DESIGN AND SYNTHESIS OF METAL-ORGANIC FRAMEWORKS FOR SUSTAINABLE ENERGY-RELATED APPLICATIONS

A Dissertation

by

XUAN WANG

Submitted to the Office of Graduate and Professional Studies of
Texas A&M University
in partial fulfillment of the requirements for the degree of

DOCTOR OF PHILOSOPHY

Chair of Committee,	Hong-Cai Zhou
Committee Members,	Kim Dunbar
	Donald Darensbourg
	Hae-Kwon Jeong
Head of Department,	Simon W. North

December 2016

Major Subject: Chemistry

ABSTRACT

Metal-organic frameworks (MOFs) are attracting because of their significant tunability, crystalline nature, permanent porosity, and tremendous surface area. These features make MOFs suitable for clean energetic applications, such as gas storage, biomedical applications, and catalysis. Till now, utilizing MOFs' stability and functionality are challenging. In general, MOFs constructed from carboxylate linkers and soft metal ions are not very stable. Moreover, functionalization of MOFs during direct synthesis often comes with many difficulties. To address those two issues, two approaches—direct synthesis of MOFs from high-valence metals and post-synthetic metal metathesis—are in this dissertation.

By using the direct synthesis approach, one of my projects seek to synthesize a series of stable Zr-MOFs, PCN-56X (PCN stands for Porous Coordination Network), constructed from Zr_6 clusters, which have been reported to exhibit remarkable chemical and thermal stability, and functionalized linear carboxylate linkers with fused rings and alkyl chains. Experimentally, some pendent groups on the linkers of these MOFs significantly utilize the packing efficiency of gas molecules and increase the total methane storage capacity. Furthermore, the PCN-56X series exhibite excellent moisture stability after exposure to laboratory conditions for six weeks.

Another project aims at building an anionic MOF to encapsulate the photocatalytic-active $[Ru(bpy)_3]^{2+}$. The resultant PCN-99 framework is constructed by a tetrahedral $[In(COO)_4]^-$ node and a specifically designed trigonal planar linker. The corresponding Ru@PCN-99 demonstrates excellent heterogeneous catalytic activities in

oxidative hydroxylation of arylboronic acids under visible light with improved reusability.

Applying the post-synthetic metathesis approach, another project startes with a template of Mg-MOF PCN-430. During the exchange with the first row transition metals, four criteria, “Liability, Open metal sites, Energy stabilization, and Geometrical preference match (LOEG),” for complete metal metathesis are discovered. This discovery can be extremely useful in the functionalization of MOFs, which brings up more potential applications of MOFs. Following the FLEG guidance, the last project shows PCN-527-Cd with more Lewis acidic iron ions via applying the post-synthetic metathesis and oxidation method. The parent PCN-527-Cd demonstrates poor catalytic activity in one-pot deacetalization-Knoevenagel condensation reactions. However, the product PCN-527-Fe has a 100% catalytic activity.

DEDICATION

To my beloved family and relatives for their continual support

To all my friends who helped me during my study in the U.S.

ACKNOWLEDGEMENTS

I would like to take this opportunity to express thanks to my committee chair Dr. Hong-Cai Zhou, and my committee members, Dr. Kim Dunbar, Dr. Donald Darensbourg, and Dr. Hae-Kwon Jeong for their support throughout the past five years.

Additionally, a special thanks to Dr. Jingbo Liu, Dr. Sajid Bashir, Dr. Abraham Clearfield, Dr. Wendy L. Keeney-Kennicutt, Dr. Vickie M. Williamson, Dr. Holly Gaede, Dr. Joanna Pellois, and Dr. Rasheedah Richardson who were my mentors and instructors at Texas A&M University. Thank you for offering me your support in chemistry education. I am forever grateful for your efforts.

I would like acknowledge the Zhou group members from the past and present. Special appreciation to Dr. Tian-Fu Liu, Dr. Weigang Lu, Ms. Ying-Pin Chen, Dr. Qiang Zhang, Dr. Zhangwen Wei, Mr. Stephen Fordham, Mr. Shuai Yuan, Dr. Junsheng Qin, Dr. Muwei Zhang, Dr. Dahuan Liu, Carrie Frederiksen, Mr. Zac Perry, and Mrs. Lizzie West for their valuable mentorship and/or professional suggestions. My thanks are also extended to every collaborator—Dr. Zhi-Yuan Gu, Dr. Jinhee Park, Dr. Kelvin Gagnon, Mr. Xi-Zhen Lian, Dr. Andrey Yakovenko, Dr. Gregory J. Halder, and Mr. Mat Bosh.

I also want to thank Ping Wang who brought me to the U.S., as well as Dr. Bill Luttrell, Dr. Amanda Nichols, and my fellows from my undergraduate institution. I would not be able to have this wonderful opportunity for the Ph.D. education without their help.

I have been fortunate to have many other friends, who have spent a majority of their time at Texas A&M University, like Dr. Baoyu Zhao and Dr. Fenglei Du. They have offered a large range of knowledge, support, and companionship.

My extended gratitude to all my friends, colleagues, and department faculty members and staffs, for making my time at Texas A&M University meaningful and wonderful.

Finally, my parents Mr. Shimin Wang and Mrs. Xiuli Du deserves my greatest appreciation for their encouragement, support and endless love.

NOMENCLATURE

BET	Brunauer-Emmett-Teller
CCDC	Cambridge Crystallographic Data Center
CCS	Carbon Capture and Sequestration
COF	Covalent Organic Framework
CO_2	Carbon Dioxide
CH_4	Methane
DFT	Density Functional Theory
IUPAC	International Union of Pure and Applied Chemistry
MOFs	Metal-organic Frameworks
NMR	Nuclear Magnetic Resonance
PCN	Porous Coordination Network
PSM	Post-synthetic Modification
PSMO	Post-synthetic Metathesis and Oxidation
PPN	Porous Coordination Polymer
PXRD	Powder X-Ray Diffraction
Q_{st}	Isosteric Heat of Adsorption
SBUs	Secondary Building Units
UMCs	Uncoordinated Metal Centers
TGA	Thermogravimetric analysis
XRD	X-ray Diffraction

TABLE OF CONTENTS

Page

LIST OF FIGURES

Page

LIST OF TABLES

Page

CHAPTER I

INTRODUCTION TO METAL-ORGANIC FRAMEWORKS: DEFINITION, SYNTHESIS, AND APPLICATION*

1.1 Metal-Organic Frameworks (MOFs): Definition, Synthesis, and Applications

1.1.1 Introduction of Metal-Organic Frameworks

Porous materials have attracted a significant amount of attention during the past few decades in scientific and technological research. Porous materials have a significant surface area, which makes them capable of adsorbing and interacting with small molecules and ions on their inner surface. Classic inorganic porous materials contain activated carbon, silica gels, activated alumina, molecular sieve, zeolites, and mesoporous silica.

Traditional porous materials have limitations of either pore size or surface area. Silica gels, activated carbon, and activated alumina are all amorphous (irregular arrangement of pores) polymers containing micro- and mesopores (micropores are defined as pores smaller than 2 nm and mesopores between 2 and 50 nm) with a wide pore size distribution. From the perspective of materials, the wide pore size distribution, the micropores, and limited surface area hamper the utilization of these pores. Therefore, extensive studies have focused on the development of new classes of porous materials,

---

* Part of this chapter is reprinted with permission from Chapter "Lanthanide Metal-Organic Frameworks: Synthesis, Properties, and Potential Application" In *Lanthanide Metal-Organic Framework*, by Fordham, S., Wang, X., Bosh, M., Zhou, H.-C., 2015, Springer Berlin Heidelberg, Berlin, Heidelberg. Copyright [2015] by Springer.

* Part of this chapter is reprinted with permission from Chapter "Metal-Organic Frameworks for Methane Storage" In *Nanomaterials for Sustainable Energy*, by Wang, X., Fordham, S., Zhou, H.-C., 2015, American Chemical Society, U.S.A. Copyright [2015] by American Chemical Society.

such as covalent organic frameworks (COFs) and metal-organic frameworks (MOFs). Both COFs and MOFs have emerged as an advanced class of porous materials. MOFs, also known as porous coordination polymers (PCPs), are defined as 1, 2, or 3 dimensional coordination networks with potential porosity.[1-3] Different from COFs, which are constructed from the linkage between light elements (H, B, C, N and O) by strong covalent bonds,[4] MOFs are connected by coordination bonds through self-assembly between inorganic metal-containing units (generally known as secondary building units SBUs) and organic linkers to form a rigid uniform crystalline hybrid materials.[2,5-7]

1.1.2 Synthetic Routes of MOFs

In general, MOFs are prepared via solvothermal or hydrothermal reactions, in which metal salts and organic linkers are heated in the presence of polar solvents with high boiling points (dialkyl formamides, dimethyl sulfoxide, or water) in a sealed vessel. In order to prepare highly crystalline materials in a dilute liquid phase condition, a reaction time of hours to days is needed for the crystallization process.[8] The synthesis of MOFs can be quite delicate due to a variety of factors greatly impacting the formation of crystalline material that can be easily characterized through traditional techniques. In general, the main factors that contribute to MOF formation include temperature, pressure, reactant solubility, pH, and concentrations of metal salts and ligands. These Lewis acid-base reactions often lead to the formation of amorphous precipitates from the rapid deprotonation of the ligand.[9] Several reaction conditions can be modified to

improve crystallinity, including lowering the reaction temperature or adding acid, such as hydrofluoroboric acid (HBF_4), which slows down ligand deprotonation rate. This often difficult trial-and-error process has led to the growth of combinatorial synthetic methods including high-throughput robotic screening.[10]

MOF-5,[11] one of the most important MOFs, was first reported by Yaghi *et al.* through diffusion of triethylamine into a solution of zinc (II) nitrate and H_2bdc(1,4-benenedicarboxylic acid) in N, N'-dimethylformamide (DMF) and chlorobenzene. However, the yield of MOF-5 through diffusion synthesis is low. Therefore, the method was further optimized to a high-yield solvothermal reaction of $Zn(NO_3)_2 .4H_2O$ and H_2bdc in N, N'-diethylformamide (DEF) at 120 ^{O}C for 24 hours.[12] The pore size of MOF-5 was further investigated to be controlled and functionalized by applying isoreticular chemistry in similar solvothermal conditions. After weak hydrothermal stability was revealed for MOF-5, attention shifted to other porous materials, such as HKUST-1[13], MIL-101[14], and UiO-66[15]. In the effort to shorten the synthesis time and produce high-quality crystals, alternative synthesis methods have been developed, such as microwave-assisted, sonochemical, electrochemical, and mechanochemical methods (Figure I-1).[8]

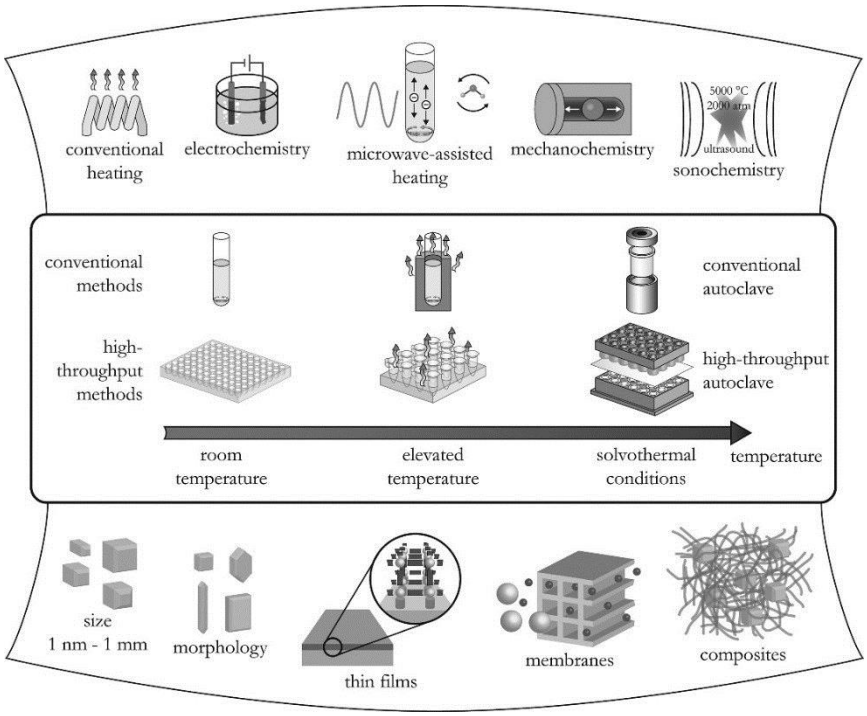

Figure I- 1. Different Synthesis Methods of MOFs. (Reprinted with permission from Ref. [*8*], copyright © 2013 American Chemical Society)

In microwave-assisted synthesis, the mixture of substrates (metals salts and organic ligands) and suitable solvent sealed in a Teflon vessel is placed in an applied oscillating electric field, which results in molecular rotation after coupling with the permanent dipole moment of substrates and consequently leads to the rapid heating of the system.[16,17] In terms of reaction time of Cr-MIL-100, the microwave-assisted reaction was significantly shortened from 4 days to 4 hours in a conventional hydrothermal synthesis.[8]

For the sonochemical synthesis, an adjustable powder output is introduced to sonicate the substrate mixture, providing a very high local temperature and pressure resulting in the formation of relatively small but high-quality crystallites.[18] In the case of

MOF-5, the crystals were obtained within 30 minutes compared to 24 hours in a solvothermal reaction.[19]

In the electrochemical synthesis, the continuous anodic dissolution drives the metal ions to react with the dissolved polyprotic acids, forming highly-crystalline powder MOF compared to the larger crystals in a batch reaction.[18,20] The electrochemical method has demonstrated high efficiency with lower temperature requirements than conventional synthesis, high yield, and no need for metal salts.[21] In the mechanochemical synthesis, mechanical force is introduced not only to break the intramolecular bonds but also to facilitate the chemical transformation, which usually occurs under solvent-free conditions at room temperature.[18]

1.1.3 Key Structure of MOFs

For the aforementioned MOFs synthesis, a multitude of new MOFs have been developed and extended from several key structures that may be important for the future development and application of MOFs. The hallmark of those MOFs is their permanent porosity. The MOFs are constructed from the metal units or SBUs[22], formed *in situ* from pre-formed organic linkers through coordination bonds. The adjustment of the geometry, length, ratio, and functional group of the linkers will consequently tune the size and shape of the pores. Based on the number and geometry of carboxylates and elements in the linker, the pre-formed organic linkers could be categorized as ditopic, tritopic, tetratopic, hexatopic, octatopic, mixed, desymetrized, metallo, and N-heterocyclic linkers. [23] In this chapter, the key discussion will focus mainly on metal units or SBUs

with ditopic or tritopic linkers. For MOFs composed of other linkers including phosphonate and sulfonate, detailed reviews have been published. [23-25]

In 1999, MOF-5 [11] and HKUST-1[13] were synthesized and characterized to demonstrate their high crystallinity and porosity, two major breakthroughs of MOF chemistry. MOF-5 was constructed from a 6-connected octahedral $Zn_4O(CO_2)_6$ cluster and ditopic acid terephthalate (bdc) giving an extended 3D cubic framework with square openings of 8 Å and 12 Å. One of the unique benefits of MOFs is that the pore size and the internal pore surface functionalities can be tuned by using pre-designed organic linkers of the same symmetry, which, according to the theory of isoreticular chemistry, will not alter the underlying topology.[26,27] MOF structures are predicable on the premise of forming SBUs with fixed linking geometries. Using MOF-5 as the prototype material, the 3D porous systems can be functionalized with the organic groups of bromo, amino, n-propyl, n-pentoxy, cyclobutyl, and fused benzene rings.[26] Their pore size can be further expanded with a stepwise expansion to biphenyl, tetrahydropyrene, pyrene, and terphenyl. This IRMOF-n series has open pores that ranging from 2.8 to 28.8 Å (Figure I-2).

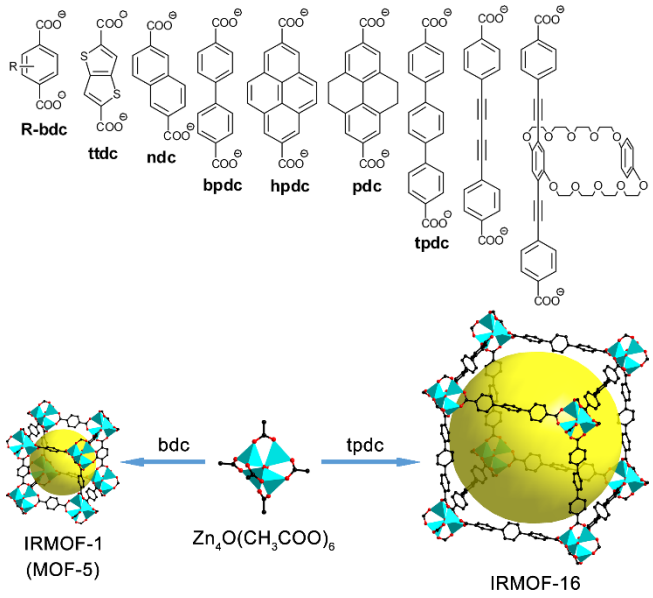

Figure I- 2. Examples of IRMOF-n series. Color Scheme :Zn (turquoise polyhedral); O (red); C (black). (Reprinted with permission from Ref. [28], copyright © 2014 The Royal Society of Chemistry)

HKUST-1,[13] another archetypical MOF, consists of 4-connected square planar dicopper paddle-wheel units as nodes and tritopic 1, 3, 5-benznetricarboxylates (btc) as linkers. Each BTC linker connects to three copper paddle-wheel SBUs forming a T_d – octahedron and occupies the alternating triangular faces of the octahedron. Along with the connection of other units, a cubic framework with **tbo** topology is formed. However, linking a 4-connected paddle-wheel unit with a ditopic acid, such as bdc, results in a two dimensional (2D) sheet rather than a three dimensional (3D) MOF material. The various combinations of different carboxylates and metal units would lead to a rich library of MOFs. The marriage of dicopper paddle-wheel units and extended tritopic organic

linkers has been shown to extend the networks of HKUST-1 and produce a variety of materials with the same network topology.

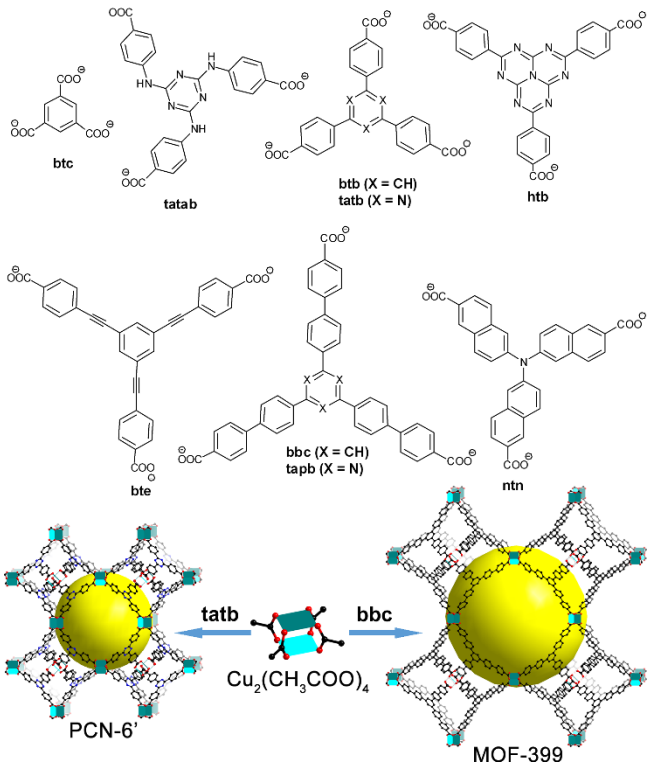

Figure I- 3. Examples of MOFs constructed from tritopic carboxylate linkers and dicopper paddle-wheel SBUs. Color Scheme: Cu (turquoise); O (red); C (black). (Reprinted with permission from Ref. [*28*], copyright © 2014 The Royal Society of Chemistry)

A combination of elongated tritopic linkers, such as 4,4',4"-s-triazine-1,3,5-triyltri-p-aminobenzoate (tatab), 4,4',4"-(1,3,4,6,7,9,9)-heptaazaphenalene-2,5,8-triyl)tribenzoate (htb), 4,4',4"-s-triazine-2,4,6-triyltribenzoate (tatb), 4,4',4"-(benzene-1,3,5-triyl-tris(benzene-4,1-diyl))tribenzoate (bbc), and paddle-wheel units yield a

number of isoreticular MOFs (meso-MOF-1, PCN-htb, PCN-6', and MOF-399, respectively) (PCN stands for Porous Coordination Network) (Figure I-3).

MOF-74[29,30], another well-known example, is the product of the coordination between tetraanionic 2,5-dioxido-1,4-benzene-dicarboxylate (dobdc) and an infinite metal chain, in which both the aryloxide and carboxylate moieties are bonded to the metal units. After applying the isoreticular chemistry of dobdc by the stepwise expansion of long molecular struts with phenylene units, a series of MOF-74 isoreticular materials was synthesized with pore apertures incrementally varied from 14 Å to 98 Å (Figure I-4). [31]

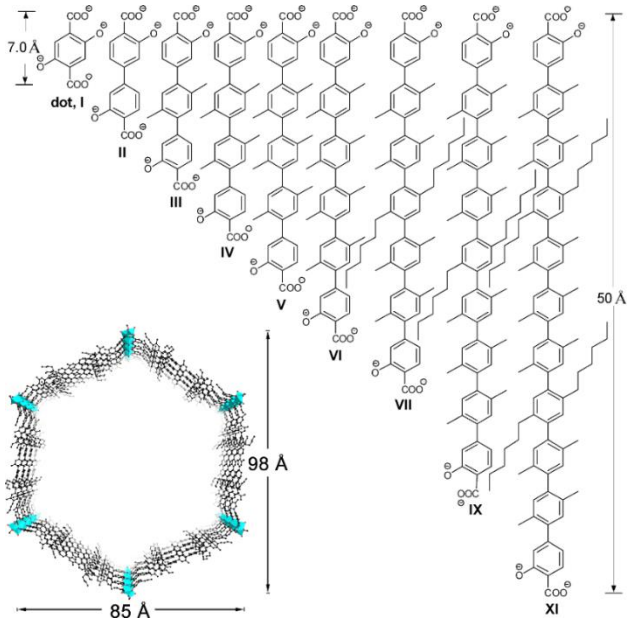

Figure I- 4. List of organic linkers used in IRMOF-74 series with the one-dimentional channel with 98 Å for IRMOF-74-XI. (Reprinted with permission from Ref. [*28*], copyright © 2014 The Royal Society of Chemistry)

To date, IRMOF-74-XI with a pore aperture of 98 Å is the record holder for the largest pore among all crystalline materials. These large pores are capable of allowing natural proteins to enter without folding, which demonstrates great potential for MOFs to serve as a matrix for enzyme immobilization.

Besides 6-connected octahedral metal units, another important SBUs is 6-connected trigonal prismatic metal units. MIL-101[14] (MIL stands for Materials Institute Lavoisier) is a signature MOF, made from the linking of bdc and metal trimmers, where three trivalent metals each coordinate with four oxygen atoms of bdc, one μ_3-O, and one oxygen from terminal water or fluorine groups in an octahedral environment.

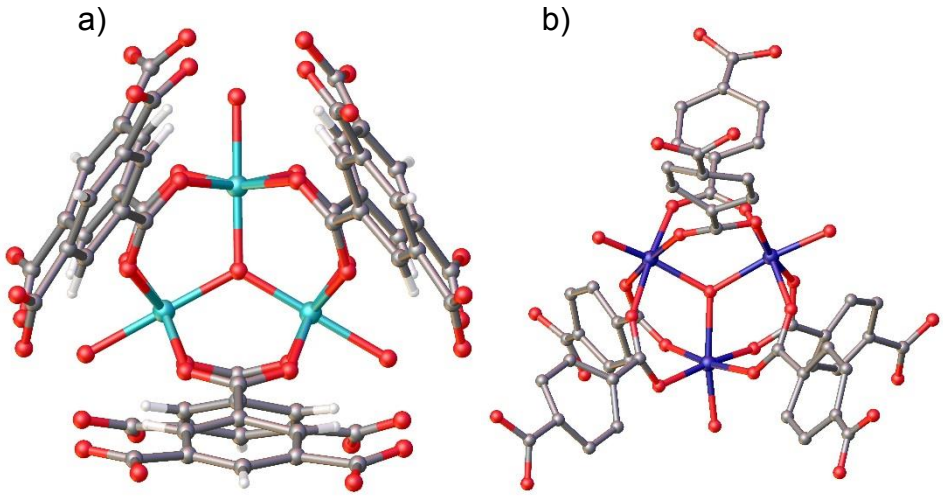

Figure I- 5. a) MIL-100, Cu SBU with coordinated btc linker; b) MIL-101, Cu SBU with coordinated bdc linker. Color Scheme: Al (blue, purple); O (red); C (gray). (Reprinted with permission from Ref. [32], copyright © 2014 The Royal Society of Chemistry)

MIL-101 (Figure I-5) is a mesoporous MOF with a hexagonal window of 16 Å and a cage diameter of 34 Å. At the same time, MIL-101 is also acknowledged for enhanced hydrothermal stability through increasing the charge of the metals. Assembling the same trimeric SBUs with the tritopic linker btc, MIL-100[33] was successfully synthesized. A so-called "supertetrahedra" is formed with four trimeric metal units as vertices and four btc as the triangular faces. The further connection between these supertetrahedras gives rise to two mesoporous cages with accessible diameters of 25 and 29 Å.

In addition to the aforementioned 4- and 6-conneted SBUs, a 12-connected SBU, $Zr_6O_4(OH)_4$, is identified as a new class of building units to be investigated and explored. In 2008, the first Zr-MOF, UiO-66 (UiO stands for University of Oslo) was synthesized under a solvothermal condition using bdc as the organic struts.[15] In the framework of UiO-66, six Zr atoms in the square-antiprismatic coordination environment are linked by eight oxygen atoms from four bdc linkers and four alternatives of μ_3-O and μ_3-OH on the triangle face to form the $Zr_6O_4(OH)_4$ core. In the UIO-66 structure, each $Zr_6O_4(OH)_4$ core is further connected by twelve bdc**,** consequently resulting in a 3D framework with a triangular window of 6 Å in diameter. The $Zr_6O_4(OH)_4$ building units have been further applied to achieve desired stable porous materials. Functional groups on bdc[34]and elongated benzene rings[15,35] have been designed for gas storage and metal sensing. However, MOFs with 12-connected SBUs are still scarce.

As the study of MOFs is still a burgeoning field, new SBUs are expected to be identified in the future. With the knowledge of reticular chemistry, substantial development of MOFs with new structures is expected.

1.2 Ionic Metal-Organic Frameworks

In general, the positive charges of metal ions in MOFs are balanced off by the negative charge of the metal linkers (arylcarboxylates in most cases). However, a special family of ionic MOFs was discovered, where the framework could be positively or negatively charged with counterions either free or weakly coordinated to the metal SBUs. [36-38] Moreover, those counterions could be easily exchanged with other exogenous ions improving host-guest interactions for specific applications. [39,40]

Based on the charge of counterions in the framework, ionic MOFs are classified into anionic and cationic frameworks. The anionic MOFs have a negatively charged framework with extra cations attaching the pores, while the frameworks of cationic frameworks are positively-charged with subsequently negatively-charged counterions in the frameworks. The overall charge of any ionic MOF with its counterions must be zero. Like the synthesis of normal MOFs, *in situ* synthesis and post-synthetic approaches are two common routes to produce ionic MOFs.

1.2.1 Anionic Metal-Organic Frameworks

The formation of anionic MOFs through the *in situ* synthesis is often results of the hydrolysis of solvents, like DMF and DEF, and sequential decarboxylation in present

of water, which produces $NH_2Me_2^+$ or $NH_2Et_2^+$ serving as the counterions to balance the overall charge of frameworks (Figure I-6) . [41] On other hand, solvents like DMA could also be used as templates to synthesize anionic frameworks. [42-44]

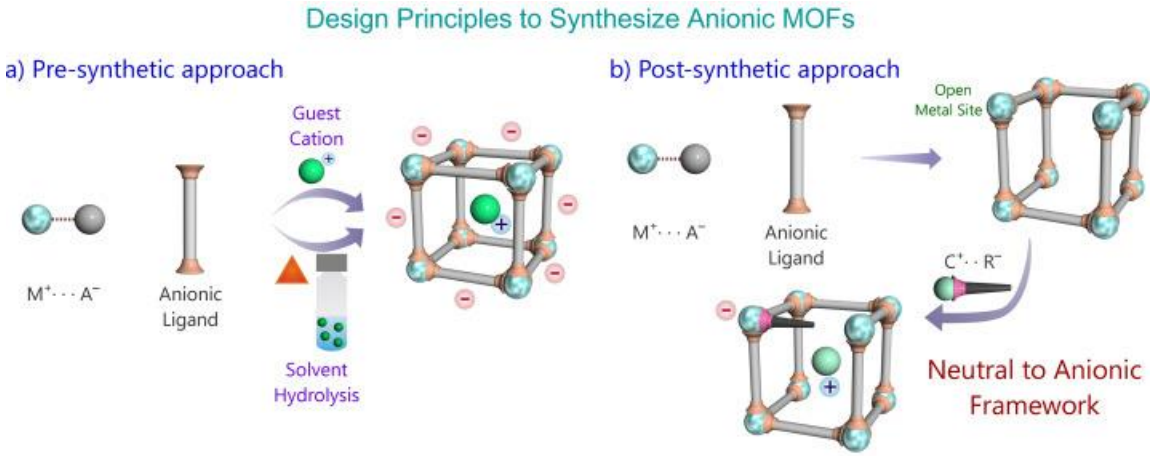

Figure I- 6. Design strategies for the synthesis of anionic MOFs. (Reprinted with permission from Ref. [*41*], copyright © 2014 The Royal Society of Chemistry)

Another advancement to synthesize ionic MOFs is the development of various SBUs, which have been reported previously with the formation of anionic MOFs. One of the most classic series is the zeolite-like MOFs (ZMOFs), which are based on the SBU of $[In(CO_2)_2N_4]^-$.[45-47] The monoindium $[In(CO_2)_4]^-$ cluster is another SBU that is frequently found in anionic MOFs. [48-59] Moreover, reports have been shown that the tetranuclear butterfly-like $[M_4(OH)_2]$ SBU could result in anionic MOFs.

So far, there is only one case been reported in the literature where a neutral MOF was transformed into an anionic MOF. [60] The original neutral $Zr_6O_4(OH)_4$ SBUs in UiO-66 are dehydrated Under vacuum with heating to 300^{O}C. Then grafting LiOtBu onto the

unsaturated Zr^{4+} leads to an anionic framework with the Li+ ion trapped in the cavities. Overall, the post-synthetic approach to achieve MOFs is a daunting task, since it requires the robustness of parent framework with sufficient large pores allowing the exchange of the counterions.

One of the applications for the anionic MOFs is for gas storage. As the key interaction between MOFs and gas molecules is Van der Waals interactions, a polarized MOFs will more likely have stronger interactions with CO_2 and H_2 molecules. With this regard, researchers studied the counterions effects on the overall CO_2 and H_2 capacities.[61-65] They found incorporation of some of the cations in the MOFs via post-synthetic modification would not dramatically increase the overall capacity with an improvement of heat of adsorption, but also the overall selectivity.

In the presence of the free counterions, the catalytic capabilities of ionic MOFs could be easily altered by simply post-synthetic exchange with some catalytic-active species. Catalysts, for example metalloporphyrins,[66] transition metal components,[67] as well as other nanoparticles[68], have been previously encapsulated in anionic MOFs through cation exchanges. Those heterogeneous catalysts were able to catalyze hydrocarbon oxidation, hydrogenation of alkenes, and epoxidation of styrene, respectively, with good catalytic activity and reusability.

Non-linear optics (NLO) describes that the dielectric polarization responds nonlinearly to the electric field of light. One of the first pre-requites to fabricate new NLO materials is the non-centrosymmetric properties of the materials.[69-71] In this case, ionic MOFs outperforms other materials by the high polarity of the framework, and

tunability of the acentric properties. Moreover, the extra framework could be easily replaced by a high loading of chromophore. Studies on the cation exchange of anionic MOFs with small mental ions[72] or cationic chromophores [51] will significantly enhance the secondary harmonic generation performance.

Another interesting application is related to drug delivery. [73] After the post-synthetic cation exchange in a bio-degradable MOF with procainamide HCl, a common drug to treat cardiac arrhythmias, the researcher were able to capture a large amount of this drug via the cation exchange with in an anionic MOFs. Besides, the release of the drug could be easily triggered by buffer solution to completion.

The exceptional ionic nature and surface area make the anionic MOFs an exclusive class of material for chemical sensing of small molecules.[74,75] The specific electronic selectivity could recognize any cation without altering the crystallinity of the MOF hosts. However, other properties, such as luminance, fluenrence, bonding environments, and oxidation states of metal in the SBUs/organic likers, could be the criteria used to evaluate the performance of sensing. The applications stem from the chemical sensing of the lanthanide cations[76,77]and other heavy metal ions[78] to the detection of explosive[79] to regular pH sensing[80,81].

Last but not least, the "free" cation counterions in the anionic MOFs could potentially act as proton source, where the proton could be further carried by the water molecules to promote great conductivities even at low humidity. [82,83]

1.2.2 Cationic Metal-Organic Frameworks

Different from the anionic MOFs, cationic MOFs have the framework positively-charged with extra anions lying free in the cavities or weekly coordinating to the metal SBUs. General synthetic strategies of cationic MOFs are listed in Figure I-7.

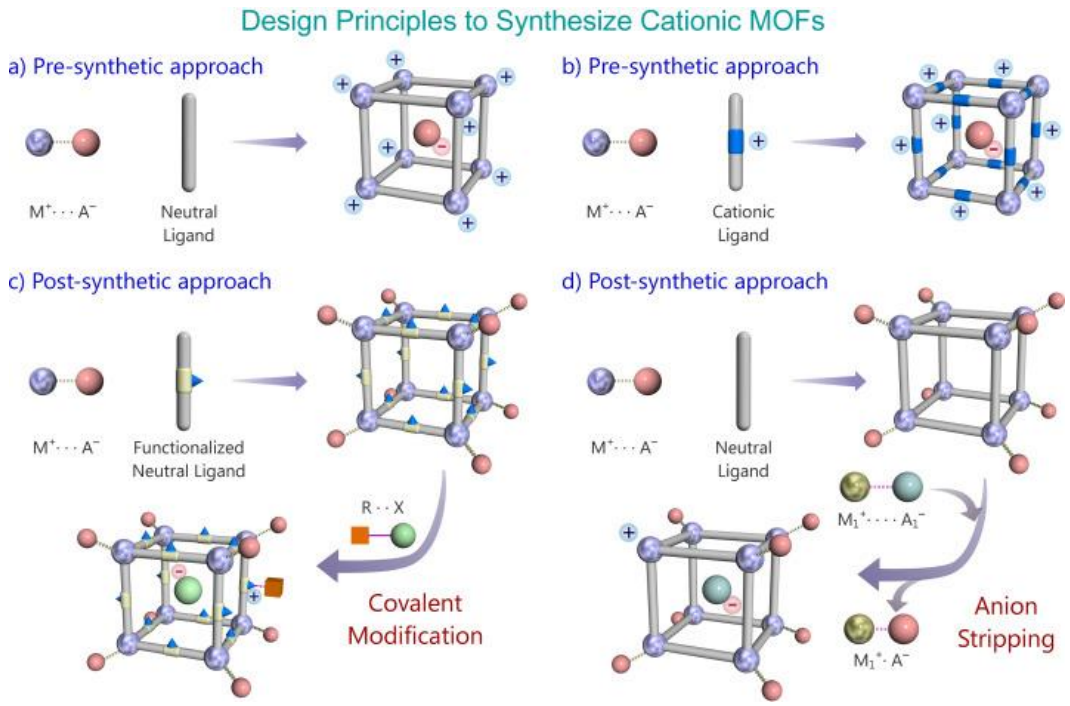

Figure I- 7. Schematic representation of cationic MOFs. (Reprinted with permission from Ref. [*41*], copyright © 2014 The Royal Society of Chemistry)

One set of ligands commonly found in the cationic MOFs is the neutral nitrogen donor ligands, which require extra anions in the framework to balance off the charge of metal-containing SBUs.[41] Many of the reported cationic MOFs are constructed from 4, 4'-bipyridine. [84-91] Other nitrogen donor-based cationic MOFs include pyridyl-based

MOFs,[92] imidazole-based MOFs,[93] and pyridylamide-based MOFs. [94,95] Despite a neutral nitrogen donor ligands building up cationic MOFs, the use of cationic ligands could also give rise to cationic MOFs. Examples of using imidazolium-containing ligands to construct the cationic MOFs have been previously reported. [96,97]

Construction of cationic MOFs from neutral frameworks via post-synthetic approach is also rare. On one hand, the pyridyl nitrogen on the linker could be modified to form a cationic MOF. [98]After immersing POST-1 in excess iodomethane, the pyridyl nitrogen atom was alkylated producing a cationic framework with iodide as the counterions. On the other hand, utilizing the difference in the affinity between metal ions and anionic species made it possible to exchange the free anions producing a cationic MOFs. [99]

Similar to the anionic MOFs, cationic MOFs also demonstrate great polarizability, which could be widely used in sensors. Here the cationic MOFs could further polarize non-polarized molecules. Specific studies revealed that the luminescence profiles will be dramatically changed upon the explosion to different organic solvents. [41,100] In spite of luminescence properties, cationic MOFs could also be employed as colorimetric sensors when incorporated with different anions. [101-104]

Similar to sensing, cationic MOFs have some similar applications to those of anionic MOFs. First, magnetic properties could be changed completely upon the incorporation of guest molecules[105] or simple desolvation[106]. Then, clear structural transformation could be observed in a single-crystal-to-single-crystal transformation[107-110], which could result in different topologies[111]. Also, another structural property that

will be altered is the porosity of those MOFs. To respond to the tuning the porosity, the corresponding gas capacity as well as selectivity will be significantly influenced at the same time,[112-114] even for other carbon-based molecules. [115,116] In addition, cationic MOFs have demonstrated great potential in the application of drug delivery[115], proton conduction[117], dye encapsulation[118,119], and heterogeneous catalysts[120-122].

1.2.3 Ion-Exchange Performance in Ionic MOFs

The use of natural ion exchangers has drawbacks, such as their non-adjustable pore sizes, poor stability, low exchange capacities and selectivity, and lack of recyclability. [41] However, ionic MOFs are superior to natural ion exchangers due to the former's inherent controllable and uniform porosity, good thermal stability, tremendous surface area, and excellent tunability. The strong coulombic forces, highly polarizable nature of metal-containing SBUs, and week coordinated counterions with great accessibility make ionic MOFs an excellent candidate to serve as ion exchange resins.

Until now, the applications of the anion exchange of cationic MOFs focus on the removing of the heavy oxo-anions, [123-126] like ReO_4^-, CrO_4^-, TcO_4^-, $Cr_2O_7^-$, MnO_4^-, AsO_4^{3-}, SeO_3^{2-}, etc from the list of oxo-anions in water waste, which are the top pollutants found in nature and potential threats to human life and the environments[41]. The porous nature of MOFs allows for these problematic heavy metal ions to diffuse easily through the frameworks facilitating the process to capture the heavy metal ions. Furthermore, the high surface area endorse those cationic MOFs with significant ion

capacity. On the other hand, studies on the cation exchange of anionic MOFs are extremely lacking due to the lack of anionic MOFs with large pore apertures.

1.2.4 Summary

The ionic MOFs exist as a special class of MOFs due to their charge of framework and loosely-bounded counterions. The inherent ionic nature makes those MOFs more polarizable than any neutral MOFs. This unique advantage of ionic MOFs provides stronger coulombic forces between MOFs and guests, which has great potential in applications of sensing and gas storage. The loosely-bounded counterions allow the possible incorporation of other useful species, such as catalytic active ions and small drugs, to fabricate the functionality of the MOF system with the expense of porosity. After judicious rational design of those MOFs, the ionic MOFs could hold many advantages over the majority of neutral MOFs, especially as ion-exchange resins.

1.3 Post-synthetic Metathesis of Metal-Organic Frameworks

1.3.1 General Information about Post-synthetic Metathesis

Post-synthetic metathesis, or cation exchange, offers a novel approach to synthesizing new materials when direct synthesis fails. The conventional synthesis at high temperature or pressure could result in one or mixed structures that are usually thermodynamically favored. Since metal ions possess various coordination modes, the desired framework topology or functionality through the direct synthesis might not be achieved as the final product. Thus, post-synthetic metathesis provides such aids, in

which the parent framework topology and functionality could be retained in the exchange process. As the post-synthetic metathesis occurs at the metal-containing nodes, or SBUs, the abundance of different metal-containing SBUs provides great possibilities to extend the list of parent template to be replaced.

1.3.2 Classical MOF Examples of Post-synthetic Metathesis

A good example of metal exchange controlled by the accessible pore size of parent MOFs was also observed in MOF $[Co^{II}_4O(bdpb)_3]_n$ (MFU-1; H_2bdpb=1,4-Bis[(3,5-dimethyl)pyrazol-4-yl)benzol])[127]. At tempts to replace Co^{2+} substitution in MFU-1 to other redox active elements were not successfully.[128] Furthermore, the attempt with a MOF of similar structure $[Zn_5Cl_4(BBTA)_3]\cdot_3$ DMF (Zn-MFU-4; H_2BBTA= 1H,5H-benzo(1,2-d:4,5-d')bistriazole)) also failed due to the diffusion limitation from the small pore size. However, partial substitution of Zn (~80%) was observed in the elongated Zn-MFU-4l using H_2BTDD (bis(1H-1,2,3-triazolo-[4,5-b], [4',5'-*i*])dibenzo-[1,4]-dioxin). Based on this comparison, it is implied that ligand elongation by only one phenyl ring from MFU-4 to MFU-4l allows the metal ions to diffuse inside of the MOFs so that substitution could happen.

Another example to elucidate the importance of pore size control is the transmetalation between Zn and Cu in HKUST-1 and PMOF-2, which are constructed from zinc paddlewheel SBUs with 1,3,5-benzenetricarboxylate and 1,3,5-tris(3,5-dicarboxylphenylethynyl)benzene, respectively. [129] Zn-HKUST-1 demonstrated only partially exchanged metal (~53%) even after being soaked in 0.5 M Cu^{2+} solutions for 3

months, whereas Zn-PMOF-2 experienced complete exchange only after in dilute copper solution for 3 days. It seems like the longer length of the linker in Zn-PMOF-2 not only allow the metal ion to diffuse more easily but also enhance the framework flexibility, which finally maximize the degree of metal exchange. With this regard, we believe that the presence of larger pores in the MOFs is a prerequisite for the complete metal exchange.

One example of the very first complete metal exchange was reported by Kim and coworkers. [130] Exchange with the model MOF $Cd_{1.5}(H_3O)_3[(Cd_4O)_3(HETT)_8]\cdot 6H_2O$ (HETT= 5,5',10,10', 15,15'-hexaethyltruxene-2,7,12-tricarboxylate) with Pd^{2+} was completed in 2 days in a single-crystal to single crystal transformation. However, the reverse transformation from Pd^{2+} to Cd^{2+} took 3 weeks to complete. It can be explained that the stronger Pd-O bond coordination significantly slow down the exchange process and likely result in incomplete metal exchange in relatively short period of time.

Cohen and coworkers studied the metal exchange of the robust structure Al-MIL-53-Br, which is a well-known stable MOFs. [131] Even under this heating environment, only about 40% of the crystalline particles containing Fe ions were observed by Aerosol time-of-flight mass spectrometry (AOFMS). Moreover, similar partial exchange was observed in the case of Zr-UiO-66.[131,132] Only 37.9% of Ti^{4+}[133] , a small portion of Hf^{4+}[133] , and 5% Ce^{4+} [132]were incorporated into Zr-UiO-66, respectively. The moderate incorporated amounts of entering metal could be attributed to the inertness of the Zr-O bonds. Recently, we reported a synthetic strategy, called high valence metathesis and oxidation, to synthesize the Ti-MOFs. [134]Using Sc-PCN-333 and Sc-MIL-100 as the

templates, partial exchanges were observed for all cases with exchange rates of 88.0%, and 48.8%, respectively.

All the examples indicated that the inertness of Al-O, Zr-O, and Sc-O bonds require more energy input to be broken and exchanged, which definitely prevented the acquisition of complete replacement. Moreover, the lability of parent MOFs could be further manipulated by the redox nature of the metal. Taking advantages of the redox reaction between Fe(III) and Cr(II), our group was able to exchange ~93% of Fe(III)-PCN-333 with Cr(II) with preserved crystallinity and porosity. [135]

In this case, the ideal template MOFs for complete metal exchange should be constructed from relative labile metal-linker bonds. With this regard, the central metal nodes of the template MOFs are ideal with a low water- and low thermal-stability compare to the exchanging metal. However, extra care on the liability of leaving metal species must be considered in order to maintain the crystallinity and porosity, since there must be a balance between the dissociation rates of leaving metal and that of incoming metal species. A good example is the insertion of Cr(III) into the PCN-333 system. [136] The frameworks of Sc-PCN-333 completely collapsed during the metathesis, while the Fe-PCN-333 retained the crystallinity and porosity.

In the case of first row transition metals, Song and coworkers has reported the progress of substitution in the crystals of MOFs, $[M_6(BTB)_4(BIPY)_3]_n$ (M-ITHD; M= Zn^{2+}, Cu^{2+}, Co^{2+}, and Ni^{2+}). [137] Both of the Co-ITHD and Zn-ITHD collapsed under vacuum activation, while the Cu-ITHD and Ni-ITHD maintained the full porosity. In addition, the Co-ITHD and Zn-ITHD were reversibly exchanged, but Zn^{2+} could not

replace the Cu^{2+} or Ni^{2+}. It was obvious that the stability trend of those paddlewheel systems ranked MOFs from most to least stable, Cu>Ni>Co>Zn, which agrees with the Irving-Williams Order of Stability. [138]

In spite of the complete palladium exchange in the MOF $Cd_{1.5}(H_3O)_3[(Cd_4O)_3(HETT)_8]\cdot 6H_2O$, this MOF also demonstrates complete substitution by Nd^{3+} and Dy^{3+} in a longer time of 12 days. [130] As all the lanthanides ions are considered as relatively hard Lewis acid , Cd^{2+} as soft Lewis acid, and carboxylates as hard Lewis base, the Ln^{3+} ions will be much easier to be exchanged in the metal nodes with the higher positive charge compare to Cd^{2+} ions. Also, complexes with the higher positive charge should favor approach of the nucleophile, the linker in this case. Therefore, this thermodynamical preference of Nd^{3+} and Dy^{3+} over Cd^{2+} dictates the final Ln- MOFs.

Another significant example to demonstrate the importance of the nature of incoming metal is the complete exchange of Fe and Cr using Mg-MOFs as the parent MOFs.[139] Single crystals of Fe-PCN-426 and Cr-PCN-426 were successfully obtained via the Fe(II) and Cr(II)-MOF interemediate using the template of Mg-PCN-426 , in which the Mg-O bonds were more labile than common coordination bonds. The lability of Mg-O bonds has also been demonstrated in the case of a bimetallic MOFs $Mg_2[Mg_4[Cu_2\text{-}(Me_3\ mpba)_2]_3$ (Me_3mpba^{4-}=N, N' -2, 4, 6-trimetyl-1,3-phenylenebis(oxamate)). [140] Complete replacement of Mg to Co and Ni were observed while the copper ions retained untouched. This unique substitution can be explained by

the fact that Ni-O and Co-O bonds are much stronger than the Mg-O bonds but weaker than the Cu-O bonds.

From the mentioned cases above, we can tell that complete metathesis could occur if the metal-oxygen bonds of target MOFs is more energetic stable compare to those of the parent MOFs. This trends could also be related to the Ostwald's step rule that the thermodynamically stable step will eventually predominate in the crystallization process. [141]

It is worthy to note that the ITHD system, which is mentioned in last section, adopt a pillared paddlewheel SBUs rather than square plane geometry of regular paddlewheel structure. [137] This distinctive geometry could lead to the steric hindrance that prevent the complete replacement by entering metal ions. Therefore, the exchange between Zn-ITHD and Co-ITHD was reversible while the Cu and Ni species were not. Similar geometrically selectivity was also demonstrated in MFU-4l composed of crystallographically independent octahedral and tetrahedral Zn motif [128]. It was found only Co^{2+} replaced the tetrahedral Zn^{2+} center while the octahedral remained inert.

One of the very first metathesis in $Mn_3[(Mn_4Cl)_3(BTT)_8(CH_3OH)_{10}]_2$ (BTT=1,3,5-benenetristetraazolate, in which the linkage of the chloride –centered square-planar $[Mn_4Cl]^{7+}$ units and BTT^{3-} formed an anionic 3D framework, also implicated the geometrical preference based on the nature of entering ions.[65] The substitution of Li^+, Co^{2+}, and Fe^{2+}, turned out to exchange of the charge balancing extra-framework Mn^{2+} cations, while only Cu^{2+} and Zn^{2+} were able to afford partial intra-framework exchange materials. A more detailed study on the replacement site were

reported by Dincă and coworkers. [142] Using multi-wavelength anomalous X-ray dispersion, the researchers were able to determine the extent and location of the incoming metal by exploiting the dispersive differences between the exchange metals and parent Mn-MOF. Interestingly, they found the partial exchange to Cu and Zn showed a preference at the C_{4v} sites than Fe.

Our group has recently reported the preferential copper substitution in a Mo-MOP. [143] The coordination of bridging ligands and dimetal paddlewheel afforded a molecular square and cages, which were nested through multi-point hydrogen bonding and added up to the novel core-shell structure. Two ligand conformers coordinated to two distinct Mo_2 units, one in the core and the other one in the shell. The copper metathesis of Mo-MOP demonstrated the core selectivity while those in the shell are partially substituted. Similar central metal ion substitution was also observed in another double-helical wheel MOP. [144]

A more extensive example is reported by Yan and coworkers with the template MOF composed of interpenetrated cationic and anionic nets. [145] The Zn nodes MOF had three crystallographically geometry—square pyramidal, triangular-paddlewheel, and octahedral. In the investigation of metal exchange with Cu^{2+}, Co^{2+}, and Ni^{2+}, only partial copper exchange was observed. The authors pointed out that both of the nickel and cobalt were not capable to adopt the aforementioned unusual coordination geometries, whereas the copper was versatile enough to compromise those geometry to some extent. In addition, the post-synthetic metathesis of Cd-MMPF-5, which constructed from a porphyrinic moieties and dicadminum nodes, surely displayed the preferential position

of cadmium. [146] It was interesting to find that all the Cd ions within the porphyrin macrocycles were replaced by Co while the Cd ions serving as nodes remained intact. Therefore, another key factor to affect the extent of post-synthetic metathesis is the coordination of target MOFs. Recently, we reported the synthesis of Ti-MOFs through post-synthetic metathesis using Zn-MOF-74, and Mg-MOF-74 as the templates.[134] As the Ti-O chain have rarely reported it became reasonable to get 94.7%, and 37.9% substitution with Ti. We can conclude that a complete metal replacement could occur if the coordination of the mother MOFs should also be the geometrically favored and desired by the final MOFs.

Scanning all In the previously-mentioned example of $Cd_{1.5}(H_3O)_3[(Cd_4O)_3(HETT)_8]\cdot 6H_2O$ was the open metal site on the square planar $[Cd_4O]^{6+}$ units provides such the valency that reduce the steric hindrance and certainly facilitate the complete metal exchange. [130]

Meantime, one can see the distinct influence due to the nature of ligand in a similar square planar moiety in POST-65 $Mn[H_3O][(Mn_4Cl)_3(HMTT)_8]$. [147] Using POST-65-Mn as the template, complete exchange in the exchange of Fe^{2+}, Co^{2+}, and Ni^{2+} was confirmed by ICP-AES. From the tetrazolate to carboxylate ligand, the influence of the ligand change dramatically from relative strong field ligand to the weak field. The resultant exchange extent underline that the geometrical preference of metal units relies on the nature of the coordinate linkers in some aspect.

There are other factors, for example solvent playing a critical role in crystallization and reconstruction.[148,149] It is common that the use of different solvent

result in diverse MOF, morphology and interpenetration as well as the extent of both ion exchange and linker exchange. [149-153] To identify the influence of solvent parameters on cation exchange, Dincă and coworkers investigated the insertion of Ni^{2+} into Zn-MOF-5 and Co^{2+} into using several common solvent, such as DMF, DMSO, N-methyl-2-pyrrolidone (NMP), N-methylformamide (NMF), THF, and MeCN. [154] After plotting the exchange ratios determined by inductively coupled atomic emission spectroscopy (ICP-AES) against the ligand field parameter of the corresponding $[Ni(solvent)_x]^{2+}$, the cation-solvent interaction dominated the exchange-determining step in the MOF-5 system. It was found that weak Ni^{2+}-solvent interaction fasten the releasing of Ni^{2+} but retarded the rate of exchange. Furthermore, the comparison between the theoretical calculation and experiment results demonstrated the two-fold role of solvent during the metathesis, which affected both the stability of the intermediates and the flexibility of the lattice. [155] The coordinated solvent molecules would first promote the exchange, but it can also block the second transmetalation cycle if the metal-solvent bond was too strong and the flexibility of lattice became restricted. At the same time, the degree of incorporation of Co in Zn-MFU-4l became completely opposite. [154] In spite the fact of the central octahedral Zn in MFU-4l remained (mentioned in last section), the exchange rate of the peripheral tetracoordinated Zn sites increased for more Lewis basic solvents. Based on those two cases, we can tell that the role of solvent in metathesis is likely system-dependent.

In general, most of the experiment post-synthetic metathesis are under the excess loading of solvent. However, the amount of solvent loaded during the transmetalation

also matters. Recently, the energetics of solvent-MOF-5 interaction was measured by solution calorimetry, which suggested that the solvent-MOF interaction was more exothermic with low solvent loading compared to that of high solvent loading. [156] Therefore, the interaction between electron accepting Zn_4O cluster and electron donating solvent could be manipulated by changing the solvent loading, which is meaningful for complete transmetalation. A detailed studies on the coordination between DMF and Zn-MOF-5 was reported later. [157] The analysis of solid-state ^{65}Zn and ^{13}C NMR, mass spectrometry, first-principles molecular dynamics simulations, UV-Vis and TGA revealed that two DMF solvent molecules bound to the Zn_4O cluster, which was generally believed as rigid structure, distorted the tetracoordinated Zn ion, and increased the coordination number of Zn itself. The dynamically coordinated DMF solvent dissociated from the cluster during the metathesis with Co and allowed the presence of metastable Co-MOF-5.

Last but least that, exchange temperature will also a key factor with a significant influence on the metathesis. In the case of Fe-PCN-333, no apparent color change was observed corresponding to the low exchange ratio metathesis of 23.0% Fe/Cr at 85^{o}C. [136]Whereas the temperature increased to 150^{o}C, about 99.8% Fe ions were replace by Cr(III).

1.3.3 Summary

From these reported studies, we can draw several guidelines for metal exchange. First, metathesis between two metals with similar coordination modes will likely be

completed. Then a large pore diameter of the parent MOFs will also facilitate the cation exchange process. In addition, we observed a large concentration of incoming metal could drive the exchange equilibrium to replace the metal ion in the framework rather than be trapped within the framework. Besides, factors including ionic radii, reaction kinetics, solvent effects, and framework flexibility demonstrated significant influences in the exchange process.

The addition of open metal site via post-synthetic metathesis have demonstrated significant enhancement of gas adsorption, as well as catalytic activities. Post-synthetic metathesis provide such great possibilities to functionalize primary inert MOFs.

1.4 Methane Storage for Metal-Organic Frameworks

1.4.1 General Information about Methane Storage in Metal-Organic Frameworks

In 2012, the consumption of gasoline in United States increased to 134 billion gallons per year compared to 117 billion gallons in 1995. [158] With such a huge global demand for gasoline, gasoline prices have increased dramatically year by year. Natural gas is a gaseous mixture of predominately methane, some longer chain hydrocarbons, carbon dioxide, hydrogen sulfide, nitrogen and oxygen. The abundance of natural gas in the environment yields a low price fuel with wide availability, thus natural gas displays potential to serve as an alternative fuel compared to other fuels, such as ethanol, hydrogen, electricity, all of which require energy input from external sources to generate. Even though extensive pipeline networks of natural gas have been constructed through the U.S. only ~0.1 % of natural gas is used for transportation. [158] Much more

interest for natural gas vehicles has been due to the fact that combustion of methane boasts the smallest amount of CO_2 per unit of heat produced among fossil fuels. In addition, methane produces a larger heat of combustion compare to that of gasoline on a gravimetric unit basis (55.7 MJ/kg for methane vs 46.4 MJ/ kg of gasoline).

Currently, there are two common storage methods of natural gas—liquefied natural gas (LNG) and compressed natural gas (CNG). The LNG storage method involves the liquefaction of the natural gas below the critical temperature of methane 191K (-81^{o}C) with a risk of boil-off losses, which requires an expensive cryogenic vessels as the carrier. On the other hand, the CNG storage method refers to the compression of natural gas in a heavy, thick-walled cylinder with pressure of 200-300 bar produced by multi-stage compressors. Current technology limits LNG and CNG to a volumetric energy density of 22.2 $MJ \cdot L^{-1}$ and 9.2 $MJ \cdot L^{-1}$, respectively. The lower energy densities of LNG and CNG (32.4 $MJ \cdot L^{-1}$ for gasoline), and requirements of specialized containers indicate a relatively short driving distances with additional limitations of cargo spaces. In order to realize the benefits of natural gas vehicles, adsorbed natural gas (ANG) has become an active research topic. [159-162] ANG technology, using porous sorbents to store natural gas at a substantially higher concentration than that with simple compression. [163] Possessing sufficient volumetric storage ability yields ANG sorbents as a competitive alternative to existing NG storage methods with no requirement of refrigeration methods or expensive ancillary equipment. ANG also has merits due to efficient gas filling and release for automotive applications.

1.4.2 Fundamentals Associated with Adsorbed Natural Gas

Identifying the potential of ANG, the Advance Research Projects Agency-Energy (APRA-E) of the United States Department of Energy (DOE) issued a call including the ANG storage target to guide the future development of sorbents. The desired sorbent should have a volumetric capacity of 350 cm^3 (STP) $\cdot cm^{-3}$ (STP=standard temperature and pressure: 1 bar, 273.15 K), and a gravimetric capacity greater than 0.5 $g_{CH4}/g_{sorbent}$. Additionally, ideal sorbents are expected to demonstrate resistance to the impurities in natural gas with a cost of \$10 / $kg_{sorbents}$. [164]

As a multitude of efforts are being taken in the storage of methane, accurate measurements at high-pressure are essential to evaluate the performance of each sorbent for storage capacity. However, it is challenging to measure gas uptake at high pressure over a large pressure range, during which the gases usually demonstrate a nonlinear behavior under an increasing pressure.[165]

Measurement of the adsorption isotherm is the fundamental step. The amount of gas adsorbed at high pressure could be measured with the use of either volumetric instrument or gravimetric instrumentation. Gravimetric uptake analysis uses a microbalance to record the weight change of sample at different pressure of methane, so the gravimetric uptake is expressed as the mass of methane per unit mass of MOFs. On the other hand, the volumetric instrumentation uses the Sieverts apparatus to record the pressure change when dosing methane to a cell containing the MOF sample. Therefore, the volumetric uptake is expressed by the volume of adsorbed methane under standard temperature and pressure divided by the volume of MOF.

A gravimetric capacity is the most common standard measurements. In order to calculate the volumetric uptake, knowing density of MOFs is essential. Although differences between the practical packing density and crystallographic densities are indeed observed.[166,167] the ideal crystallographic density is widely used to convert the gravimetric capacity to the volumetric capacity. The calculated volumetric uptake maximizes the possible storage capacity, which represents the maximum capacity achievable in absence of any practical packing losses. Improvement in volumetric capacity has more impact than that of gravimetric capacity for natural gas vehicles on the vehicle driving range. [165]

The deliverable capacity, also known as working capacity, is the key standard to determine the driving range of a methane powered vehicle. The deliverable capacity is defined as the amount of methane released when the pressure is reduced. [165] It is generally calculated as the difference of volumetric capacity between the upper and low pressure limits at standard temperature and pressure. The lower limit of 5 bar is generally set based on the typical internal combustion engines powered by natural gas, while the upper limit is set at 35 or 65 bar, which could be achieved by a single-stage or two-stage compressor. Chapter I Introduction to Metal-organic frameworks: definition, synthesis, and application

The deliverable capacity can further improved by reaching higher storage pressure (65 bar and up) and lower engine intake pressure (1-2 bar).It is apparent that maximized capacity at upper pressure limits and minimized capacity at lower pressure limits will produce the best deliverable capacity. In this case, the maximum deliverable

methane capacity between 5 bar to 35 or 65 bar will enable natural gas vehicles with on-board storage and at-home refueling in light-duty tanks with current compressor technology.

1.4.3 Benchmark MOFs as methane storage sorbent

The applications of MOFs in methane storage have not received as much attention as those of hydrogen storage or carbon capture. Due to increasing awareness of the great potential of natural gas as an alternative energy fuel, the importance of methane storage in MOFs has been gradually realized, and some MOFs exhibit comparable or even better methane capacity compared to the best activated carbons. Several benchmark MOFs will be enumerated in the following section.

IRMOFs

The isorecticular MOFs (IRMOFs) represents a novel MOF family with facile functionalization and tunable pore spaces. The choice of linear ditopic carboxylates and $Zn_4O(COO)_6$ SBUs afford this family with potential in various applications. [26] Isorecticular chemistry has been widely applied in the design and synthesis of new MOF materials. [168-173] With the perspective of methane storage, the binding sites of IRMOF-1 (MOF-5, Figure I-8a), composed of 1,4-benendicarboxylate and $Zn_4O(COO)_6$ SBUs, are evaluated in detail. [174] The primary binding sites were determined near the Zn_4O cluster. (Figure I-8b). The well-defined orientation of methane indicates a strong interaction with methane molecules. At a high loading of methane, the extra methane molecules start to

either gradually occupy the hex sites and ZnO_2 sites or become trapped inside the cavity. (Figure I-8b-d).

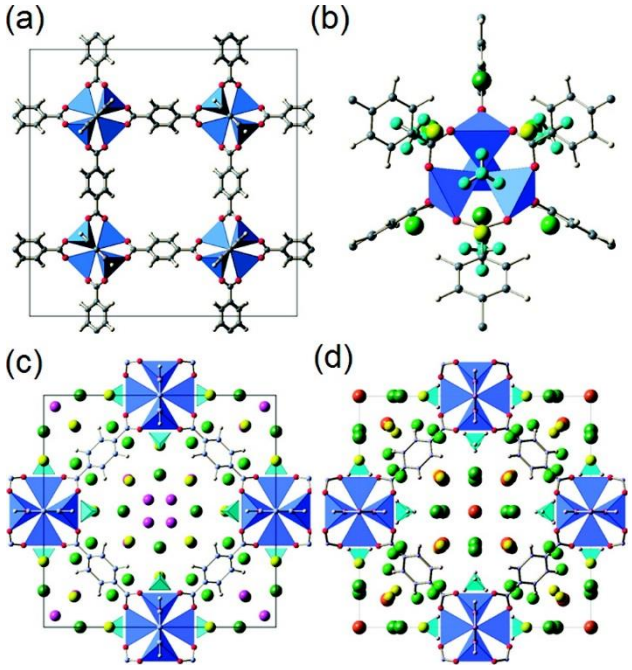

Figure I- 8. (a) Crystal structure of MOF-5. C in gray and D in white. (b) The methane adsorption sites in MOF-5: cup sites (cyan) and secondary hex (yellow) and ZnO_2 sites (green) (c) [001] view of the I4/mmm structure of MOF-5 with more CD4 loading at 80 K, extra methane (pink) were observed to populate near the center of the pores. (d) [001] view of the P4mm structure of MOF-5 with higher CD_4 loading below 60 K, confined methane sites (orange) were observed to align themselves along the c axis and further lower the symmetry to P4mm. Orientationally disordered methane molecules are shown as spheres for clarity (Reproduced with permission from reference [*174*]. Copyright 2009 American Chemical Society)

Another evaluation of three IRMOFs shows that the high surface area and hydrophobic nature of C_2H_4 endow IRMOF-6 with high excess methane uptake of 155 v(STP)/v at 36.5 bar. [26] Extended Raman spectroscopic studies on IRMOFs reveals that

the organic linker plays a critical role in the methane storage at high pressure. [175] In the Raman study, the interactions between methane and the framework downshift the symmetric stretching band of the methane molecule. Interestingly, the frequency shits are highly linker-dependent. Therefore, the organic linker is assigned as the predominant factor controlling the methane uptake in IRMOFs. The realization of linker effects also spurred a comprehensive computational simulation of many hypothetical IRMOFs. Based on the simulation, IRMOF-993, consisting of 9, 10-anthracene dicarboxylate linkers with an expected pore size of 6.3 x 6.3Å, is predicted to be a better sorbent than IRMOF-6. In fact, experimentally this gives rise to a distortion of $Zn_4O(COO)_6$ SBUs in the crystal structure. As a consequence, a microporous MOF synthesized as the experimental realization of the simulated IRMOF-993, namely PCN-13, displays a limited methane capacity within the confined pore spaces (~3.5 Å). [176]

MOF-74/CPO-27 Series

The M-MOF-74 series (M=Mg, Mn, Co, Ni, Zn), also known as CPO-27-M are a family of MOFs with high density of coordinative unsaturated metal centers (UMCs). [29,30,177-180] This isostructural series is composed of the infinite helical metal chain SBUs and 2, 5-dioxido-1,4,-benzenedicarboxylate (dhtp) with a 1D channel of 13.6 Å in diameter. The coordinated solvent molecules on the metal SBUs could be easily removed to expose the UMCs, which serve as the primary adsorption sites to the methane molecules through Coulomb interactions. [177] Among the excess adsorption measurements of this series of materials, Ni-MOF-74 exhibits the high value of ~190

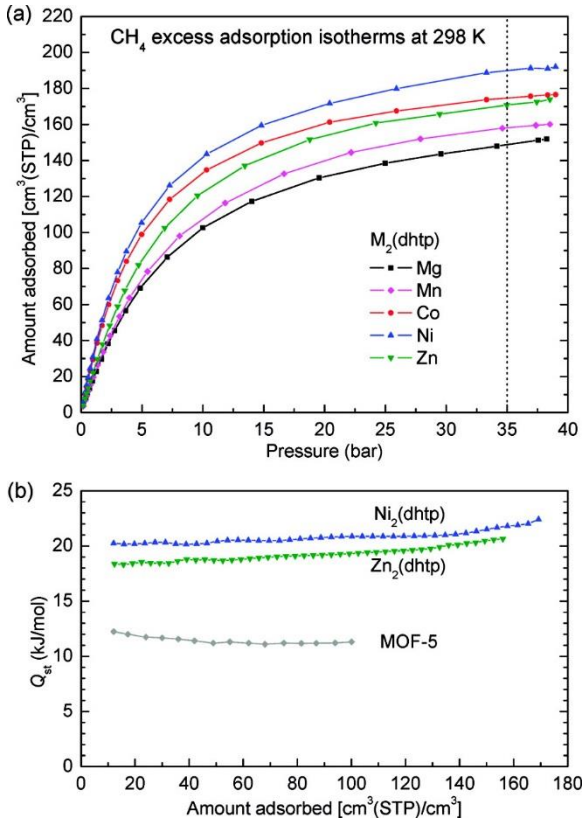

Figure I- 9. (a) Excess CH_4 adsorption isotherms of M_2(dhtp) at 298 K. (b) The experimental Q_{st} of Ni_2(dhtp) and Zn_2(dhtp). The Q_{st}'s of Mg_2(dhtp), Mn_2(dhtp), and Co_2(dhtp) fall between the two curves and, thus, are not shown for clarity. The Q_{st}'s of MOF-5 (from ref [182]) are also plotted for comparison. (Reproduced with permission from reference [177]. Copyright 2009 American Chemical Society)

cm^3 (STP) ·cm^{-3}(Figure I-9a). [181] All five MOFs have similar heat of adsorption in the range of 18 to 20 kJ mol^{-1} (Figure I-9b), which indicates no metal preference on the interactions between the UMCs and methane gas. This is ascribed to the fact that the large pore size increases the distance between the surface and methane but decreases the interaction potential between the two. Even though the large heat of adsorption is likely preferred for a stronger interaction, this trend does not apply to the overall deliverable capacity. A large amount of methane retention is witnessed at lower pressure, which is

unfavorable to methane delivery. As a result, the deliverable capacity can only be achieved that is less than half of the storage amount. [177] In addition to the primary binding site by UMCs (Figure I-10a), a secondary binding site is determined, where the methane molecules interact with both the framework and adjacent methane molecules (Figure I-10b).

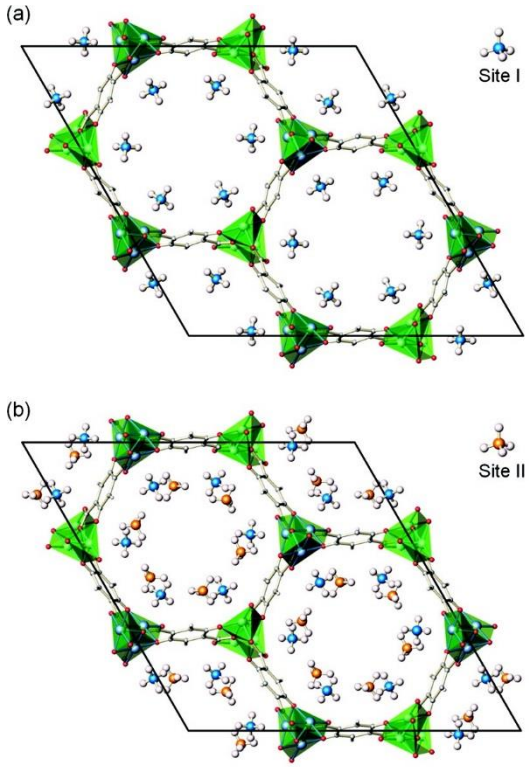

Figure I- 10. Crystal unit cell of Mg-MOF-74 with methane adsorbed on site I (a) and site II (b). (Reproduced with permission from reference [*177*]. Copyright 2009 American Chemical Society)

PCN-14

PCN-14 was widely cited as the record-holding MOF material for methane storage until 2013 with the total capacity of 230 cm^3 (STP) ·cm^{-3} at 298K and 35 bar. [183] PCN-14 is constructed through self-assembling of dicopper paddlewheel SBUs and 5,5'-(9, 10-anthracenediyl)diisophthalate. It is composed of squashed cuboctahedral cages and other small octahedral cages. The removal of terminal coordinated solvent of the paddlewheel yields nanoscopic cages with a significant amount of UMCs, which is a source of this material's high methane capacity. [184]

Computational studies based on Density Function Theory (DFT) have been applied to determine the potential methane adsorption sites of PCN-14. [185] Four major adsorption sites are identified: open copper sites, small cage window sites, small cage bottom sites, and small cage side window sites (Figure I-11). In addition, the large cage corner sites also make a contribution to the total methane capacity. Notably, another simulation study demonstrates that the methane position at the open metal sites is temperature-dependent.[186] The open metal site is densely populated at lower pressure but less populated at room temperature, which indicates that no energy barrier exists between the strong and weak adsorption sites.

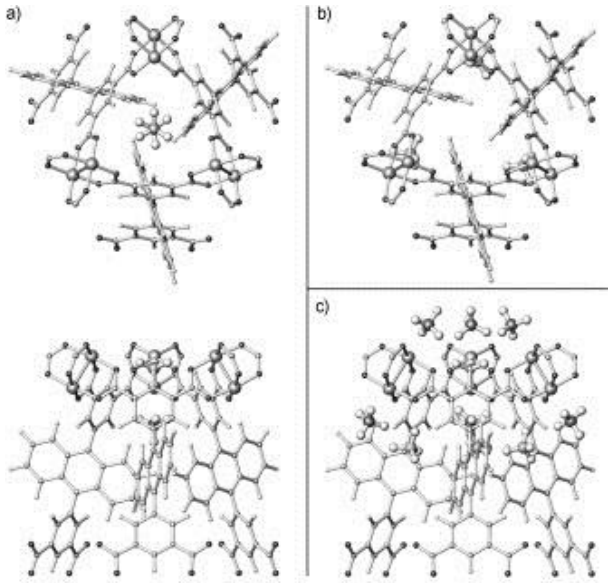

Figure I- 11. Partial structure of the DFT-optimized PCN-14 crystal with CH_4 molecules adsorbed at a) the small cage window site and the small cage bottom site (top and side views), b) the small cage side window site, and c) all four major adsorption sites, including the open Cu sites. (Reproduced with permission from reference [***185***]. Copyright 2010 John Wiley and Sons)

UTSA-20

Immobilizing high-density of open metal sites and constructing suitable pore spaces theoretically enhance the performance of methane storage. Realization of these two design principles to maximize the methane storage in new MOFs is an essential goal of this field. Based on these two principles, one experimental attempt produced UTSA-20 with high methane storage density ($0.222 g \cdot cm^{-1}$). [187] UTSA-20 is constructed from dicopper paddlewheel SBUs and 3,3',3'',5,5',5''-benzene-1,3,5-triyl-hexabenzates (bhb^{6-}). UTSA-20 contains one rectangular 1D channels of about 3.4 x 4.8 Å and a 1D cylinder of 8.5 Å in diameter along the c axis with exposed UMCs pointing into the pore. Because of the interplay of high density of UMCs and optimal pore spaces, the

total volumetric methane storage capacity can reach 195 $cm^3 \cdot cm^{-3}$ at 300K and 35 bar. Further computational simulation reveals the channel site is an additional primary adsorption site (Figure I-12 a). It is found that the size of the linker channel pore is suitable enough to sandwich the methane molecules between the surfaces of the two linkers (Figure I-12 b).

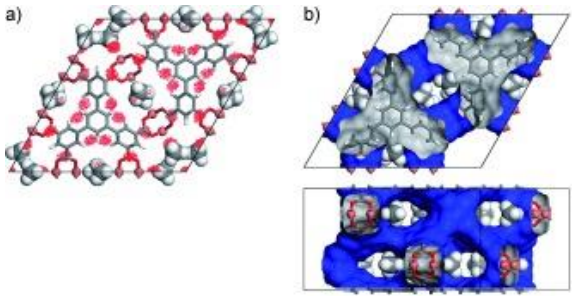

Figure I- 12. (a) Probability distribution of the CH_4 center of mass in UTSA-20 ([0 0 1] view), obtained from Grand Canonical Monte Carlo simulation at 298 K and 10 bar. The red regions represent the places where methane molecules are heavily populated in the MOF structure. Note that the open Cu site is pre-occupied with CH_4 molecules to focus our effort on the search for other strong methane adsorption sites. b) The pore surface of the interconnected channel pores in UTSA-20 with adsorbed methane at the linker channel site. The channel width along the c axis matches well with the size of the adsorbed methane molecules, leading to enhanced van der Waals interaction. (Reproduced with permission from reference [*187*]. Copyright 2011 John Wiley and Sons)

PCN-6X and NU-111

At the stage of exploring new material for gas storage, it is generally believed that increasing the surface area of MOF materials will correspondingly offer more interaction potential surfaces and enhance the gas storage capacity. Extensive efforts have been dedicated to the synthesis of new materials through linker extension.

However, linker extension can also produce several effects that can lower the suitability of the resulting MOF for methane storage, such as the undermining of stability and possible interpenetration. It has been suggested that use of metal-organic polyhedra as the building block of MOFs will not only increase the surface area and pore volume but also stabilize the large pore voids. [188] The *rht*-type frameworks (Figure I-13a) are one classical MOF family following the cage-based synthetic strategy. Cuboctahedral cages, assembled from 12 dinuclear paddlewheel SBUs and 24 isophthalate moieties, are commonly found in this *rht* family. Using this type of topology as a template, examples likes PCN-6X,[169] NU-11X,[189-191] and NOTT-10X[192,193] demonstrate high gas uptake with hierarchical pore cages containing UMCs.

The PCN-6X (X=1, 6, 8) series is realized by the combination of extended hexatopic carboxylates and dicopper paddlewheel SBUs. The size of T-O_h and T-T_d (Figure I-13b) is enlarged through linker extension, but this approach was not successful for cub-O_h (Figure I-13b). As expected, the Langmuir surface areas of the MOFs impressively increased to 6033 m^2 g^{-1}(PCN-68) .[169] At low pressure (<20bar), PCN-61 demonstrates the highest methane uptake due to the fact that small pore size provides more methane-framework overlapping. The volumetric excess methane uptakes of PCN-6X series are calculated to be 145, 110, and 99 cm^3 (STP) $\cdot cm^{-3}$ at 298K and 35 bar, respectively. As the pressure is increased, the effects of surface area and pore volume begin to dominate, with PCN-68 possessing the highest methane uptake.

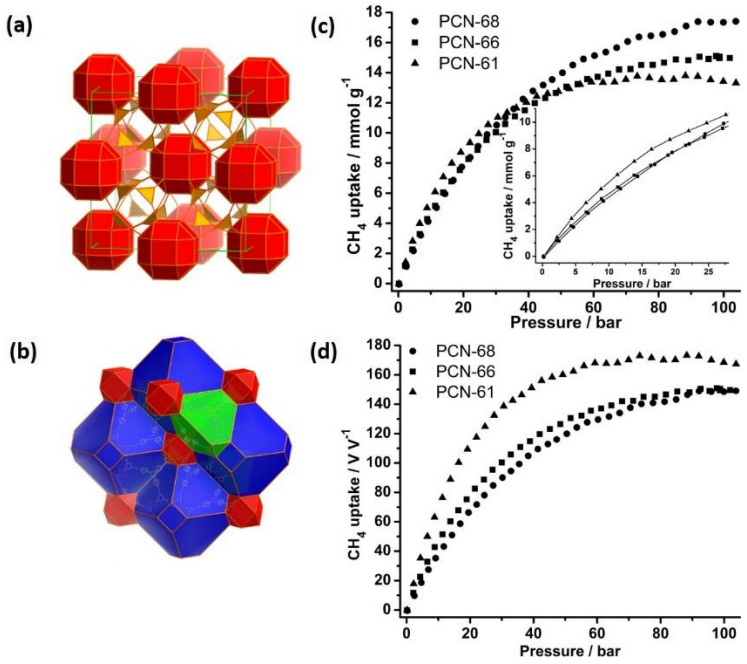

Figure I- 13. (a) **rht**-type framework and (b) 3D polyhedra of PCN-68; (c) gravimetric and (d) volumetric methane capacities in PCN-6X at 298K. The inset (c) shows the medium-pressure region enlarged (Reproduced with permission from reference [*169*]. Copyright 2010 John Wiley and Sons)

Continuous work on linker extension has been done to reach the record-high surface area with the design and synthesis of the NU-11X series. [189-191] Utilizing triple bonds as a spacer in the linker design, NU-111 was synthesized with a high BET surface area of 5000 m^2 g^{-1}. Strikingly, NU-111 displays equally high total gravimetric and volumetric methane capacities of 0.36 g g^{-1} and 206 cc/cc at 298K and 65 bar. [184]

HKUST-1

HKUST-1, one of the earliest MOFs, is reported as a 3D network consisting of dicopper paddlewheel SBUs and 1, 3, 5-benzenetricarboxylate linkers. [13] In the structure

of HKUST-1, there is a ~1nm-size channel and three different types of cages (Figure I-14a). The small octahedral cages with a diameter of ~5Å, a middle cuboctahedron cage with diameter ~10Å, and a large cuboctahedral cage with diameter of ~11Å are interconnected. Inconsistent high-pressure methane adsorption has been reported due to the variation of sample quality and the activation methods. [165,166,184,185] Recently, HKUST-1 was discovered to demonstrate a room-temperature total volumetric methane uptake of 230 cc(STP)/cc at 35 bar and 270 cc(STP)/cc at 65 bar. [184] The calculated deliverable capacity of HKUST-1 is 190 cc (STP)/cc (Figure I-14b).

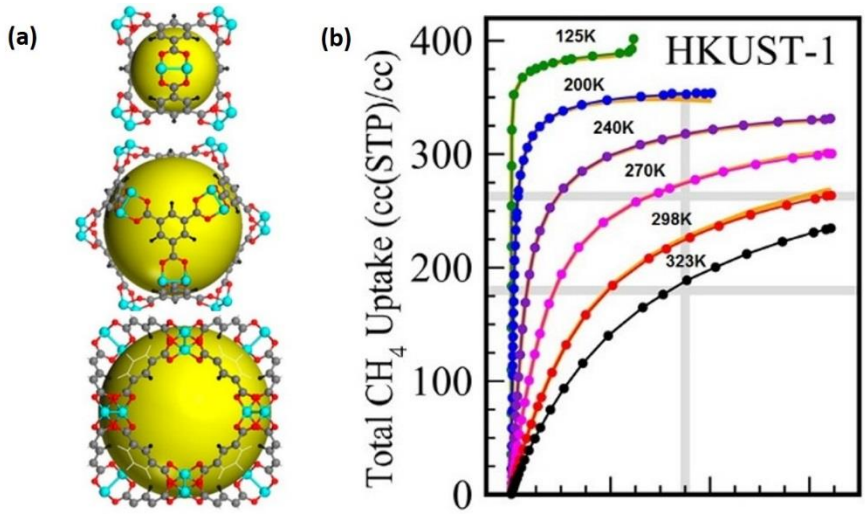

Figure I- 14. (a) the nanocages and crystal structures HKUST-1. The gray, black, red, cyan, and blue spheres represent carbon, hydrogen, oxygen, copper, and nitrogen atoms, respectively. (b) Total volumetric uptake isotherms at various temperatures for HKUST-1. The gray horizontal lines indicate the DOE's old and new volumetric targets, respectively. (Reproduced with permission from reference [184]. Copyright 2013 American Chemical Society)

The analysis from high-resolution neutron powder diffraction (NPD) reveals that the methane adsorption sites are sequentially filled at distinct preferred adsorption sites, and the open copper sites are still the primary adsorption position at low temperature. [194] The comprehensive study based on the NPD measurements and computation simulations discovers a second primary adsorption site at the window site of the small octahedral cage. [185] The close distance at 2.7~3.2 Å between the frameworks provides strong interactions to methane molecules.

USTA-7X(X=5, 6, 7, 8, 9)

Shortly after the realization of the high methane storage capacity in HKUST-1, more efforts on functionalization of isostructural MOFs have been made to improve the methane storage capacities. Significant improvement of methane capacity has been demonstrated on the incorporation of Lewis basic sites on the linkers of UTSA-7X (X=5, 6, 7, 8, 9). [195,196] The UTSA-7X materials are all isostructural to NOTT-101[192,193], which were constructed from copper paddlewheel and nitrogen-functionalized tetratopic carboxylate linkers (Figure I-15 a, b). Variation of the number of nitrogen sites, from pyridine, pyridazine, to pyrimidine groups on the designed linkers did not make any significant differences on the pore volume, BET surface area or crystal densities. Moreover, the open copper sites still serve as the primary adsorption sites at 5 bar. In this case, the effect on the methane storage capacities at 5 bar can be neglected. Strikingly, the incorporation of Lewis basic nitrogen sites on the linkers significantly increase the methane uptake at 65 bar (Figure I-15c), which consequently enclose

UTSA-76 with the record methane storage deliverable capacities of 197 $cm^3 \cdot cm^{-3}$. DFT calculations reveals that the Lewis basic nitrogen sites (pyrimidine) of UTSA-76 provides a shallower energy barrier for hydrogen atoms to rotate in the center ring compare to that of benzene ring in NOTT-101. [69] These findings are all in good agreement to the results from neutron scattering studies, in which the rotation motion of the USTA-76 central ring requires much lower temperature compare to that of NOTT-101. [69] As a result, the Lewis basic nitrogen sties in UTSA-76 provides an enhanced van der Waals interaction at higher pressure and displays a higher CH_4 affinity.

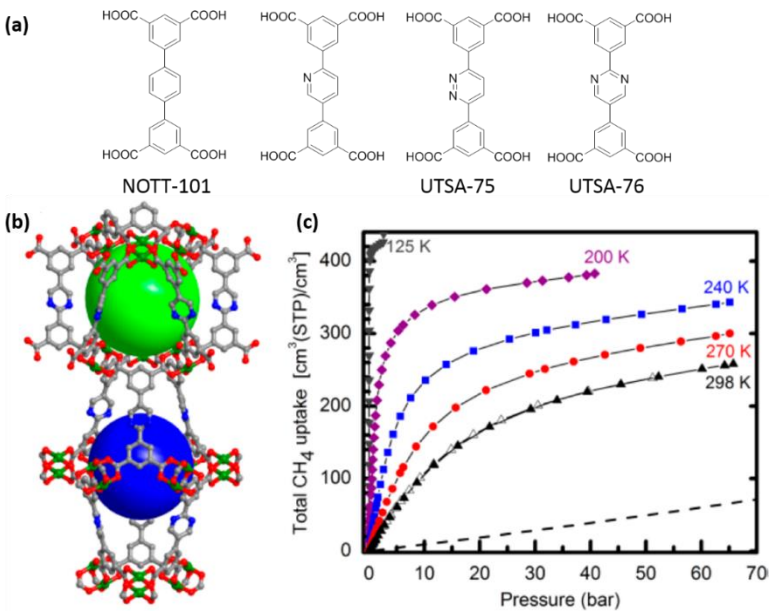

Figure I- 15. (a) the schematic structure of the organic linker design for the construction of NOTT-101 and UTSA-7X; (b) Two cages of about 10.2 and 9.6 ×22.3Å, respectively in UTSA-76; (c) temperature-dependent high-pressure methane sorption isotherms of UTSA-76 (black dash curve represents the stored methane in a high pressure gas tank) (Reproduced with permission from reference [*195*]. Copyright 2014 American Chemical Society)

Zr-MOFs

When subjecting the porous materials to numerous adsorption/desorption cycles, material stability and resistance to impurities of natural gas (water, hydrogen sulfide, and other hydrocarbons), must be considered. The discovery of the zirconium-based MOF UiO-66 has inspired the investigation of stable MOFs due to the high inertness of Zr-oxoclusters.[15] Their excellent thermal, chemical, and mechanical stability afford Zr-based MOFs great potential for methane storage. Computational simulation reveals UiO-67 shows the highest storage capacity of 146 cm^3 (STP) $\cdot cm^{-3}$ in a series of isoreticular Zr-based MOFs. [197] With the goal to identify and synthesize a stable zirconium-based MOFs, another screening test is done on the MOFs featuring $(Zr_6O_4)(OH)_4(CO_2)_n$ SBUs.[198] Among those hypothetical MOFs, the ones with alkyne groups adjacent to the zirconium corner allow efficient packing of methane and ultimately provide high methane capacities. Typically, NU-800, using a 1,4-benzenedipropiolate linker, exhibits volumetric deliverable capacities of 167 cc(STP)/cc, which is higher than those of PCN-14[199] and UTSA-20. [199] In addition, no sample degradation is observed over a large number of gas adsorption cycles. The superior stability definitively shows the promise of Zr-based MOFs as methane sorbents.

1.4.4 Optimal Design Characteristic for Methane Sorbents

As more porous MOFs are being realized with improved gravimetric and volumetric methane capacity, there is a strong need to consider the factors that can dramatically affect the ultimate performance of the material for methane storage. The

deliverable capacity is the dominant factor for the ultimate adoption and use of MOFs for on-board vehicle natural gas storage.

Computational simulations based on DFT can generally provide some insights directing the design of new MOF sorbents. Pore sizes centered around ~4Å and ~8 Å in MOFs are optimal for methane storage at 298K and 35 bar based on the high-throughput computational simulations.[200] The pore size of MOFs has a strong influence in the determination of the deliverable capacity through its correlation with the heat of adsorption and pore volume available for methane occupancy. [201] In general, the pore size ~4Å is just right to provide strong enough affinity to uptake methane during the adsorption process yet weak enough to release it during desorption. As the pore size of MOFs go beyond ~4Å, the wasted volume increase until the pore size of ~8Å, which is suitable to accommodate two methane molecules. In addition, increasing the volumetric surface area exhibits a positive correlation to the raise of volumetric methane capacity. [173,184,202] Additionally, the optimal void fraction for MOFs with high methane uptake is suggested about 0.8. [200] Larger void fraction provide less overlap between the internal surface and the methane molecules.

From the perspective view of experimental studies**,** cage-based MOFs commonly demonstrate strong framework-methane interactions. If taking advantages of the fact that a structural priori could be conceived through proper modulation of SBUs and linkers**,** topology-guided synthesis offers opportunities to achieve a number of cage-based MOFs. However, proper design of linker and SBUs are also required to prevent possible interpenetration, which not only reduce the pore volume and surface area but

also increase the crystalline density. [201] Besides, the functionalization of the linker with lipophilic or small and polar groups are desired to enhance the methane performance. [200,203,204] In the adsorption process, uncoordinated metal centers display the major role in the contribution of the total methane capacity. Therefore, design MOFs with high density of UMCs showcase the success to achieve high methane capacity. However, a portion of methane will be retained at low pressure and cannot be removed during the desorption process. As a consequence, the deliverable capacity will certainly decrease. Thus, a clear tradeoff between UMCs and deliverable capacity must be taken into consideration.

1.4.5 Summary

After detailed analysis of the adsorption sites in each MOFs, a couple of optimal design characteristics for future development can be concluded. MOFs definitely show promise in me-thane storage. However, the research area of MOFs in the application of me-thane storage is still widely underexplored. Considering the complete ANG storage system, factors such as mechanical stability, heat capacity, and thermal conductivity and stability are critical to the practical application of MOFs as methane sorbents. Additionally, the dynamic adsorption process based on experimental measurements over a large range of pressure has not been extensively studied. It is apparent that collaboration between chemists, engineers and even industrial experts is necessary to drive this technology into further stages of development with the goal of widespread use for natural gas vehicles.

CHAPTER II

TOPOLOGY GUIDED DESIGN OF AN ANIONIC BOR-NETWORK FOR PHOTOCATALYST ENCAPSULATION *

2.1 Introduction

The utilization of metal-organic frameworks (MOFs) for heterogeneous catalysis has been a hot topic in the past two decades.[205-209] MOFs are well-defined structures that can achieve exceptionally high porosity, which endows them with the capacity of hosting not only densely packed but also precisely positioned active sites for heterogeneous catalysis. To realize such an assembly of "molecular reactors", a variety of suitable MOF scaffolds to accommodate catalytic centers of various sizes are needed.[210,211] A significant amount of effort has been dedicated to rationally design MOFs with desired porosity and controlled cavity size and shape to tune the environment surrounding the active center of a catalyst.[208,209,212] Most recently, the rapid development of MOFs with permanent mesoporous cavities has prompted the study of encapsulation of bulky catalysts and ensuing catalytic properites.[212] The widely studied photoactive cation $[Ru(bpy)_3]^{2+}$ (bpy = bipyridine), in particular, is such a catalyst, which displays potential in both light harvesting and photocatalysis.[213] The difficulty in the recycling of photocatalyst, however, has delayed its practical applications.[214,215] One

* Reproduced with permission from "Topology-Guided Design of An Anionic bor-Network for Photocatalyst $[Ru(bpy)_3]^{2+}$ Encapsulation" by Wang, X.; Lu, W.; Gu, Z.-Y.; Zhang, W.; Zhou, H.-C. *Chem. Commun*., **2016**, 52, 1926-1929, copyright 2016 by The Royal Society of Chemistry. (http://pubs.rsc.org/en/Content/ArticleLanding/2016/CC/c5cc08614k#!divAbstract)

approach to circumvent this issue is to design and synthesize heterogeneous photocatalysts, in which the catalytic centers are trapped in the solid form. $[Ru(bpy)_3]^{2+}$ encapsulation in MOFs have been studied through ligand design [210,211,216-220] and *in situ* entrapment.[214,221-224] However, encapsulation of $[Ru(bpy)_3]^{2+}$ through post-synthetic ion exchange is relatively understudied, which is puzzling because the photocatalytic cation can be encapsulated easily and effectively.

Ionic MOFs are porous crystalline materials having either positively- or negatively-charged frameworks with trapped counterions inside the cavities. The charged frameworks provide strong electrostatic interactions to the guest molecules and, in most cases, function as templates for post-synthetic ion exchange;[51,225] these unique properties make ionic MOFs promising for chemical sensing[226,227] or ideal as highly efficient heterogeneous matrices.[228,229] Nevertheless, the incorporation of large photoactive species has rarely been studied likely due to the lack of ionic MOFs with large pore apertures. [55,230] Only a few ionic MOFs with cavities at mesoporous scale have been reported to date. [231,232]

General approaches to obtain MOFs with desired topology and a larger cavity involve extension of the organic linkers. In this work, a careful inspection of the net topology of the target framework may provide more insights into rational material design. With regard to ionic MOFs, indium-based MOFs are commonly constructed with either cationic building blocks $[In_3O(COO)_6]^+$ or anionic building blocks $[In(COO)_4]^-$.[48-59] For the sake of incorporation of cationic $[Ru(bpy)_3]^{2+}$, $[In(COO)_4]^-$ is our choice. Topologically, the $[In(COO)_4]^-$, a 4-connected tetrahedral node, could potentially form

various high-symmetry nets when combined with other highly symmetric nodes.[233] The extension of btc (btc = 1,3,5-benzenetricarboylate) could theoretically produce an isorecticular ionic MOFs with larger cavities.[53,232] Therefore, tritopic carboxylates are chosen as the inorganic building units. Herein, we report the synthesis of an anionic MOF PCN-99 (PCN = porous coordination polymer) with a pore cavity at the mesoporous scale, spontaneous encapsulation of $[Ru(bpy)_3]^{2+}$ through ion exchange, and its photocatalysis in oxidative hydroxylation of arylboronic acids.

2.2 Experimental Section

2.2.1 Materials and Instrumentation

Materials

N,N-dimethylformamide (DMF), ethanol, $InCl_3 \cdot xH2O$, tetrafluoroboric acid, and tris(2,2'-bipyridyl)dichlororuthenium(II) hexahydrate were purchased from either Alfa Aesar or Sigma Aldrich. Unless otherwise noted, all chemicals were used without further purification.

Instrumentation

Synchrotron powder X-ray diffraction (PXRD) was carried out with Bruker D8-Discover diffractometer equipped with a Mo sealed tube (λ = 0.72768Å) on the beamline 17-BM at the Advanced Photon Source, Argonne National Laboratory. In-house powder X-ray diffraction (PXRD) was carried out on a Bruker D8-Focus Bragg-Brentano X-ray powder Diffractometer equipped with a Cu sealed tube (λ = 1.54178) at 40 kV and 40

mA. UV-Vis spectra were recorded on Shimadzu UV-2450 spectrophotometer. Fluorescence spectra were recorded on Horiba Fluorolog spectrofluorometer. Thermogravimetric analyses (TGA) were carried out on a Shimadzu TGA-50 thermal analyzer from room temperature to 800 °C at a ramp rate of 2 °C/min in a flowing air atmosphere. Nuclear magnetic resonance (NMR) data were collected on a Mercury 300 spectrometer. Single Crystal XRD data were collected with a Bruker APEX II diffractometer and processed using the program SAINT routine. The structure was solved by direct methods of SHELXL[234] program and refined by full-matrix least squares techniques using the SHEXL[235] program and WINGX.[236] Contributions to scattering due to these solvent molecules were corrected with the SQUEEZE,[237] part of the PLATON package, and the structures were then refined again using the data generated. Solvent molecules are not represented in the unit cell contents (chemical formula) in the crystal data. The topology was calculated using the TOPOS[238] software.

2.2.2 Ligand Synthesis

Step 1. Synthesis of trimethyl 4,4',4''-(benzene-1,3,5-triyltris(azanediyl))tribenzoate (c)

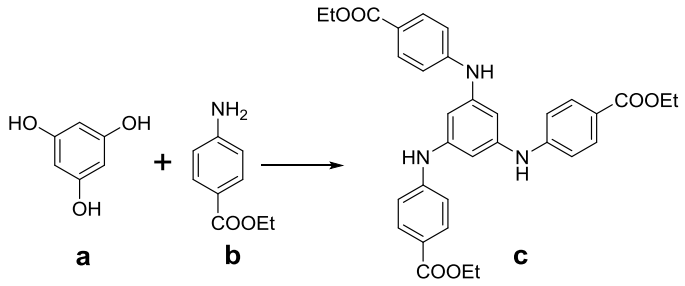

Scheme II- 1 Synthesis of triethyl 4,4',4"-(benzene-1,3,5-triyltris(azanediyl))tribenzoate(c).

Synthetic procedure of **c** was followed according to the literature.[239]

Step 2. Synthesis of 10,15-dihydro-5H-diindolo[3,2-a:3',2'-c]carbazole-3,8,13-tricarboxylic acid (H_3DCTA)

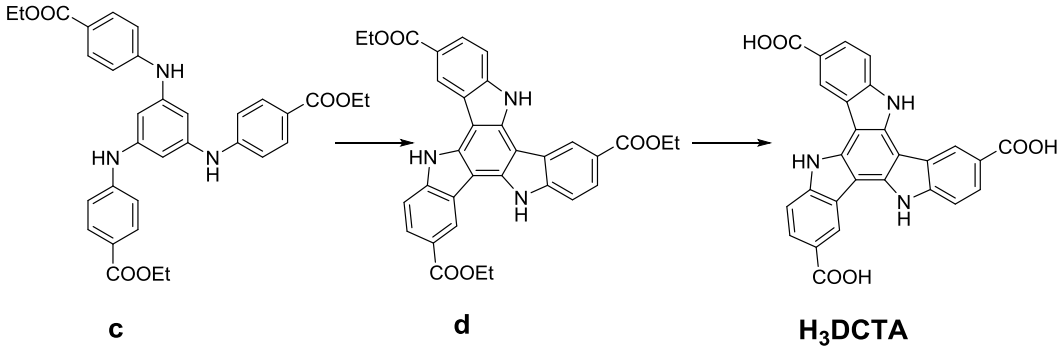

Scheme II- 2 Synthesis of H_3DCTA.

Synthesis of **d**: 0.03 g (0.09 mmol) $Pd(CF_3COO)_2$, 1 g **c** and 20 mL acetic acid in 50mL round bottom flask with the eliminator. Temperature up was carried out to 100 degree, blowing and agitating air in the system of reaction with an air pump for 7 hours.

An exception carries out the crystal which deposits after cooling, washed with acetic acid and obtained the compound **d** (0.63 g, 74%) ^{1}H-NMR (DMSO-d_6) 1.44(9H, t) , 4.45 (6H,dd) 7.84(3H, d), 8.07(3H, dd), 9.38(3H, s), 12.67(3H, s),

Synthesis of H_3DCTA: Compound **d** (1g) and 1.5g KOH were suspended in 20 mL EtOH, and refluxed for 2 Hours. After cooling, the pH value was adjusted to approximately 2 using hydrochloric acid. The resulting precipitate was collected by centrifugal, washed with water, and dried under vacuum to give H_3DCTA (0.63 g, 74%). ^{1}H-NMR (DMSO-d_6): 7.81(3H, d), 8.07(3H, dd), 9.37(3H, s), 12.61(3H, s).

2.2.3 MOF Synthesis

$InCl_3 \cdot xH_2O$ (20 mg) and H_3DCTA (5 mg, 0.010 mmol) was immersed in 1.8 mL 4, 4'-dimethylformamide (DMF), 0.2 mL ethanol and 2 drop HBF_4(40% min v/v aq solution) in a 4 mL Pyrex vial. After sonication for 5 min, the mixture was moved to a pre-heated 120 ^{o}C oven for 4 days. After cooling down under room temperature and DMF wash, colorless cubic crystals was harvested (33% yield based on ligand).

2.2.4 Structure Determination of Single Crystals

The as-synthesized PCN-99 was taken directly from the solution, loaded in the oil on a loop, and further mounted for single crystal X-ray data collection. Diffraction patterns were measured on a Bruker Smart Apex diffractometer equipped with a Mo-Kα sealed-tube X-ray source (λ = 0.71073 Å) under protection of N2 stream at 110 K. The data frames were recorded using the program APEX2 and processed using SAINT

routine within APEX2. The data were corrected for absorption and beam corrections based on the semi-empirical technique as implemented in *SADABS*. All structures were solved by direct methods using *SHELXS* and refined by full-matrix least-squares on F2 using *SHELXL* software.

Non-hydrogen atoms were refined with anisotropic displacement parameters during the final cycles, whereas organic hydrogen atoms were located with isotropic displacement parameters set to 1.2 × *U*eq of the attached atoms. Attempts to locate and refine the strong solvent peaks were successful, but contributions to scattering due to those highly disordered solvent molecules were removed using the SQUEEZE routine of PLATON; structures were then refined again using the data generated.

The detailed information about the solution and refinement of the single crystal structures can be found in the electronic supplementary materials of this manuscript. [240]

2.2.5 Loading Process for PCN-99

Part a. The congo red solution and $Ru(bpy)_3Cl_2 \cdot 6H_2O$ were prepared as 1mmol/L in DMF solution, respectively. One vial of PCN-99 were treated with 200 μL those stock solution before the UV-absorption measurement.

Note: $[Ru(bpy)_3]^{2+}$, has a dimension of 1.15 X 1.15 X 1.15 nm, while congo red is 0.7 X 2.5 nm. The channel size of 2.2 nm is capable to accommodate the diffusion of the congo red solution and $Ru(bpy)_3Cl_2 \cdot 6H_2O$. [241]

Part b. The $Ru(bpy)_3Cl_2 \cdot 6H_2O$ (10 mg, 0.021 mmol) was dissolved in 10 mL DMF as the stock solution. This stock solution was incubated with as-synthesized PCN-99 (5 mg) at room temperature and gently shaken for 40 min. The resulted $Ru(bpy)_3$@PCN-99 was then centrifuged and the supernatant was carefully removed for UV-vis measurement. According to the Beer-Lambert Law, the absorption of the band (454 nm for $[Ru(bpy)_3]^{2+}$) was proportional to the concentration of $[Ru(bpy)_3]^{2+}$. Therefore, the loading amount was calculated by subtracting the concentration of $[Ru(bpy)_3]^{2+}$. in the supernatant from the free-MOF amount. The uptake reached the saturation in 6 hr until the band of 454 nm no longer changed any more. The mole absorption coefficient was determined by preparing four different concentrations to derive a standard curve which gave $\varepsilon = 13372\ M^{-1}\ cm^{-1}$. After wash with DMF several times, $Ru(bpy)_3$ @PCN-99 was ready to use for further analysis.

2.2.6 TGA Data Collection

~10 mg as-synthesized PCN-99 exchanged with acetone for three times, and then dried in the oven overnight. The sample was later transferred to the sample holder of TGA instrument. The measurement was performed under nitrogen flow with speed of 10 ^{O}C/min.

2.2.7 General Procedure and NMR Spectral Data of Products

According to the literature[242],a mixture of 4-methoxycarbonylphenylboronic acid **1a** (90 mg, 0.50 mmol), $Ru(bpy)_3Cl_2 \cdot 6H_2O$ (2 mol%) in 5mL DMF with $^{i}Pr_2EtN$ (1

mmol) was stirred at room temperature under visible light radiation in open air. After 48 hr, the reaction and evaporated to remove the dryness. The residue was purified with column (EtOAc :Hexanes= 3:7) to give the pure product **2a**.

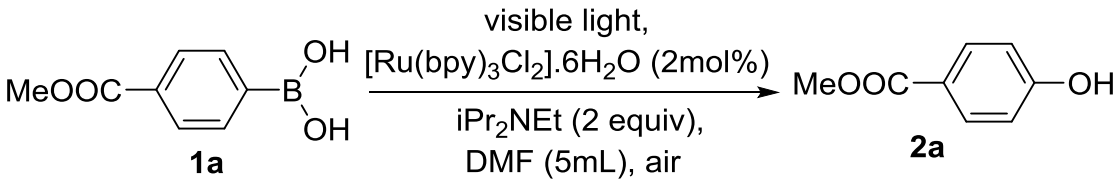

Scheme II- 3 Catalysis of 4-methoxycarbonylphenylboronic acid.

4-methylphenol (2b)

Similar reaction was prepared based on general procedure with the 4-methylphenyl boronic acid (68 mg, 0.50 mmol).

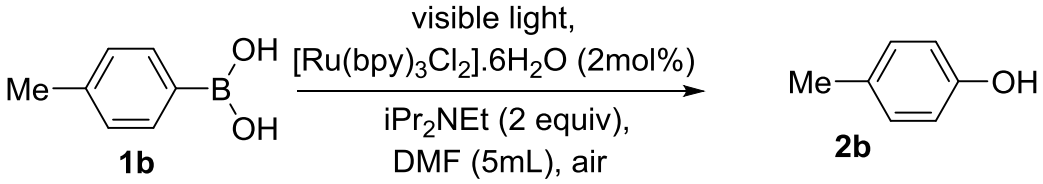

Scheme II- 4 Catalysis of 4-methylphenylboronic acid.

4-Hydroxybenzaldehyde (**2c**).

Similar reaction was prepared based on general procedure with the 4-formylphenyl boronic acid (75mg, 0.50 mmol).

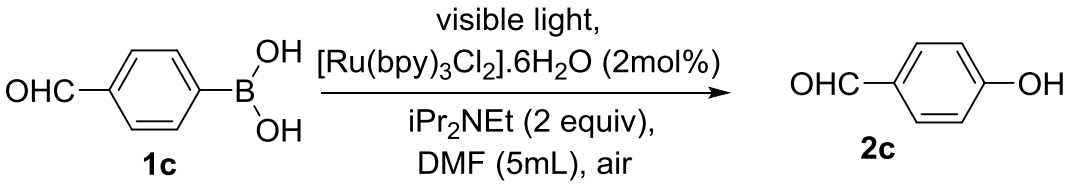

Scheme II- 5 Catalysis of 4-formylphenyl boronic acid.

2.2.7 Screening and Control Experiments of Catalytic Activity of Ru(bpy)$_3$@PCN-99 in Oxidation of 4-(methoxycarbonyl)phenyl)boronic Acid

Screening and control experiments (Table II-1) was demonstrated using 4-(methoxycarbonyl)phenyl)boronic acid as the substrate according to the general procedure in Section 2.2.6, where "+" means including, while "-" means excluding.

Table II- 1 Screening and control experiments of Ru(bpy)$_3$@PCN-99 as catalysis [a].

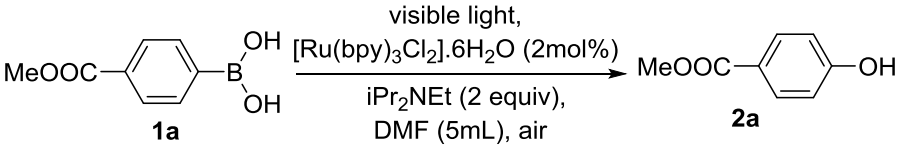

Entry	Ru(bpy)$_3$@ PCN99	H_3DCTA	In $(NO_3)_3$	PCN-99	$[Ru(bpy)_3]Cl_2 \cdot 6H_2O$
1	+	-	-	-	-
2	-	+	-	-	-
3	-	-	+	-	-
4	-	-	-	+	-
5	-	+	-	-	+

2.3 Results and Discussion

2.3.1 Geometrical Analysis

Initially, the development of TATB (4,4',4''-s-triazine-2,4,6-triyl-tribenzoate), a trigonal planar linker, with 4-connected $[In(COO)_4]^-$ was attempted in the expectation of forming such an anionic MOF with large cavities, but to no avail. Similar endeavours have been reported with the achievement of a microporous anionic MOF.[243] This could be ascribed to the free rotation of carboxyphenyl rings in TATB, which prevents the three carboxylates from staying coplanar with each other (Figure II-1). Compared to the orientation preference of TATB, BTB (4,4',4''-benzene-1,3,5-triyl-tribenzoate) is even less likely to have a coplanar conformation. Under the combination with $[In(COO)_4]^-$, three nets were interwoven to provide a **jcy** framework with micropores.[51] In order to minimize the structural variation caused by the flexibility of linkers, a strictly coplanar conformation must be adopted for the linker configuration. Therefore, guided by topological analysis using the known connectivity of metal nodes, a tritopic ligands 10, 15-dihydro-5H-diindolo[3,2-a:3',2'-c]carbazole-3,8,13-tricarboxylate acid (H_3DCTA) was designed and synthesized.

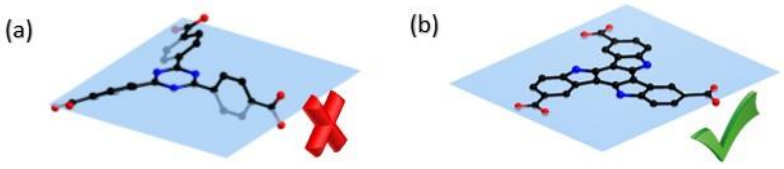

Figure II- 1. Analysis of TATB (left) and DCTA (right).

2.3.2 Characterization of Crystal Structures

The single crystal of PCN-99 is colorless cube crystal. In PCN-99, each indium center is coordinated by four carboxylate groups of DCTA linkers, making the framework negatively charged (Figure II-2). The counterions interact weakly with the framework and can be easily exchanged.[55,228]A small octahedral cage is formed by six indium units and four DCTA linkers (Figure II-2). In addition, a large cuboctahedral cage comprised of twelve indium units and four linkers leads to a mesoporous cavity. Such a large pore is rarely reported for indium-based ionic MOFs. [231,232] Moreover, this cage-based structure can help minimize the leaching of guest molecules, which was found in some MOFs used for enzyme immobilization.[244] At the topological level, PCN-99 adopts the bor topology, in which the connection of the coplanar tritopic linker DCTA and the $[In(COO)_4]^-$ node give rise to not only large cages but also 1D channels (Figure II-2). This eases the diffusion of the substrates during catalysis. Overall, this unique structural architecture imparts PCN-99 great potential in large catalyst encapsulation.

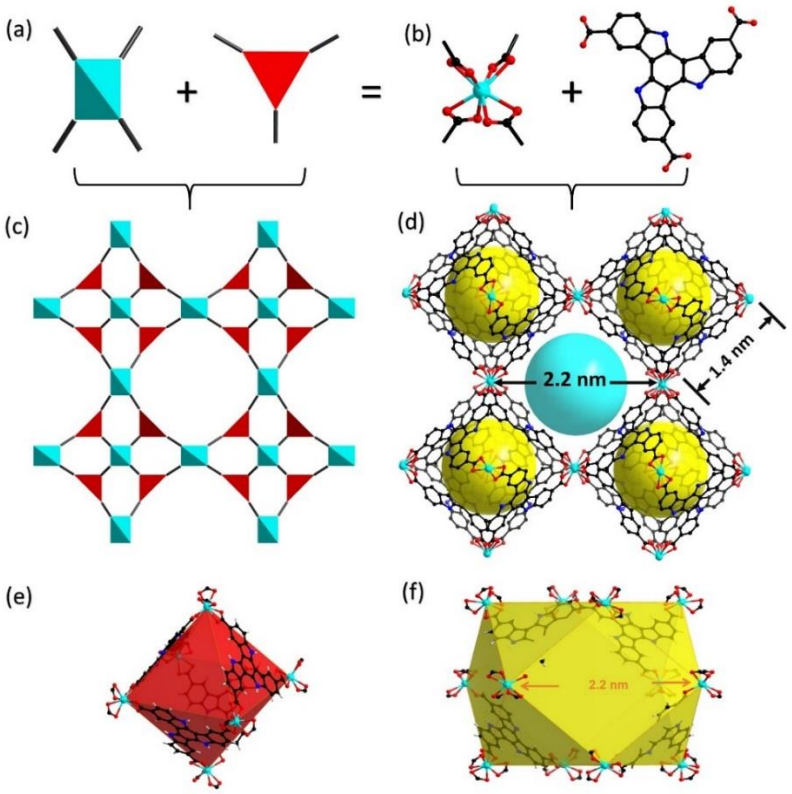

Figure II- 2. Assembly of a T_d and coplanar trigonal nodes into a bor network; a), b) combination of 4-connected $[In(COO)_4]^-$ node（blue tetrahedral） and 3-conneted DCTA linker (red triangle) produces PCN-99; e) octahedron and f) cuboctahedron cages in PCN-99.

2.3.3 Characterization of Ionic Nature of PCN-99

To evaluate the anionic nature of PCN-99, single crystals of PCN-99 were immersed in solutions of $[Ru(bpy)_3]Cl_2$ or congo red, respectively (Figure II-3). The colour of the congo red solution was retained after 24 hours, while the colour of the $[Ru(bpy)_3]^{2+}$ solution gradually turned from yellow to colourless, and the originally colourless PCN-99 at the bottom of vial turned orange. The decrease of $[Ru(bpy)_3]^{2+}$

concentration, a dramatic drop at 454 nm, is demonstrated by UV-Vis absorption spectra, which is consistent with the trapping of cationic $[Ru(bpy)_3]^{2+}$ in the pores of

PCN-99. Powder X-ray Diffraction (XRD) studies showed evidence that the crystallinity was well preserved during and after the guest inclusion (Figure II-3). The high absorption selectivity of $[Ru(bpy)_3]^{2+}$ owing to the strong electrostatic interactions over congo red was also witnessed in a equimolar-mixed environment. The diminishing absorption peak at 454 nm corresponds to the inclusion of $[Ru(bpy)_3]Cl_2$ while the consistent peak at 530 nm indicated the retention of congo red in the solution (Figure II-3).

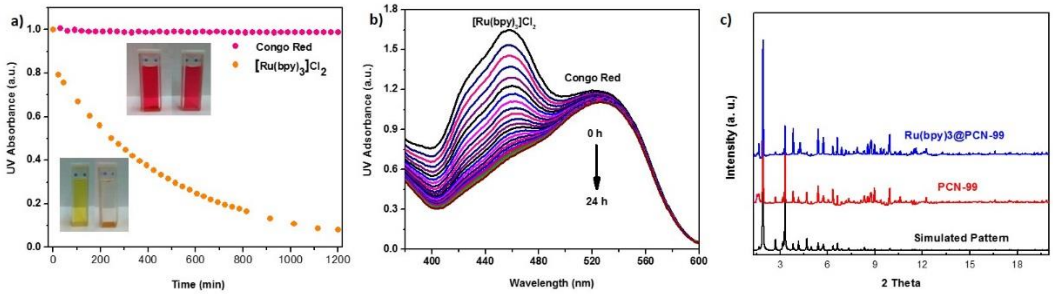

Figure II- 3. a) UV-Vis absorbance changes over time for PCN-99 in solutions of congo red and $[Ru(bpy)_3]Cl_2$, respectively; b) UV-Vis absorbance for PCN-99 in a mixture of $[Ru(bpy)_3]Cl_2$ and congo red in an equal molar; c) PXRD spectra of simulated pattern from crystal structure (black), as-synthesized PCN-99 (red), and $Ru(bpy)_3$@PCN-99 (blue)

2.3.4 Heterogeneous Catalysis of $Ru(bpy)_3$@PCN-99

Arylphenols have been recognized as versatile intermediates in the chemical and pharmaceutical industry. Since $[Ru(bpy)_3]Cl_2$ has displayed excellent catalytic activities in aerobic oxidative hydroxylation of arylboronic acids, [210,242] it is interesting to apply $Ru(bpy)_3$@PCN-99 in this type of chemistry as a heterogeneous catalyst within the scope of arylboronic acids . All conversions of the substrates exhibited relatively high efficiency (Table II-2). Due to the fact that the framework structure impedes the access of substrates to a certain extent, so a reduced catalytic activity was observed for $Ru(bpy)_3$@PCN-99 compared to $[Ru(bpy)_3]Cl_2$ in homogenous solution (Table II-2).

Table II- 2. Visible-light-induced aerobic oxidative hydroxylation of arylboronic acid.

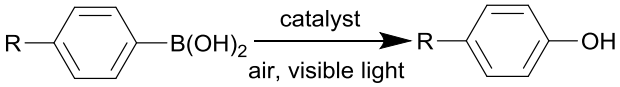

Entry	R-	Catalyst	Conversion
1	COOMe	$[Ru(bpy)_3]Cl_2$	71.9%
2	COOMe	$Ru(bpy)_3$@PCN-99	59.0%
3	Me	$[Ru(bpy)_3]Cl_2$	89.4%
4	Me	$Ru(bpy)_3$@PCN-99	65.4%
5	CHO	$[Ru(bpy)_3]Cl_2$	70.8%
6	CHO	$Ru(bpy)_3$@PCN-99	45.9%

After the catalysis, PXRD of $Ru(bpy)_3$@PCN-99 before and after before and after catalysis approved that the crystallinity was maintained (Figure II-4) . Similar observation was found through the SEM images (Figure II-4).

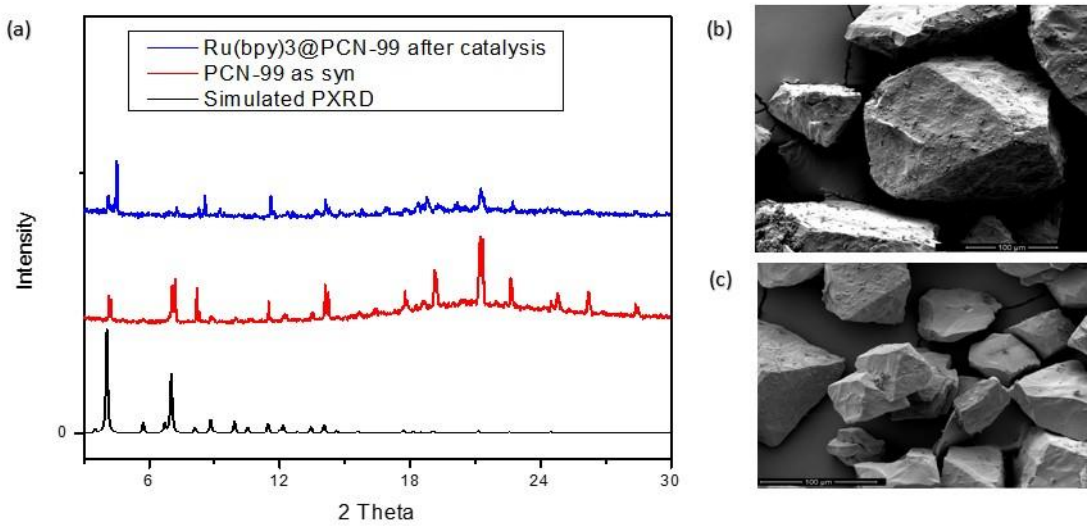

Figure II- 4. a) PXRD patterns of $Ru(bpy)_3$@PCN-99 collected before and after the catalysis. SEM images before (b) and after (c) the catalysis.

2.3.7 Screening and Control experiments of Catalytic Activity of $Ru(bpy)_3$@PCN-99 in Oxidation of 4-(methoxycarbonyl)phenyl)boronic Acid

The absence of product **2a** excluded the influences from the interference of the H_3DCTA (Table II-1, Entry 2), the Lewis acidity of indium (III) (Table II-1, Entry 3), and the framework itself (Table II-1, Entry 4). Thus, all the catalytic behaviour were dedicated solely to the $[Ru(bpy)_3]^{2+}$ components in $Ru(bpy)_3$@PCN-99. (Table II-1,

Entry 1). In addition, no significant effect was observed caused by the electron-rich ligand on the photocatalysis of $[Ru(bpy)_3]^{2+}$ (Table II-1, Entry 5 vs 71.9% for just $[Ru(bpy)_3]^{2+}$). In the catalysis of $Ru(bpy)_3$@PCN-99, the influence of the Lewis acidity of metal cluster was excluded As a result, the catalytic activity of $Ru(bpy)_3$@PCN-99 was due to the efficient encapsulation of $[Ru(bpy)_3]^{2+}$ active sites within the unique bor topology.

2.3.9 Recyclability of $Ru(bpy)_3$@PCN-99

Comparing the Ru complex content before and after the first catalysis, 9.48% $Ru(bpy)_3^{2+}$ was found in the solution after the first use of $Ru(bpy)_3$@PCN-99 system, which could be from partial decomposition of MOFs under basic conditions. A separate control experiment (R=COOMe) with leached $Ru(bpy)_3^{2+}$ ended up with 13% product yield. However, most of the $Ru(bpy)_3^{2+}$ was still preserved in PCN-99. The second use of $Ru(bpy)_3$@PCN-99 for second use end with only greatly decreased leaching of 4.76% but comparable product yields (Table II-3).

2.3.10 Reversible Capture and Release of $Ru(bpy)_3^{2+}$ in PCN-99

For practical applications, a reversible ion-exchange process is commonly required.[55,245] Modulation of the relative concentration of different guest molecules shifts the dynamic equilibrium and consequently leads to release and recapture of the original guests.[55] The release experiment was performed on the fully loaded $Ru(bpy)_3$@PCN-99. The release of $[Ru(bpy)_3]^{2+}$ was triggered by adding the same volume of saturated

$NaNO_3$ solution (Figure II-5) . The virtually complete release of $[Ru(bpy)_3]^{2+}$ could be achieved by increasing the volume of saturated $NaNO_3$ solution to 20 mL from the original 10 mL after 23 hours with the assist of gentle stirring (Figure II-5). As the $[Ru(bpy)_3]^{2+}$ was replaced by the sodium ions, the yellow colour of the crystals gradually faded.

Table II- 3. Recyclability of $Ru(bpy)_3$@PCN-99 as catalysis in hydroxylation of arylboronic acid.

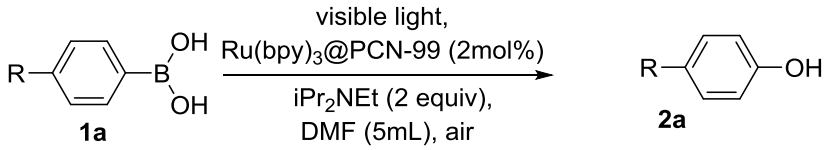

Entry	R-	Catalyst	1st Conversion	2nd Conversation
1	COOMe	$Ru(bpy)_3$@PCN-99	59.0%	60.0%
2	Me	$Ru(bpy)_3$@PCN-99	65.4%	65.0%
3	CHO	$Ru(bpy)_3$@PCN-99	45.9%	45.0%

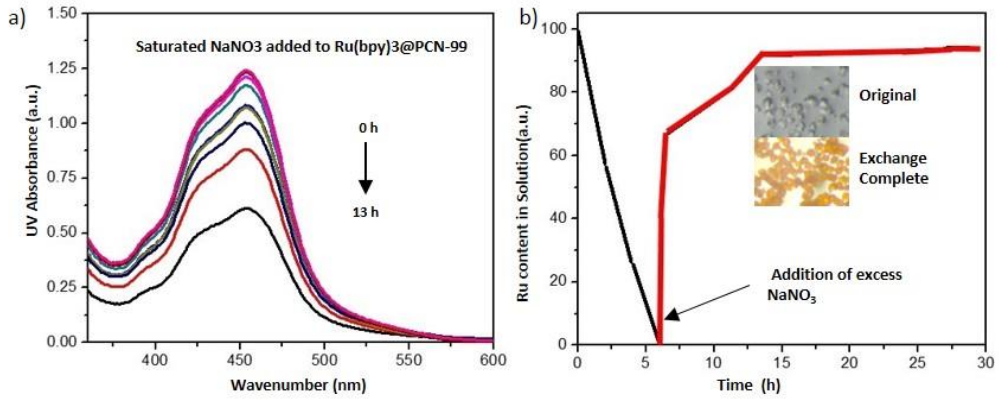

Figure II- 5. a) UV-Vis absorbance of $[Ru(bpy)3]^{2+}$ at different time after the addition of 20 mL of saturated $NaNO_3$ solution during the release experiment; b) trapping and releasing of $[Ru(bpy)3]^{2+}$ in PCN-99 in one-ion-change and release cycle.

2.4 Summary

In this study, a trigonal coplanar linker was designed using topology guidance to produce an anionic **bor**-MOF PCN-99. In light of its anionic nature, the selective encapsulation of $[Ru(bpy)_3]^{2+}$ through ion exchange imparts $Ru(bpy)_3$@PCN-99 with heterogeneous photocatalytic activity toward the aerobic hydroxylation of arylboronic acid. Not only does this work exemplify a successful approach to customize MOF structures to accommodate a bulky photocatalyst, it also provides insights into the construction of ionic MOFs with large cavities. The post-synthetic ion-exchange can be a technically straightforward alternative to the modification of other ionic MOFs with catalytic units—as such, it could be tested with other types of ionic MOFs and catalytic ions. The specific matrix PCN-99 in this work is also interesting for its luminescence properties, which may be useful for chemical sensing.

CHAPTER III

METAL DEPENDENT CATION EXCHANGE IN MAGNESIUM-BASED METAL-ORGANIC FRAMEWORKS

3.1 Introduction

Metal-organic frameworks (MOFs) are a family of porous materials consisting of multitopic organic linkers and metal-ion-containing nodes or secondary building units. The combination of these two building units produces 3D structures with unique chemical and physical properties, which are extremely useful for further applications in gas storage and separation, sensing, electronic conduction and catalysis. [132,135,136,246-250] Post-synthetic modification of MOFs, by altering the substituents of the organic linkers or changing the metal nodes, opens a field of new materials that cannot be reached by synthesis from scratch. [251-257] To tailor the composition of MOFs, especially the metal-containing nodes, post-synthetic cation exchange, or metathesis, demonstrates tremendous potential to furnish different properties from those of the parent MOFs. [132,134,136,137,139,140,253,257-263] In most cases, the metal substitution gets saturated (i.e. does not reach a complete exchange).[252,253,264] The details of cation exchange remain unknown. It has been proposed that several factors control the exchanging process: the coordination environment, electronegativity of pristine metal and incoming metal, flexibility of framework, and solvent among other possibilities. [142,154,155,157,252,258,264-266] However, systematic studies on the effects of incoming metal ions during the metathesis to address those influences are rare, which is extremely meaningful to adjust the physical properties and functionalities of the parent materials.

To date, there are less than 50 examples of post-synthetic metal metathesis (PSMM). [264,267] The common regard of the metal node, as an inert element for the framework, blinds insights to explore the basic principle for complete metal exchange. Only a few examples of complete metal change in MOFs happened, among which occur between Cu, Zn, Ni, and Co. [130,137,147,256,257,259,261,263,264,268-273] Moreover, the exchange time could range from a few days to even months. In this case, a complete metal exchange in MOFs in a practical time period remains elusive. With those difficulties, current metal exchange studies in MOFs is still dark in the box, especially for a complete metal exchange. A comprehensive and critical analysis of the knowledge of affecting factors and their influences has never been reported.

Taking advantage of the kinetically labile Mg–O bonds, a heterobimetallic network Mg/Cu-MOF, complete replacement of Mg ions with Co (II) and Ni (II) gave rise to the corresponding MOFs with maintained structural integrity and crystallinity, while the Cu (II) nodes were left unchanged. [140] Those studies demonstrated a clear advantage of the post-synthetic metathesis using Mg-MOFs as templates.

According to the literature, the Mg-containing nodes possess excellent compatibility when coordinating to various organic linkers in the construction of MOF.[274-281] The Mg secondary building units, existing as monomagnesium, dimagnesium, trimagnesium and infinite magnesium-oxygen chains, create great potential for gas storages in those Mg-MOFs. The commercial availability of magnesium salts and the mild condition necessary for synthesis both make Mg-MOFs accessible to scale up. As the applications of MOFs gain tremendous importance in material science,

more specific designs of materials encompassing compatible functionality in targeted applications are required. Therefore, it is important to gain insights on the influence of incoming metals in order to pursue the applicability in the cation exchange within MOFs. Herein, we present a systematic study on the cation exchange of Mg-MOF PCN-430 (PCN=Porous Coordination Network) with the first-row transition metals through post-synthetic metathesis and oxidation (PSMO) to identify the influences of factors, such as coordination modes, electronegativity differences, and solvent intervention, to the complete metathesis at room temperature.

3.2 Experimental Section

3.2.1 Materials and Instrumentation

Magnesium Nitrate Hexahydrate ($Mg(NO_3)_2 \cdot 6H_2O$), chromium(III) chloride ($CrCl_3$), chromium(II) chloride ($CrCl_2$), iron(III) chloride ($FeCl_3$), iron(II) chloride ($FeCl_2$), nickel chloride ($NiCl_2$), manganese bromide ($MnBr_2$), copper chloride ($CuCl_2$), zinc chloride ($ZnCl_2$), Vanadium Chloride (VCl_2), cobalt chloride ($CoCl_2$), Scandium Chloride ($ScCl_3$), Aluminum Chloride ($AlCl_3$), Titanium (III) Chloride tetrahydrofuran ($TiCl_3 \cdot 4THF$), N, N-dimethylformamide (DMF), dimethylacetamide (DMA), acetonitrile, and acetic acid were purchased from Alfa Aesar and Sigma-Aldrich. All commercial chemicals were used without further purification unless otherwise mentioned. The single-crystal data was collected on the Advanced Light Source Beamline 11.3.1 at the Lawrence Berkeley national Laboratory with a beam of monochromatic X-rays in the range of 6 - 17 keV. (0.73 - 2.0 Å). Powder X-ray

diffraction (PXRD) was carried out with a BRUKER D8-Focus Bragg-Brentano X-ray Powder Diffractometer equipped with a Cu sealed tube ($\lambda = 1.54178$) at 40 kV and 40 mA. NMR spectra were recorded on MERCURY 300 (1H 300 MHz). Energy dispersive X-ray spectroscopy was carried out by JEOL JSM-7500F with Oxford EDS system equipped with X-ray mapping. X-ray photoelectron spectroscopy was carried out by Kratos Axis Ultra Imaging X-ray photoelectron spectrometer. Inductively Coupled Plasma Emission - Mass Spectrometry (Laser Ablation) was carried out by Perkin Elmer DRCII ICP-MS with both solution and laser ablation capabilities. All the ICP-MS certified reference standards are purchased from RICCA Chemical Company.

3.2.2 Ligand Synthesis

The ligand H_3TATB was synthesized through reported literatures. [282-284]

3.2.3 MOF Synthesis

Synthesis of PCN-430-Mg

A typical synthesis involved magnesium nitrate hexahydrate $Mg(NO_3)_2.6H_2O$ (30 mg, 0.2023 mmol) H_3TATB (10 mg, 0.0226 mmol) in 2 mL N, N'-dimethylacetamide (DMA) and one drop of 1 M HOAc. The mixture was then introduced into a 4 mL Pyrex vial which was heated at 120 ^oC for overnight. After cooling down, the solution was filtered and washed with DMF, yielding colorless crystals.

3.2.4 General Procedure for Metal Exchange

Exchange with Divalent Metals (Mn, Co, Ni, Cu, Zn)

As-synthesized Mg and Co MOFs 25mg was washed with dry DMF several times. About 100 mg MCl_2 or MBr_2 (M=Mn, Co, Ni, Cu, Zn) was added and gently stirred for 12 hrs. Then the solution was decanted, and free dry DMF was added. Another 50 mg of MCl_2 or MBr_2 was added for complete exchange under stirring for 12 hrs. The final products were achieved after washing with fresh dry DMF several times.

Exchange with Trivalent Metals (Sc, Al, Ti, Fe, Cr) and Air-sensitive Metal (V^{2+}, Cr^{2+} and Fe^{2+})

As-synthesized PCN-430-Mg 25mg was washed with dry DMF several times and then immersed in 3 mL dry DMF. The mixture was later bubbled with nitrogen for 15 min, followed by 100 mg MCl_x (0.16 mol/L, M=Sc, Al, Ti, x=3; M=V, Fe, Cr, x=2) was added under the protection of nitrogen. Another two or three portions of MCl_x was added to the reaction in order to maximize the exchange, after the old solution was removed by syringe and new dry DMF was added under nitrogen. The solid was washed with fresh dry DMF to get the final product. In the case of V(II), Cr (II), Fe(II), and Ti(III), the sample was further bubbled with air for 15 min to get the corresponding derivatives, respectively. The final products were achieved by washing the mixture with large amount of DMF until the solution became colorless.

3.2.5 X-ray Photoelectron Spectroscopy (XPS) and Energy Dispersive X-ray Spectroscopy (EDS) Analysis

In order to confirm the oxidation state of products, we preformed XPS measurement for PCN-426-X (II/III) and PCN-430-X(II/III). We also performed EDS analysis to find the exchange extent of those MOFs. In both cases, ~10mg of different MOF samples were prepared and washed a large amount of DMF, then a large amount of acetone, and finally dried in the oven before tests.

3.2.6 ICP-MS Sample Preparation

All the samples were washed with DMF continuously until clear solution were created. After samples were washed with acetone and dried in an oven. All the MOF samples were prepared in triplicate with weights of 2-3mg of sample. Each sample was dissolved in 1mL of J.T. Baker Ultrex® II Ultrapure 70% nitric acid at 60^{o}C for 12 hours. Samples were then diluted to 750x in 1% nitric acid and 18.0 MΩ water from Millipore Milli-Q® water purification system. Calibration standards were prepared from certified reference standards from the RICCA Chemical Company. Samples were further analyzed with a Perkin Elmer NexION® 300D ICP-MS. Resulting calibration curves have a minimum R^2=0.9999. Additionally, in order to maintain accuracy, quality control samples from certified reference standards and internal standards were utilized. The individual results of the triplicate samples were averaged to determine the metal ratios as the final results.

3.3 Results and Discussion

3.3.1 Characterization of Crystal Structures

The Crystal Structure of PCN-430

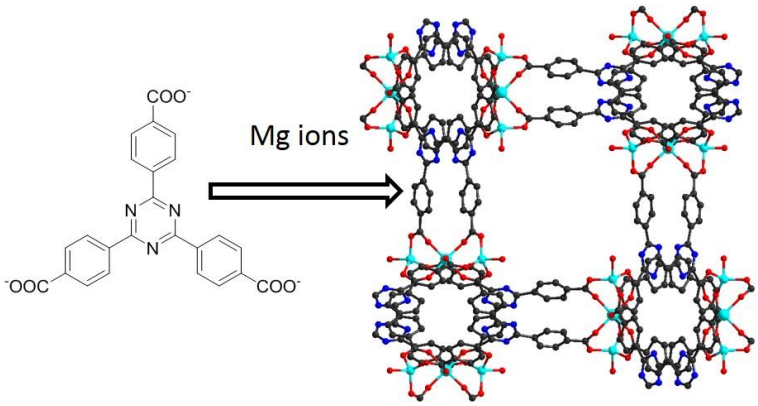

Figure III- 1. Structure of PCN-430-Mg, synthesized from TATB ligands and Mg(II) ions.

Several groups have previously reported a series of MOFs composing linker 4,4',4''-s-trizaine-2,4,6-triyl-tricarboxylate (TATB). [282-295] The relative availability and richness of topologies of TATB-containing MOFs make it a good linker support of the MOF template. The combination of Mg and TATB yields a novel structure of PCN-430-Mg. Due to the lability of PCN-430-Mg, it was difficult to characterize the structure by single crystal X-ray diffractometer. Instead, we were able to collect the data of PCN-430-Mg/Co with the help of synchrotron. PCN-430-Mg only adopts one hourglass-type of secondary building units with two terminal solvent molecules, where three

magnesium cations bridged and ligates by six carboxylates from the TATB linkers through oxygen (Figure III-1). The middle Mg ion has an octahedral coordination environment, while the other two Mg cations are 4-connected with terminal solvent molecules. There are numbers of examples in the literature in which metal ions are arranged in such an hourglass configuration. [42,282,284,296]

3.3.2 Direct Metathesis with Trivalent Metal

Direct Metathesis of PCN-430-Mg with Trivalent Metals

To examine the effects of trivalent incoming metals in the exchange into PCN-430-Mg, we soaked the single crystals of PCN-430-Mg of in a concentrated DMF solution of trivalent metals salts ($ScCl_3 \cdot 6H_2O$, $CrCl_3 \cdot 6H_2O$, VCl_3, and $FeCl_3$) under otherwise identical conditions. In the exchange to Sc(III), the colorless crystals rapidly turned to white (Figure III-2), indicating the favored coordination between TATB and Sc ions. In the system of PCN-426, we demonstrated that the comparisons of the water exchange rates of incoming metals could be used to gauge the relative reactivity of two metal ions in postsynthetic metathesis regardless of the nature of ligands.[139] Since the water exchange rates constant is only metal-dependent, it is easy to research the literature for the value comparisons. For Sc (III), the exchange rate constant is $4.8\times10^7 s^{-1}$, which is much higher than that of Mg(II) $6.7\times10^5 s^{-1}$. Considering about the stronger coordination between Sc-O and faster ligand exchange rate, majority replacement of Mg to Sc is reasonable (Figure III-3). Beside of Sc(III), all the other trivalent metals have a much small ligand exchange rate, which is a sign of slower exchange.

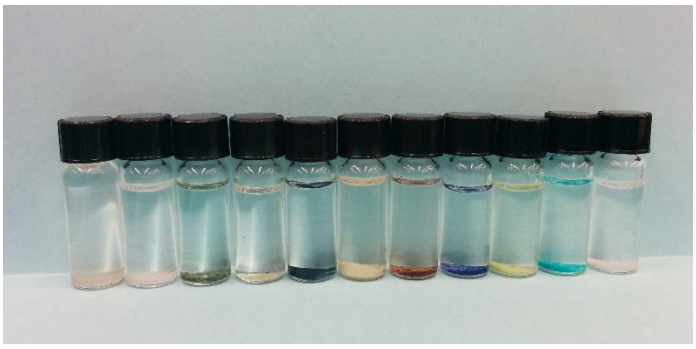

Figure III- 2. PCN-430-M Crystal after metal exchange. (M=Mg, Sc, V, Ti, Cr, Mn, Fe, Co, Ni, Cu, Zn from left to right).

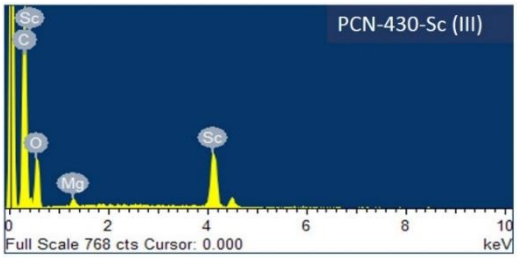

PCN-430-Sc/Mg	ICP-MS			SEM-EDS		
Mg	1.00	1.47	0.84	0.36	0.22	0.23
Sc	18.88	35.92	21.44	3.09	4.33	3.54
Sc%	94.96	96.06	96.23	93.35	94.96	94.40
Average Sc%	95.75			94.24		

Figure III- 3. EDS and ICP-MS results of PCN-430-Sc.

The exchange process with air-sensitive Ti(III) were performed under inert environment, after which PCN-430-Mg/Ti were further oxidized by air. About half of the Mg ions were replaced by Ti according to the ICP-MS and EDX results (Table III-1 Entry 2, Figure III-4). Due to the poor solubility of $CrCl_3$ in DMF, the hydrated $CrCl_3 \cdot 6H_2O$ were used. As a result, the Lewis acidic Cr (III) rapidly destroyed the labile

Mg−O bonds, and eventually the frameworks decomposed. Similar decomposition was also observed in the cased of V(III) (Table III-1 Entry 3). Following a direct metathesis of PCN-430-Mg with $FeCl_3$, only a slight color change occurred (Table III-1 Entry 6, Figure III-5). PCN-430-M(III) (M=Ti and Fe) were amorphous, which could be ascribed that the hourglass type metal unites are not favored by those trivalent metals. Instead of the hourglass metal units, the classic μ_3-oxotrimetal were observed previously when Sc, Cr, and Fe coordinated to TATB linkers.[135,295] At the sample time, there are rare examples reported literature on trititanium unites. As the early stage of cation exchange involved in the dissociation of Mg−O bonds and the formation of M-O (M as the incoming metal) bonds, the strong Lewis acids (trivalent metals here) quickly destroys the Mg−O bonds, theoretically accelerating the exchange process. When this dissociation of Mg−O bonds is much larger than the formation of M-O bonds, the framework would decompose. Moreover, the small ligand exchange rates of those trivalent metals slow down the entire exchange process and eventually lead to partial exchange. As the cation exchange goes on, the trivalent metals attempt to form their thermodynamic-preferred configuration, while the retained Mg-MOF maintained its original configuration. Therefore, the mixture of those configurations make the final product amorphous.

Table III- 1. Summary of Exchanged PCN-430.

Entry	Metal	Charge	ICP	SEM-EDX	Crystallinity after Exchange	Ligand-Exchange Rate (s^{-1} @298K) [a]	Reported SBUs[b]	Ref.
	Mg	+2	–	–	Yes	6.7×10^{5}	hourglass	This work
1	Sc	+3	95.75%	94.24%	No	4.8×10^{7}[c]	μ_3-oxotrimetal	295
2	Ti	+3[d]	44.21%	47.73%	No	1.8×10^{-2}	–	–
3	V	+2[d]	26.61%	28.57%	Yes	–	–	–
		+3	Decomposed	Decomposed	–	5.0×10^{-2}		
4	Cr	+2[d]	73.79%	77.39%	Yes	$\sim10^{9}$	–	–
		+3	Decomposed	Decomposed	–	2.4×10^{-6}	μ_3-oxotrimetal	135
5	Mn	+2	97.91%	100%	yes		Hourglass	284
							chain	291
6	Fe	+2[d]	77.38%	81.32%	Yes	4.4×10^{6}	–	–
		+3	99.86%	99.92%	No	1.6×10^{2}	μ_3-oxotrimetal	295
7	Co	+2	65.41%	72.62%	Yes		hourglass $Co_4(\mu_4\text{-}O)$	282,284 285
8	Ni	+2	70.66% [e]	73.63% [e]	Yes		μ_3-oxotrimetal	297
9	Cu	+2	98.80%	~100%	Yes[f]		paddle wheel	35
10	Zn	+2	64.57%	69.95%	Yes		Hourglass $Zn_6(\mu_4\text{-}O)$	284,288,293 291

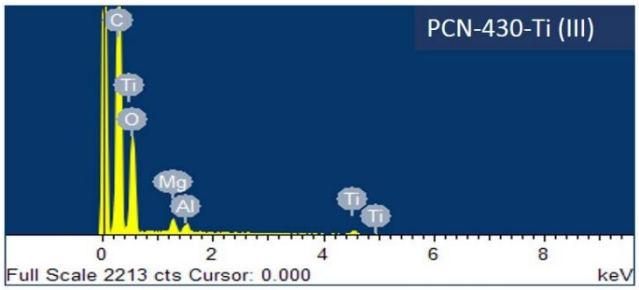

PCN-430-Ti/Mg	ICP-MS			SEM-EDS		
Mg	0.27	0.18	0.20	0.85	0.24	1.01
Ti	0.25	0.26	0.15	0.92	0.13	1.29
Ti%	48.16	58.88	42.67	51.98	35.14	56.09
Average Ti%	44.21			47.73		

Figure III- 4. EDS and ICP-MS results of PCN-430-Ti.

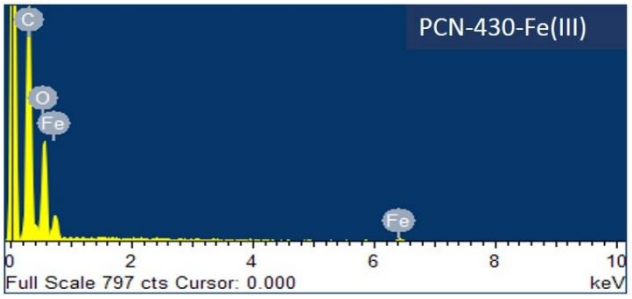

PCN-430-Fe/Mg	ICP-MS			SEM-EDS		
Mg	0.04	0.02	0.01	0.00	0.08	0.00
Fe	16.63	12.26	14.52	25.06	25.18	24.36
Fe%	99.78	99.88	99.92	100	99.68	100
Average Fe%	99.86			99.89		

Figure III- 5. EDS and ICP-MS results of PCN-430-Fe(III).

3.3.2 Metathesis of PCN-430-Mg with Redox Active Transition Metals (M^{II}/M^{III}).

Introduction of metastable PCN-426-Cr(II) and PCN-426-Fe(II) were the key to drive the exchange of Mg-PCN-426 to completion. In a similar manner, utilization the

relative lability differences of Fe(III)-O bond Cr(II)-O bond in PCN-333, complete substitution of Fe(III) to Cr(II) was achieved. [135] All of these cases tells that the redox active metals have great potential in serving as the metastable intermediates, which accelerate the cation exchange while preserve the integrity of the framework. Taking notes from this unique metastable intermediates, we were able to investigate the cation exchange of those redox active species in our PCN-430 system. Due to the air sensitivity of the M(II)(M=V, Cr, Fe) species, all the cation exchange were performed in the inert environment. Air oxidation was followed with those M(II)-PCN-430 species to obtain the final products.

The solubility of anhydrous VCl_2 in DMF was so low that only very small amount of Mg ions (~26.61% based on ICP-MS while ~28.57 % based on EDX) were replaced by V(II) ions (Table III-1 Entry 3, Figure III-6) . At the same time, two thirds of Mg had been substituted in both Cr(II) and Fe(II) species (Table III-1 Entry 4 and 6). As mentioned before both of Cr(II) and Fe(II) species have a larger ligand exchange rate constant (10^6 and 10^{10} k, sec^{-1}, respectively), which would ideally promote the exchange process. However, none of the cation exchange went to completion. The partial exchange might be attributed to the coordination of magnesium. Studies has revealed that the coordination number of parent metal increased during the cation exchange. [157] In this case, the center six-coordinated Mg ion is too full to support the additional coordination. As the result, the centered Mg ion would be most likely retained, while the four-coordinated Mg would be easily replaced. Therefore, about two thirds of substitution of Cr and Fe in PCN-430 was reasonable (Figure III-7 and Figure III-8).

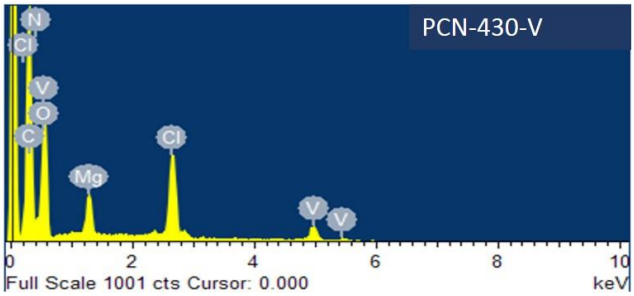

PCN-430-V/Mg	ICP-MS			SEM-EDS		
Mg	4.22	3.72	4.22	1.95	2.80	2.70
V	1.61	1.31	1.50	1.06	0.85	1.01
V%	27.60	26.06	26.18	35.22	23.29	27.22
Average V%	26.61			28.57		

Figure III- 6. EDS and ICP-MS results of PCN-430-V.

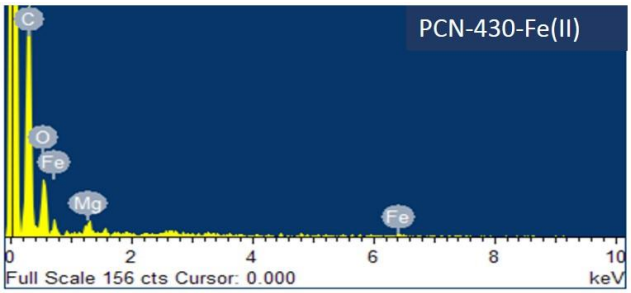

PCN-430-Fe/Mg	ICP-MS			SEM-EDS		
Mg	5.64	15.37	7.54	0.87	1.20	1.22
Fe	23.32	40.92	28.25	4.56	4.63	5.06
Fe%	80.52	72.70	78.92	83.98	79.42	80.57
Average Fe%	77.38			81.32		

Figure III- 7. EDS and ICP-MS results of PCN-430-Fe with $FeCl_2$.

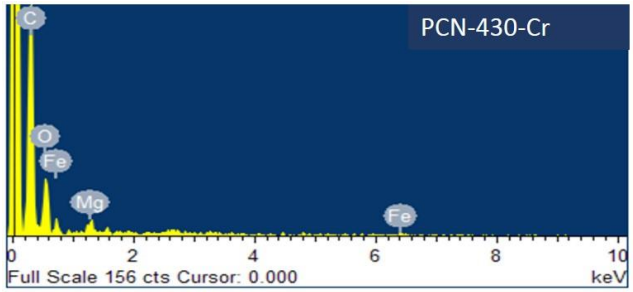

PCN-430-Cr/Mg	ICP-MS			SEM-EDS		
Mg	4.36	10.69	8.83	1.17	1.00	1.35
Cr	15.04	27.62	22.45	3.83	4.17	4.03
Cr%	77.51	72.10	71.77	76.60	80.66	74.91
Average Cr%	73.79			77.39		

Figure III- 8. EDS and ICP-MS results of PCN-430-Cr with $CrCl_2$.

3.3.3 Metathesis with Divalent Transition Metals

Direct Metathesis of PCN-430-Mg with Divalent Transition Metals

Direct metathesis of PCN-430-Mg with $Mn(NO_3)_2$ at room temperature quickly destroyed the liable Mg−O bonds. If we again use the water exchange constant as the reference again, we see the constant for Mn^{2+} is 10^7 *k, sec*$^{-1}$(vs Mg 10^5 *k, sec*$^{-1}$*).*[298] Therefore, the incoming mental salts were switched to $MnBr_2$, which is less ease to ionize Mn^{2+}. As expected, the exchange with $MnBr_2$ completed based on the SEM-EDX and ICP-MS results (Figure III-9).

Only about two thirds of the Mg ions were replaced during the direct metathesis of PCN-430-Mg with Co^{2+} ions and Zn^{2+} (Figure III-10 and Figure III-11, respectively). Even both those two metals have been previously reported with an hourglass SBU, [282,284,288,293]the nature of free Co^{2+} (d^7, high spin) and Zn^{2+} (d^{10}, preference for a

tetrahedral coordination environment) ions in solution made the exchange less thermodynamically favorable.

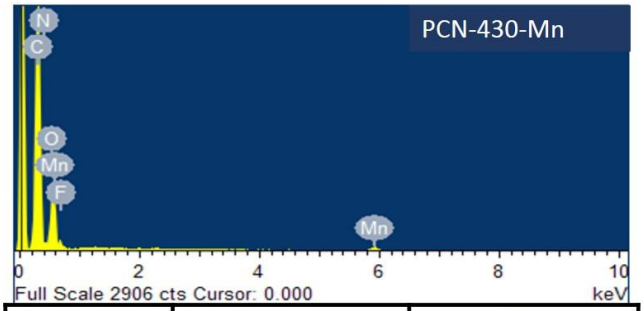

PCN-430-Mn	ICP-MS			SEM-EDS		
Mg	0.54	0.42	0.32	0	0	0
Mn	26.16	17.97	15.95	5.30	4.41	4.21
Mn%	97.98	97.73	98.03	100	100	100
Average Mn%	97.91			100		

Figure III- 9. EDS and ICP-MS results of PCN-430-Mn.

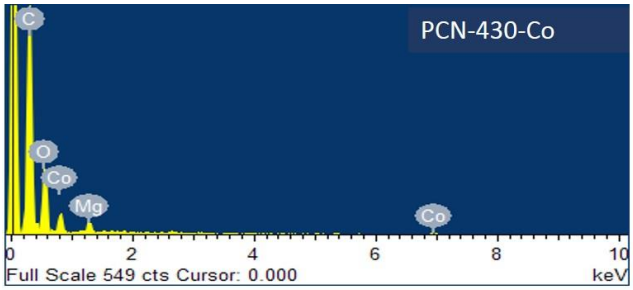

PCN-430-Co/Mg	ICP-MS			SEM-EDS		
Mg	9.29	5.64	6.17	1.53	1.17	1.40
Co	17.37	11.65	10.82	3.49	3.58	3.78
Co%	65.15	67.38	63.71	69.52	75.37	72.97
Average Co%	65.41			72.62		

Figure III- 10. EDS and ICP-MS results of PCN-430-Co.

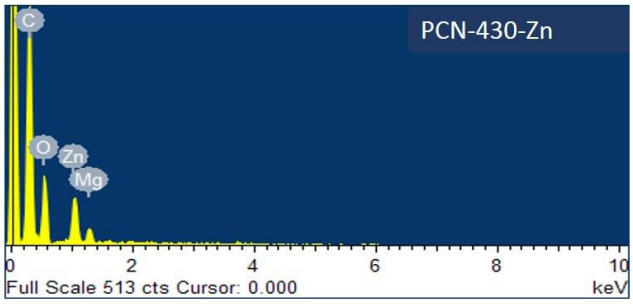

PCN-430-Zn/Mg	ICP-MS			SEM-EDS		
Mg	8.92	12.37	4.35	1.38	1.10	1.30
Zn	16.29	22.50	7.91	3.06	3.09	2.66
Zn%	64.63	64.54	64.53	68.92	73.75	67.17
Average Zn%	64.57			69.95		

Figure III- 11. EDS and ICP-MS results of PCN-430-Zn.

Similar results were found in the exchange with $Ni(NO_3)_2$ (Figure III-12). One of the reasons behind the partial exchange with Ni^{2+} could be the geometrical preference, where the preferred coordination between Ni and TATB have been reported in a SBU of μ_3-oxotrimetal of PCN-5.[297] Another reason could be the smaller water exchange constant (10^4 *k, sec*$^{-1}$) compare to that of Mg^{2+} ion. Previous study reveals that basic solvents (for example, DMF) provide stronger associate with the metal ions, leading to stable adducts and retarding the rate of cation exchange. [154] For the curiosity of the solvent basicity influence in our system of PCN-430, we performed the same exchange experiments in the mixed solvent systems under the same synthetic conditions. As the volumetric ratio of between MeCN and DMF increase to 1:1 or even 2:1, complete exchange to Ni^{2+} ions were observed at the expense of crystallinity.

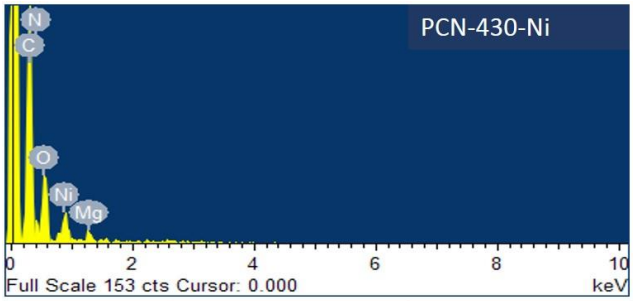

PCN-430-Ni/Mg	ICP-MS			SEM-EDS		
Mg	6.60	5.87	6.32	1.55	1.65	1.65
Ni	15.79	14.13	15.33	4.52	5.19	3.95
Ni%	70.53	70.65	70.81	74.46	75.88	70.54
Average Ni%	70.66			73.63		

Figure III- 12. EDS and ICP-MS results of PCN-430-Ni.

Since PCN-6-Cu has been previously reported contained a dicopper paddle wheel SBU[286], the cation exchange of PCN-430-Mg with Cu^{2+} ion would expectably result in a partial exchange, which might be similar to the case of Cr^{2+} with a geometrical preference of the μ_3-oxotrimetal SBUs. To our surprise, almost complete exchange were achieved (Figure III-13). Instead of a similar power pattern to PCN-430-Mg, a completely different powder pattern was observed, which matched well with that of PCN-6-Cu. Once we compare the water exchange rate constant of Cu^{2+} (10^9 *k*, sec^{-1}), it is almost four magnitude faster than that of Mg^{2+} (10^5 *k*, sec^{-1}). The rapid exchange rate will likely give rise to a faster linker-metal bond formation than the bond dissociation. Moreover, the stable Cu-O in a dicopper paddle wheel is thermodynamically favored. Under those cooperative influence, a complex similar to PCN-6-Cu was eventually produced.

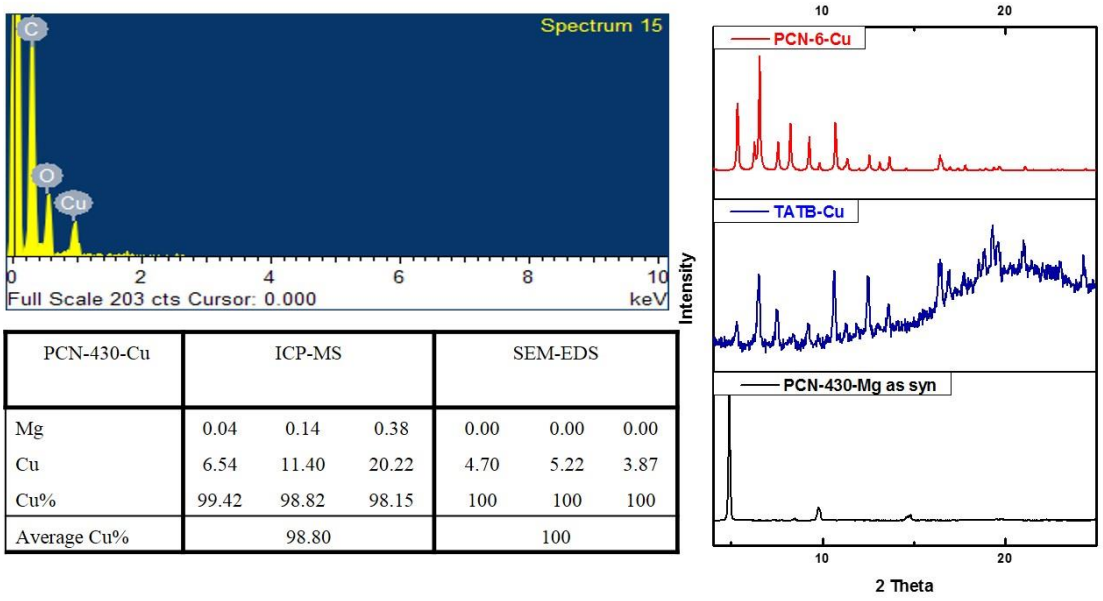

PCN-430-Cu	ICP-MS			SEM-EDS		
Mg	0.04	0.14	0.38	0.00	0.00	0.00
Cu	6.54	11.40	20.22	4.70	5.22	3.87
Cu%	99.42	98.82	98.15	100	100	100
Average Cu%	98.80			100		

Figure III- 13. EDS, ICP-MS and PXRD results of PCN-430-Cu.

3.3.4 Gas Sorption Study of PCN-430-Fe(III)

Due to the liability of Mg–O, the parent MOF PCN-430-Mg collapsed during the activation. Moreover, PCN-430-Mn also collapsed at the same time. With the increasing stability of the coordination between metal and oxygen (Fe>V>Co>Mg), an enhancement of surface area is displayed. This improvement of porosity approves that post-synthetic metathesis and oxidation is such an excellent method to enhance the physical properties of MOFs.

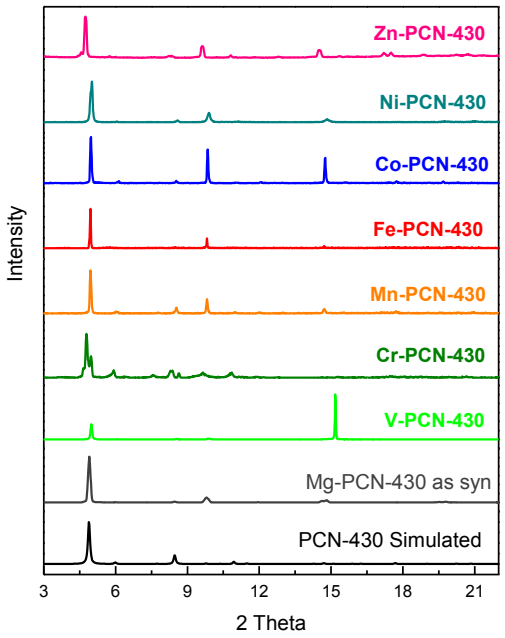

Figure III- 14. PXRD patterns of PCN-430-X.

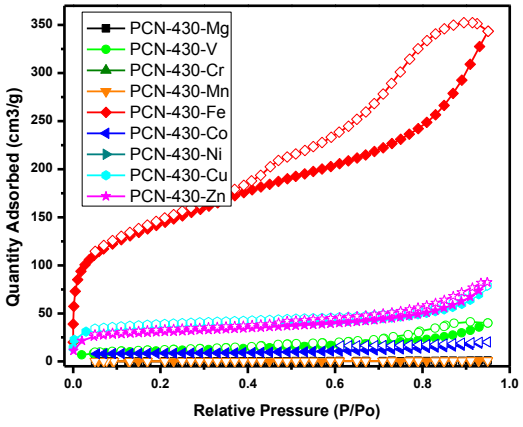

Figure III- 15. Selective nitrogen adsorption isotherms of PCN-430-X.

3.4 Summary

PCN-430-Mg with the labile Mg−O bonds was chosen as a template to ease the following metal exchange. In the project, the method of post-synthetic metathesis and oxidation, where the MOF template was first exchanged with low-oxidation-state but kinetically labile metal ions and subsequently oxidized to high oxidation state, was applied to accelerate the metal-exchange for redox-active exchanging metals. The study of cation exchange of parent MOF PCN-430-Mg with the first row transition metal indicate several important criteria for complete post-synthetic metal metathesis at room temperature. First, the parent framework much be constructed from relative labile metal-linker bonds compare to that of the target framework, evidenced by a large water ligand exchange rate. Only if the entering metal-linker is thermodynamically stable, in another words a slow water ligand exchange rate of the entering metal, the equilibrium could be driven to the side of target framework. Last but not most, complete cation exchange will likely occur when the geometrically preference of those metal-containing SBUs of incoming metal ions match with those of parent MOFs.

Besides of the mentioned liability of the parent MOFs, stability of target MOFs, and geometric preference between those two MOFs, there are many other factors affecting the exchange process. More symmetric study are needed to further understand the exchange mechanism. We expect those knowledge of post-synthetic metathesis will give some guidance to the later studies for specific applications.

CHAPTER IV

NITROGEN-RICH PORPHYRINIC METAL-ORGANIC FRAMEWORKS SYNTHESIZED BY POSTSYNTHETIC METATHESIS FOR CATALYSIS*

4.1 Introduction

Metal-organic frameworks (MOFs), as a new class of organic-inorganic hybrid porous materials,[7,299] have attracted considerable attention due to their versatile potential applications in various areas, such as gas storage/separation,[300-305] chemical sensing,[306] luminescence,[307] and drug delivery.[245,308,309] The ability to impart specific functional linkers and clusters in the framework while allowing the access of substrates to the active center in the highly porous structure makes these compounds very attractive for catalysis.[310,311] Theoretically, reactant molecules will be adsorbed and pre-concentrated, thereby boosting catalytic reaction rates. Metalloporphyrins, a classical example of N_4 macrocyclic compounds, are known for their catalytic activities in active centers of enzymes such as Cytochrome P450.[312] These prototypal catalytic properties have spurred extensive studies on the construction of MOFs based on the building blocks of metalloporphyrins.[313-315] Representative examples include the synthesis of light-harvesting MOFs,[316-319] and biomimetic porphyrinic MOFs.[320,321] The majority of porphyrinic MOFs are constructed from carboxylate linkers.[249,313,320] By contrast,

* Reproduced with permission from "Nitrogen-rich porphyrinic metal-organic frameworks synthesized by postsynthetic metathesis: from inert material to active catalyst" by Liu, D.; Wang, X.; Chen, Y.-P.; Yuan, S., Zhong, C.; Zhou, H.-C., *Sic. China. Chem.* (2016). doi:10.1007/ss11426-016-0060-3, copyright 2016 by Springer Berlin Heidelberg.

porphyrinic MOFs structurally linked through nitrogen coordination is relatively underdeveloped.

Compared to the coordination of transition metals with carboxylates, the nitrogen-rich linkers show that active sites can be rationally introduced into the framework through active uncoordinated N-heteroatoms to demonstrate their functions.[322-324] In addition, nitrogen-rich linkers usually exhibit their highest occupied molecular orbitals (HOMOs) at a relatively high energy level.[322,323] The interactions between these linkers and the soft Lewis acidic transition metals will likely result in the stronger orbital overlapping and afford a relatively stable M-L bond.[325] Experimentally, MOFs constructed with pyrazolates and triazolates have demonstrated excellent chemical stability. [319,322,323] However, the stronger coordination bonds between linkers and metal nodes commonly are linked with slow bond dissociation, which makes those MOFs challenging to be obtained as crystalline products, especially single crystals. On the other hand, MOFs based on tetrazolate linkers are easier to obtain in the form of single crystals, extensively facilitating structural characterization. In general, tetrazolate has much smaller pK_a value and could adopt similar coordinating modes as the triazolate and pyrazolate.[322,323] Thus, isoreticular structures of pyrazolate- and triazolate-based MOFs can be conveniently simulated and identified based on the tetrazolate-based models.[324] With those aforementioned concerns, a porphyrinic MOF using a tetrazolate linker, 5,10,15,20-tetrakis[4-(2H-tetrazol-5-yl)phenyl] porphyrin (H_2TTPP) was designed and synthesized.

4.2 Experimental Section

4.2.1 Materials and Instrumentation

Materials

Pyrrole, propionic acid, *N*,*N*'-diethylformamide (DEF), cadmium chloride ($CdCl_2$), methanol, 4-formyl benzonitrile, ethyl acetate, tetrahydrofuran, ammonia chloride (NH_4Cl), sodium azide (NaN_3), and dichloromethane (CH_2Cl_2) were purchased from Alfa Aesar. All commercial chemicals were used without further purification.

Instrumentation

Single crystal X-ray data were collected on a Bruker Smart Apex diffractometer equipped with a fine-focus sealed-tube X-ray source (Mo-Kα radiation, λ = 0.71073 Å, graphite monochromated) and a low temperature device. Powder X-ray diffraction (PXRD) was performed on a Bruker D8-Focus Bragg-Brentano X-ray Powder Diffractometer equipped with a Cu sealed tube (λ = 1.54178 Å) at 40 kV and 40 mA. ICP-MS experiment was performed on a Perkin Elmer NexION® 300D ICP-MS with sample digested in J.T. Baker Ultrex® II Ultrapure 70% nitric acid at 70ºC for 12 hours in triplicate. Nuclear magnetic resonance (NMR) data were collected on a Mercury 300 spectrometer. Energy dispersive X-ray spectroscopy was measured using Quanta 600 FEG with Oxford EDS system equipped with X-ray mapping.

4.2.2 Ligand Synthesis

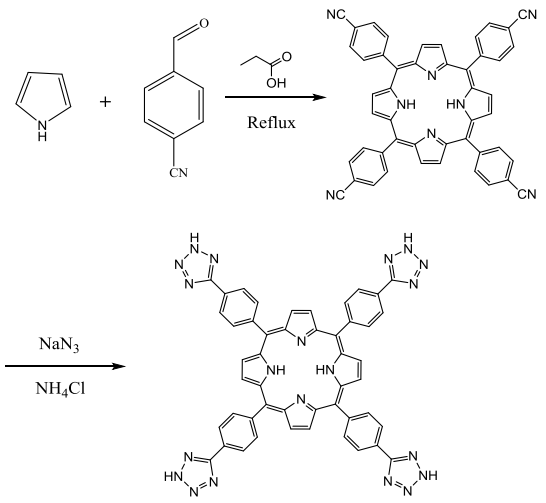

Scheme IV- 1. Synthesis of 5,10,15,20-tetrakis[4-(2H-tetrazol-5-yl)phenyl]porphyrin.

5,10,15,20-tetrakis[4-(2H-tetrazol-5-yl)phenyl]porphyrin (H_2TTPP) ligand was prepared using the modified method according to the literature.[326,327] 4-formyl benzonitrile (1.13 g, 8.46 mmol), pyrrole (0.6 ml, 8.46 mmol) and propionic acid (20 ml) were added to the flask equipped with a reflux condenser and heated to reflux for overnight. Then, the reaction mixture was washed several times using methanol, ethyl acetate, and tetrahydrofuran, followed by dry in vacuum to obtain 5,10,15,20-tetraki(4-cyanophenyl)porphyrin (0.35 g) in 23 % yield as a violet solid. ^{1}H NMR ($CDCl_3$) δ 8.83 (s, 8H), 8.35 (d, 8H), 8.10 (d, 8H).

A solution of 5,10,15,20-tetraki(4-cyanophenyl)porphyrin (0.30 g, 0.42 mmol), NaN_3 (0.24 g, 3.67 mmol), NH_4Cl (0.18 g, 3.37 mmol), and DMF (25 ml) was heated at

120 °C for 3 days. In order to guarantee the completion of reaction, additional NaN_3 (0.17 g, 2.59 mmol) and NH_4Cl (0.11 g, 2.05 mmol) were added to the mixture. After the evaporation of DMF under reduced pressure, cold water (10 ml), 6 N HCl and CH_2Cl_2 (10 ml) were added in sequence. The precipitate was filtered and dried in vacuum to obtain 5,10,15,20-tetrakis[4-(2H-tetrazol-5-yl)phenyl]porphyrin (0.35 g) in 94 % yield as a green solid. ^{1}H NMR (DMSO-d_6) δ 8.96 (s, 8H), 8.51 (m, 16H).

4.2.3 Synthesis of PCN-527-Cd

PCN-527-Cd was prepared according to our previous report.[328] Solvothermal reaction of $CdCl_2 \cdot 2H_2O$ (30 mg) and H_2TTPP (8 mg) in the mixture of DEF (2.5 mL) and methanol (0.9 mL) at 65 ^{o}C gave rise to dark purple cuboid crystals.

4.2.4 Preparation of PCN-527-Fe

PCN-527-Fe was prepared using metal exchange procedure. 30 mg as-synthesized PCN-527-Cd was washed with dry DMF for several times. The mixture was bubbled using nitrogen for about 20 min, followed by the addition of $FeCl_2$ (~50mg) under the nitrogen protection. The mixture was properly sealed and protected under nitrogen. To make exchange process completely, the mixture was heated to 85 °C for about 4 hrs. Then the $FeCl_2$ solution was removed carefully, and the mixture was further bubbled with air to ensure all Fe^{3+}. The final solid was washed with fresh dry DMF to get PCN-527-Fe.

4.2.5 Structure Determination of Single Crystals

Single-crystal X-ray data frames of PCN-527 were collected using the program APEX 2 and processed using the program *SAINT* routine within *APEX 2*. The data were corrected for absorption and beam corrections based on the multiscan technique as implemented in *SADABS.* The structure was solved by direct methods and refined by full-matrix least-squares on F^2 with anisotropic displacement using the *SHELXTL* software package. Non-hydrogen atoms were refined with anisotropic displacement parameters during the final cycles. Hydrogen atoms on carbon and nitrogen were calculated in ideal positions with isotropic displacement parameters set to $1.2 \times U_{eq}$ of the attached atoms, but hydroxide hydrogen atoms were not added into the structure. Contributions to scattering due to these solvent molecules were removed using the *SQUEEZE* routine of *PLATON*, and the structures were then refined again using the data generated. The contents of the solvent region are not represented in the unit cell contents in the crystal data. Detailed crystallographic data and structural refinements for PCN-527-Cd and PCN-527-Fe are given in this literature. [328]

4.2.6 Procedure of Catalysis

Dimethoxymethylbenzene (0.30 g, 2.0 mmol) or 4-bromobenzaldehyhde diethyl acetal (0.52 g, 2.0 mmol) and malononitrile (0.14 g, 2.1 mmol) were stirred in DMSO-d_6 solution for 15 min. Then PCN-527 (0.01 mmol, 28 mg for PCN-527-Cd, 24 mg for PCN-527-Fe) was added and stirred at 50 °C for 12 h. The reaction progress was directly

monitored by ^{1}H NMR. The yields and conversion ratios were calculated by the integration of benzylic protons at the end of reaction.

4.2.7 Control Experiment

~15 mg H_2TTPP and 50 mg $FeCl_2$ was mixed in 2mL DMF and heated to 85 °C for about 4 hrs under nitrogen before the $FeCl_2$ solution was removed carefully. Large amount of water was added to precipitate out the H_2TTPP(Fe) ligand, and the ligand was filtered, washed with 2M HCl solution, water to pH neutral, and finally dried under vacuum to yield H_2TTPP(Fe).

Dimethoxymethylbenzene (0.30 g, 2.0 mmol) and malononitrile (0.14 g, 2.1 mmol) were stirred in DMSO-d_6 solution for 15 min. Then H_2TTPP (8.8mg, 0.01 mmol) mg , or H_2TTPP(Fe) (~15mg) was added and stirred at 50 °C for 12 h, respectively. The reaction progress was directly monitored by ^{1}H NMR and ^{13}C NMR.

4.3 Results and Discussion

4.3.1 Characterization of Crystal Structures

Single-crystal X-ray analysis at room temperature revealed that PCN-527-Cd crystalized in the tetragonal *P4/mmm* space group with $a = b = 27.809$Å, $c = 20.600$ Å (More single crystal information was included in SI†, CCDC 1063032), which is isoreticular to PCN-526[328] and UTSA-57[329]. The framework adopts a 3D 4,8-connected **scu** topology consisting of square-planar and cubic nodes (Figure. 1).[238,330-333] As shown in Figure. 2, the chloride-centered $[Cd_4Cl]^{7+}$ clusters are linked by square planar TTPP

linkers to form a 3D structure with 1D channels as large as 20 Å along *c* direction. Each Cd in the square cluster adopts octahedral coordination geometry with four nitrogen atoms from tetrazolate rings and chloride in the axial positions. In addition, every pair of the uncoordinated nitrogen atoms in adjacent tetrazolate rings on different TTPP linkers bridge a partially occupied (~ 25 %) Cd(II) ions along the edges of the square cluster, and the remaining coordination positions are occupied by water molecules and chloride atoms. The partially occupied Cd(II) can be treated as extra-framework metal sites, which were also found in a reported (3,8)-connected Mn-MOF. [64]

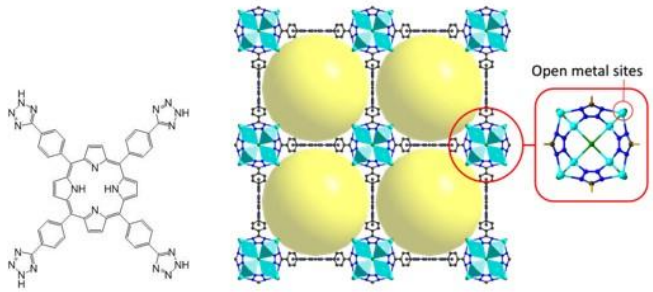

Figure IV-1. 5,10,15,20-tetrakis[4-(2H-tetrazol-5-yl) phenyl]porphyrin (TTPP) ligand. (left) Structure of PCN-527-Cd and chloride-centered $[Cd_4Cl]^{7+}$ clusters (Cd atoms are shown in cyan, N atoms in blue, Cl atoms in green, and C atoms in gray; yellow sphere indicates the channel, right).

4.3.2 Catalysis of One-pot deacetalization-Knoevenagel Condensation Reaction by PCN-527-Cd

Metal sites in the clusters as well as the center of the porphyrin can serve as weak Lewis acidic centers, and the uncoordinated nitrogen atoms in the tetrazolate rings can

act as Lewis basic sites. Such functionality endows PCN-527 a promising candidate for one-pot catalysis reactions. Therefore, we employed PCN-527-Cd as a heterogeneous catalyst for the deacetalization-Knoevenagel condensation reaction.[334-338] The first step is the acid-catalyzed deacetalization of dimethoxymethylbenzene to give benzaldehyde, followed by Knoevenagel reaction catalyzed by basic species (Scheme IV-2). The progress and yield of the reaction were characterized by ^{1}H NMR spectroscopy on the basis of the different chemical shift of the hydrogen atoms on reactant and products (as shown in blue color). To further confirm these, ^{13}C NMR spectroscopy was also measured, and the results are in good agreement with those of ^{1}H NMR. The reactions were performed using about 2.0 mmol substrates in DMSO-d_6 solvent with 0.01 mmol PCN-527-Cd for 12 h. PCN-527-Cd displayed a very low catalytic activity with conversion and yield of about 22 % for dimethoxymethylbenzene (R_1 = —CH_3, R_2 = —H).

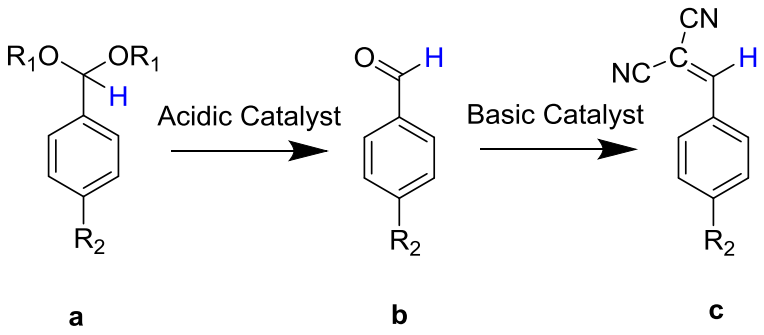

Scheme IV- 2. One-pot conversion deacetalization-Knoevenagel condensation reaction. (The ^{1}H NMR spectrum for hydrogen atoms shown in blue color are about 5.3 ppm, 10.0 ppm, and 8.5 ppm for a, b, and c respectively.)

4.3.3 Single-Crystal-to-Single-Crystal Transformation of PCN-527-Cd

The low yield of this reaction could be ascribed to the weak Lewis acidity of Cd (II). Therefore, increasing the Lewis acidity of the metal nodes in PCN-527-Cd likely will enhance the catalytic activity. Recently, our group reported a metal metathesis process in MOF from a low valent Mg (II) to high valent Fe (III) and Cr (III) nodes through the PSMO (post-synthetic metathesis and oxidation) method. [208] Due to the similar coordination mode of Fe (II) and the weak Cd-N coordination bond in PCN-527-Cd, the PMSO method could be adopted here to increase the catalytic activities. According to the literature[208], the as-synthesized PCN-527-Cd crystals were washed using DEF several times. The solution was bubbled with nitrogen for about 20 min, and anhydrous $FeCl_2$ was added under the protection of nitrogen. The exchange process was performed at 85 °C for 4 h. After the completion of the exchange, the reaction system was then exposed to the air. The energy-dispersive X-ray spectroscopy (EDS, Figure IV-2) and single crystal X-ray diffraction results revealed that 95 % of Cd was exchanged with Fe in a single-crystal-to-single-crystal (SC-SC) transformation to obtain PCN-527-Fe (CCDC 1450671). Similar results was also observed by ICP-MS (Table IV-1). The crystal data is similar to that of PCN-527-Cd. In comparison, the exchange is incomplete at room temperature and the corresponding exchange rates are 76%.

In order to confirm the oxidation state of products, we preformed XPS (Figure IV-3) measurement for PCN-527-Fe. For the spectrum of PCN-527-Fe, the $Fe2p_{3/2}$ signal at 713.21eV with the satellite peak well indicate the Fe^{3+} species in sample. [339,340]

Element	Weight %	Atomic %
C K	46.52	61.65
N K	18.59	21.12
O K	9.36	9.31
Cl K	5.41	2.43
Fe L	18.38	5.24
Cd L	1.74	0.25
Totals	100.00	

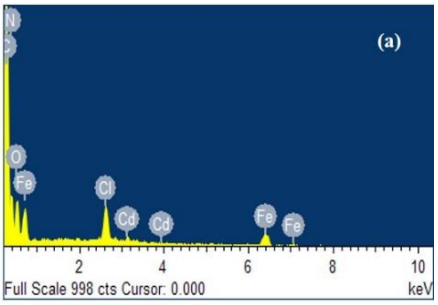

Element	Weight %	Atomic %
C K	45.69	60.58
N K	8.06	9.16
O K	24.30	24.19
Cl K	4.72	2.12
Fe L	10.51	3.00
Cd L	6.73	0.95
Totals	100.00	

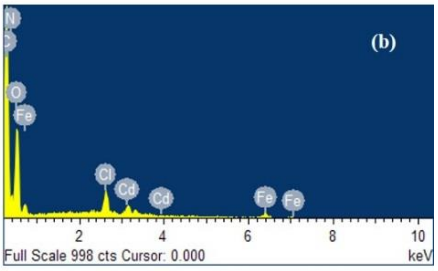

Figure IV- 2. The EDS results of PCN-527-Fe obtained at different temperature: (a) 85 °C; (b) room temperature.

Table IV- 1. The ICP-MS results of PCN-527-Fe obtained at 85 °C.

	Trial 1	Trial 2	Trial 3	Average
Cd content %	9.98	11.71	11.08	10.92
Fe content %	90.02	88.29	88.92	89.08

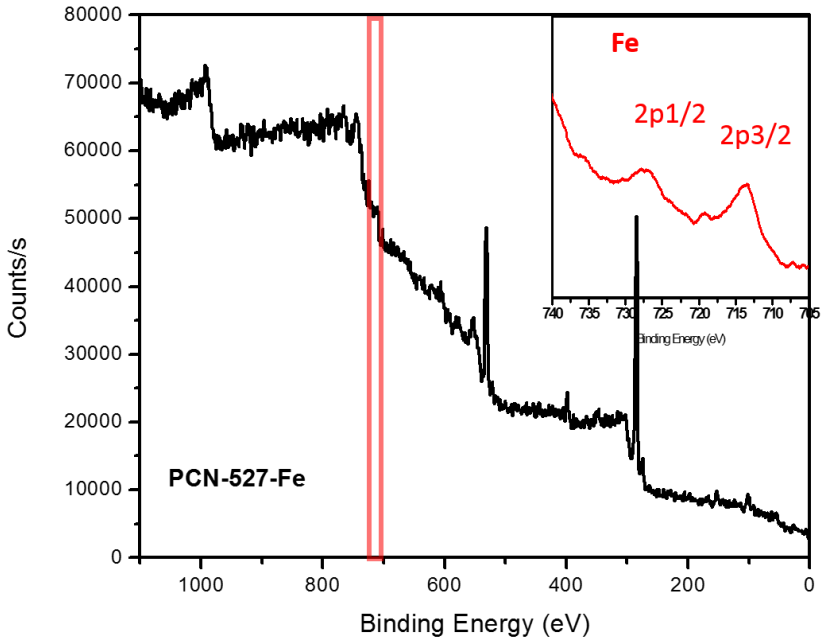

Figure IV- 3. The XPS results of PCN-527-Fe.

4.3.4 Catalysis of One-pot deacetalization-Knoevenagel Condensation Reaction by PCN-527-Fe

As we expected, the catalysis performance for the deacetalization-Knoevenagel condensation reaction using PCN-527-Fe was dramatically improved due to the stronger Lewis acidity of Fe (Table IV-2). For dimethoxymethylbenzene (R_1 = —CH_3, R_2 = —H) and 4-bromobenzaldehyhde diethyl acetal (R_1 = —C_2H_5, R_2 = —Br), the conversion ratio and the yield of final product were as high as 100 %. Moreover, using this strategy, other active metal ions can be introduced into the framework of PCN-527 conveniently to form synergic effect with the metal center in porphyrin linker as well as the

tetrazolates. This may result in more multifunctional materials, such as photocatalysis and magnetism, which is worthy of further investigations in future.

Table IV- 2. One-pot deacetalization-Knoevenagel condensation reactions. (* The conversion and yields were calculated from the integration of hydrogen atom as shown in Scheme V-2 in ^{1}H NMR at the end of the reaction)

Entry	Catalyst	Substrate	Conv.* of **a** (%)	Yield* of **b** (%)	NMR Yield* of **c** (%)
1	PCN-527-Cd	R_1 = - CH_3, R_2 = - H	22	Trace	22
2	PCN-527-Fe	R_1 = - CH_3, R_2 = - H	≈100	Trace	≈100
3	PCN-527-Fe	R_1 = - C_2H_5, R_2 = - Br	≈100	Trace	≈100

4.3.5 Identification of Catalytic Site of PCN-527-Fe in the deacetalization-Knoevenagel Condensation Reaction

In order to identify the catalytic site of PCN-527, a series of control experiments were performed under similar experimental conditions in the catalysis of dimethoxymethylbenzene. Table IV-3 summarized the results. It can be concluded that neither of the nitrogen of tetrazolate nor the iron coordinated in the middle of porphyrin involve in the catalysis of deacetalization-Knoevenagel condensation reaction.

Table IV- 3. Screening experiments. (× means absent; √ means present).

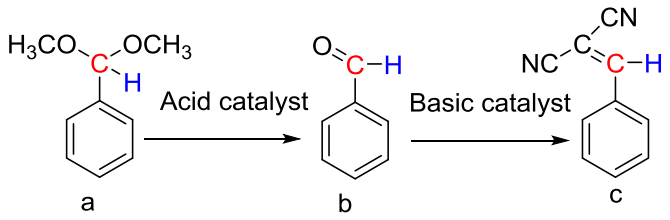

Reaction	Catalyst	a	b	c
	Theoretical ^{1}H (in blue)	5.3 ppm	10.0 ppm	8.5 ppm
4	H_2TTPP	×	×	×
5	H_2TTPP(Fe)	×	√	√
	Theoretical ^{13}C (in red)	103 ppm	191 ppm	161 ppm
4	H_2TTPP	×	×	×
5	H_2TTPP(Fe)	×	×	√

4.4 Summary

In conclusion, a nitrogen-rich porphyrinic MOF with a rare (4,8)-connected **scu** topology, PCN-527, was prepared via a topology-guided synthesis method. It can be successfully converted from a catalytically inert material to an active catalyst in a single-crystal-to-single-crystal transformation utilizing the post-synthetic metathesis strategy, which exhibits a high activity in one-pot deacetalization-Knoevenagel condensation reactions.

CHAPTER V

ROBUST ZIRCONIUM METAL-ORGANIC FRAMEWORKS FOR METHANE STORAGE

5.1 Introduction

Porous materials, such as zeolites and activated carbons, have served as gas media for industrial applications in storage, separations and catalysis.[341] Traditional porous materials, such as carbon nanotubes, zeolites and activated carbon, have been extensively studied for gas storage. Metal-organic frameworks (MOFs), a fascinating family of inorganic-organic hybrid material, are porous coordination networks constructed from metal clusters (secondary building units or SBUs) and organic linkers.[7] The combination of organic units as the struts and the polynuclear-metal units as the vertices forms rigid 3-D architectures.[22] . One of the unique benefits of MOFs is that the pore size and the internal pore surface functionalities can be tuned by using pre-designed organic linkers, which, according to the theory of isoreticular chemistry, will not alter the underlying topology.[7,2,61,342-344] In addition, the highly ordered structure possesses permanent porosity after activation, which allows small gas molecules to diffuse into the pores without causing framework collapse or large characteristic changes in the structure. Therefore, MOFs are one of the best candidates for designated gas capture and storage.

The ongoing studies for alternative energy carriers for supplement or replace conventional petroleum fuels have grown at a high rate. Methane has a gravimetric heat

of combustion of 55.7 MJ/kg, which is almost 10 MJ/Kg higher compared to that of gasoline (46.4 MJ/kg). Moreover, combustion of methane boasts the smallest amount of CO_2 per unit of heat produced among all the fossil fuels. In this context, natural gas stands out as a leading alternative fuel source compared to traditional fuels. However, the lack of efficient storage techniques hampers its applications in motor vehicles. Substantial studies have suggested that porous adsorbents represent a safer, simpler, and potentially more cost-efficient method for methane storage at ambient temperature and reasonable pressure.[341] The Grand Canonical Monte Carlo (GCMC) simulation, modeling the equilibrium between the bulk methane phase and the adsorbed phase, uncovered that the best material to achieve high gravimetric methane adsorption should have a large accessible surface area, high free volume, low framework density, and strong energetic interactions with the adsorbed methane molecules.[160] Detailed studies on tuning of pore size and modification of pore surface presents a promising initial step towards selecting MOF candidates for high methane uptake.

Despite the fantastic advantages MOFs can offer, the application of MOFs in industrial settings, especially for gas storage, is highly limited by the sensitivity towards moisture.[345] Zr-based MOFs have exhibited remarkable chemical and thermal stability, which makes them more applicable for commercialization. This stability has been accredited to high-valent oxophilic Zr^{4+} cation and the high nuclearity of the $[Zr_6O_4(OH)_4]$ metal cluster.[15] Recently, our group has demonstrated PCN-22X (PCN stands for Porous Coordination Network), a series of Zr-MOFs constructed by metalloporphyrin linkers with Zr_6 clusters showing excellent stability in acid/base or

aqueous environments at elevated temperatures.[346] Meanwhile, a series of Zr-MOFs synthesized by post synthetic modification, named as the PCN-5X series, also demonstrated the ability to survive under harsh conditions.[347] Herein, the Zr-based MOFs have addressed the problem of chemical and thermal stability observed in traditional copper and zinc MOFs.

Within the rapidly growing field of MOF research, studies of the porosity and functionality are exceedingly attractive. The IRMOF materials with bromo, amino, n-propoxy, n-pentoxy, cyclobutyl, and fused benzene functional groups have demonstrated significant influences on the methane storage capacity as well as the cavity and crystal density variation within a particular framework.[26] Among all the IRMOFs, the hydrophobic C_2H_4 side chain on the linkers in IRMOF-6 greatly enhanced the methane storage (155 cm^3 standard temperature and pressure (STP)$\cdot g^{-1}$) compared to that of the unfunctionalized IRMOF-1 (135 cm^3 (STP)$\cdot g^{-1}$). Therefore, one possible method for enhancing gas uptake capacities is to incorporate pendant hydrophobic alkyl chains on the linkers. Moreover, the introduction of various side chains on the organic linkers in mesoporous materials might tune the pore size precisely to best fit methane molecules and eventually increase the host-guest interactions to achieve optimal adsorption performance.

Current pioneers in this area of research have been dedicated to the MOFs with first-row late transition metals, especially zinc and copper. The poor moisture stability of these MOFs limited their utility for industrial application. As methane storage research shortly began, the extension to the stable MOF design for methane storage is quite rare,

with only a handful of systems studied to date.[341] Recent work from Zhou's group found that increasing the side chain of the linker would result in increased moisture stability of corresponding frameworks.[348] Moreover, previous investigation of PCN-14 developed from an anthracene derivative exhibited an absolute methane-adsorption capacity of 230 v/v, which exceeded the previous Department of Energy(DOE) target (180 v/v).[283] It occurred to us that the side chain of linkers could intensify the MOF-methane interactions and consequently improve the total methane capacity.

Recent work on a series of Zr-based MOFs from Maurin's group reveals that the highly porous UiO-67(Zr) and UiO-68(Zr) materials show high methane adsorption capacities.[197] Remarkably, the thermal, water and mechanical stability tests revealed that the porosity was retained up to 450 ^{O}C, in water at room temperature overnight, and upon the application of uniaxial pressure, respectively. All of the results are in good agreement with our objective to synthesize stable Zr-MOFs with high methane adsorption capacity.

We hypothesize that MOFs constructed from Zr-oxoclusters and different lengths of side chains on linkers would afford a stable system to serve as a fuel adsorbent. By tuning the material via different side chains, a higher methane storage capacity to fulfill the new DOE target could be reached. In principle, longer side chains in the framework can provide more interaction sites for the methane molecules (guest), decrease the dead volume inside the framework, and thus improve the volumetric adsorption capacity. A potential drawback involving the elongation of side chains in MOFs is the decline of accessible surface area and pore volume. In order to compromise this drawback while

withholding extra adsorption sites, an evaluation of the relationship between the length of side chains and methane storage capacity is necessary.

5.2 Experimental Section

5.2.1 Materials and Instrumentation

Materials

Zirconium(IV) chloride, N,N-dimethylformamide (DMF), hexanes, ethyl acetate, methanol (MeOH), tetrahydrofuran (THF), dichloromethane (CH_2Cl_2), Acetone, hydrochloride acid (HCl), 1,2-dimethoxyethane (DME), ethanol, benzoic acid, 1,4-diethylbenzene, and 1,4-dibromo-2,5-dihexylbenzene were purchased from either Alfa Aesar or Sigma Aldrich. Tetra (triphenylphosphine) palladium (0) ($Pd(PPh_3)_4$) was purchased from Matrix Scientific. 1.4 Diiodo-2, 5-dimethyl benzene, 1, 4-Diethyloxybenzene were purchased from TCI.4-Methoxy carbonylphenylboronic acid was purchased from AK Scientific Inc. Silica gel was purchased from Silicycle Inc. Unless otherwise noted, all chemicals were used without further purification.

Instrumentation

Single crystal X-ray data were collected on a Bruker Smart Apex diffractometer equipped with a fine-focus sealed-tube X-ray source (Mo-Kα radiation, $\lambda = 0.71073$ Å, graphite monochromated) and a low temperature device. Powder X-ray diffraction (PXRD) was performed on a Bruker D8-Focus Bragg-Brentano X-ray Powder Diffractometer equipped with a Cu sealed tube ($\lambda = 1.54178$ Å) at 40 kV and 40 mA.

Nuclear magnetic resonance (NMR) data were collected on a Mercury 300 spectrometer. All the N_2 adsorption-desorption isotherms were measured using a Micrometritics ASAP 2020 system at 77K. The high pressure methane isotherms were collected using Particulates System High Pressure Volumetric Analyzer (HPVA) II instrument using UHP methane gases. Thermogravimetric analysis (TGA) was conducted on a TGA-50 (SHIMADZU) thermogravimetric analyzer from room temperature to 700 °C at a ramp rate of 2 °C/min in a flowing nitrogen atmosphere. Synchrotron powder X-ray diffraction (PXRD) under high-pressure measurement was carried out with Bruker D8-Discover diffractometer equipped with a Mo sealed tube (λ = 0.72768Å) on the beamline 17-BM at the Advanced Photon Source, Argonne National Laboratory.

5.2.2 Ligand Synthesis

Synthesis of 2',5'-dimethyl-[1,1':4',1''-terphenyl]-4,4''-dicarboxylic acid (H_2TPDC-2Me) and 2',5'-tetramethyl-[1,1':4',1''-terphenyl]-4,4''-dicarboxylic acid (H_2TPDC-4Me) for Control Experiment

The linker of H_2TPDC-2Me and H_2TPDC-4Me are synthesized according to the literature.[347]

General Procedure

Most of the ester precursors of linear ligand 1,1':4', 1"-terphenyle-4, 4"-dicarboxylate (TPDC) derivatives are synthesized through Suzuki Coupling reactions between the dihalobenzene derivatives and 4-methoxyl carbonylphenylboronic acid

using tetrakis(triphenylphosphine)palladium(0) as the catalyst in the presence of 1,4-dimethoxyethane (DME). After base-assisted hydrolysis, the corresponding linear carboxylate ligands were obtained as either light yellow solid (R=OMe) or white fine powder (R=OEt, n-C_6H_6) (Scheme V-1).

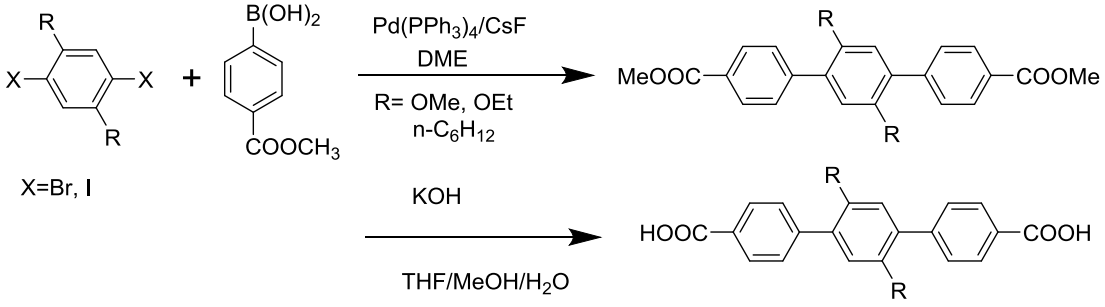

Scheme V- 1. Synthesis of H_2TPDC-R.

Synthesis of 2',5'-diethyl-[1,1':4',1''-terphenyl]-4,4''-dicarboxylic acid (H_2TPDC-2Et)

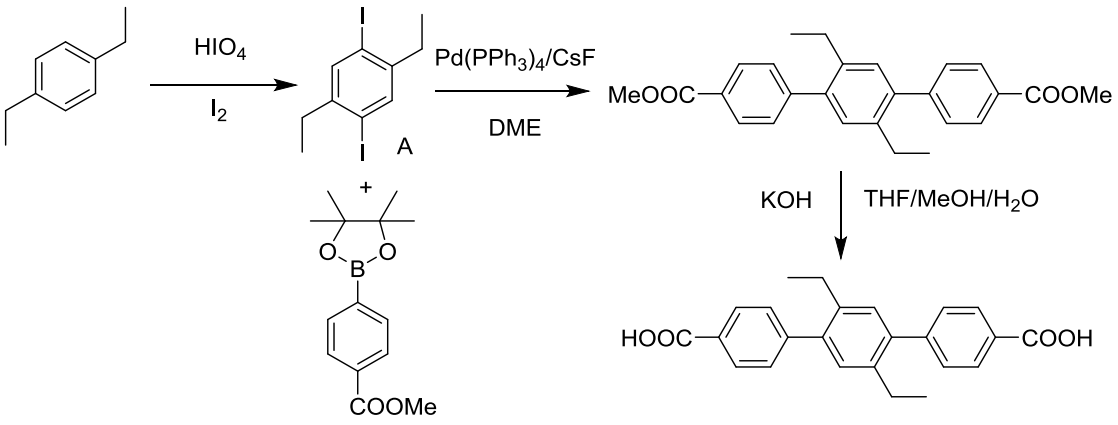

Scheme V- 2. Synthesis of H_2TPDC-2Et.

Synthesis of 1,4-Diiodo-2,5-diethylbenzene (A) was based on the reported literature [[349]] shown in Scheme V-2.

Synthesis of 4, 4'-(9, 10-anthracenediyl) dibenzoic acid

Yellow fine powder was synthesized according to the literature procedure[350], starting from 9, 10-dibromo anthracene(Scheme V-3).

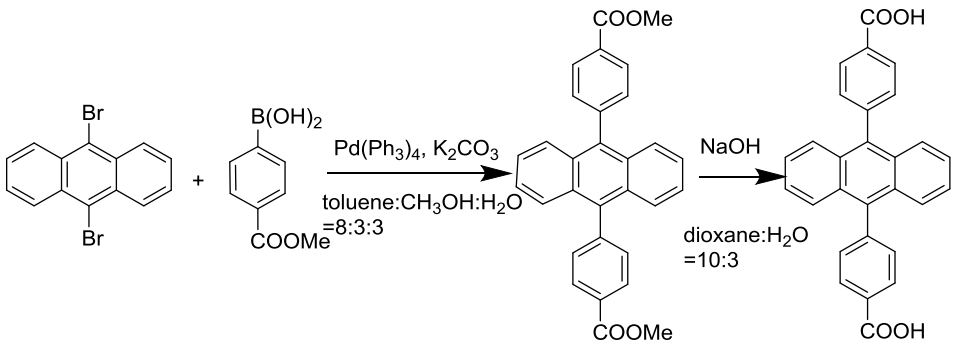

Scheme V- 3. Synthesis of 4, 4'-(9, 10-anthracenediyl)dibenzoic acid.

Synthesis of 2',5'-bis(trifluoromethyl)-[1,1':4',1''-terphenyl]-4,4''-dicarboxylic acid

Similar procedure except the starting materials of 1,4-dibromo-2,5-bis(trichloromethane)benzene shown in Scheme V-4.

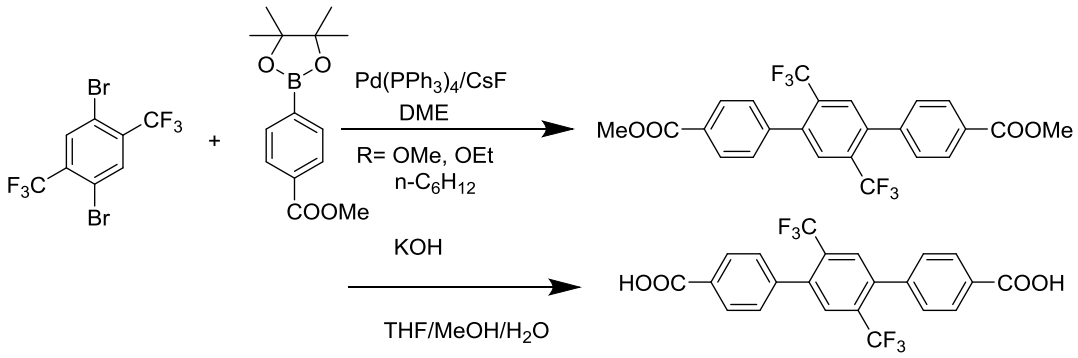

Scheme V- 4. Synthesis of H_2TPDC-2CF_3.

Synthesis of 2',5''-dihexyl-[1,1':4',1''-terphenyl]-4,4''-dicarboxylic acid

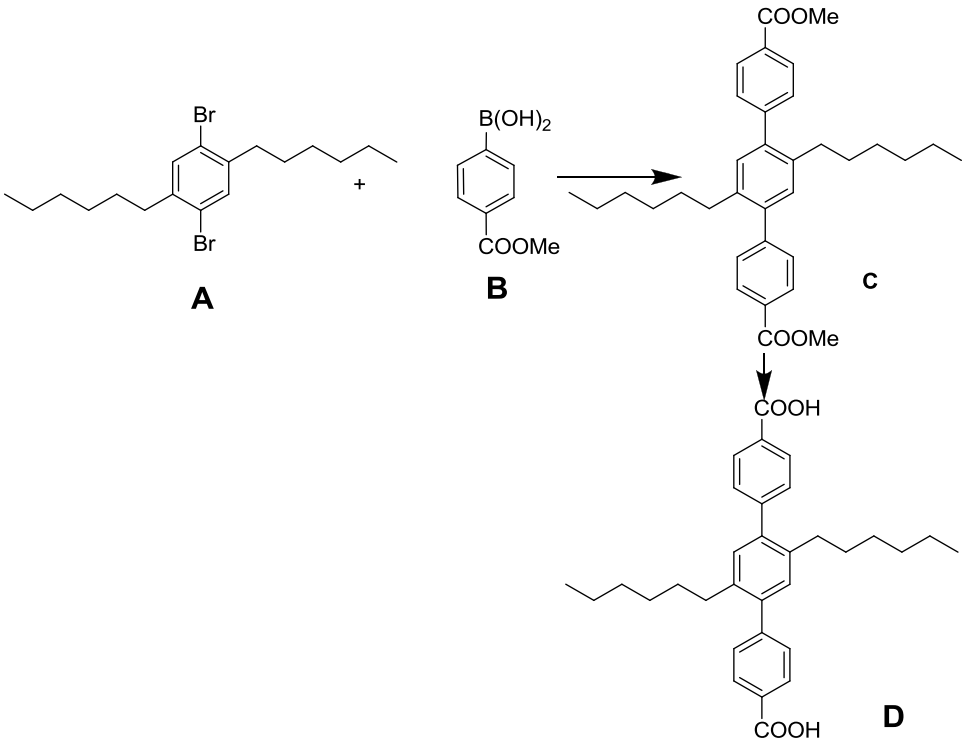

Scheme V- 5. Synthesis of H_2TPDC-2Hex.

Similar procedure except the starting materials of 1,4-dibromo-2,5-dihexylebenzene shown in Scheme V-5.

5.2.3 MOF Synthesis

Zirconium (IV) chloride (24 mg) and triphenyl dicarboxylic acid (TPDC) derivatives (30 mg) were mixed in 2 mL N, N'-dimethylformamide (DMF). Under the solvothermal conditions of 100 ^{O}C for 48 hr modulated by benzoic acid (240 mg-420 mg), yellow powder was obtained for the anthracene-based ligand while colorless single crystals for the rest.

5.2.4 Structure Determination of Single Crystals

Single-crystal X-ray data frames of PCN-56X were collected using the program APEX 2 and processed using the program *SAINT* routine within *APEX 2*. The data were corrected for absorption and beam corrections based on the multiscan technique as implemented in *SADABS.* The structure was solved by direct methods and refined by full-matrix least-squares on F^2 with anisotropic displacement using the *SHELXTL* software package. Non-hydrogen atoms were refined with anisotropic displacement parameters during the final cycles. Hydrogen atoms on carbon and nitrogen were calculated in ideal positions with isotropic displacement parameters set to 1.2 × U_{eq} of the attached atoms, but hydroxide hydrogen atoms were not added into the structure. Contributions to scattering due to these solvent molecules were removed using the *SQUEEZE* routine of *PLATON*, and the structures were then refined again using the data

generated. The contents of the solvent region are not represented in the unit cell contents in the crystal data.

5.2.5 Activation Procedures and Gas Sorption Measurements

All the as-synthesized single crystals of PCN-56X were washed with fresh DMF for three times. In particular, those crystals synthesized with benzoic acid were immersed in fresh DMF at 60^{O}C and exchanged with fresh DMF for another three times. All the MOFs were exchanged with dry CH_2Cl_2 three times before the activation of vacuum and heat. Then the MOFs were heated at 100^{O}C for 10 hours under vacuum to get ready for gas measurement.

5.3 Results and Discussion

5.3.1 Characterization of Crystal Structures

Under the solvothermal conditions modulated by benzoic acid, yellow powder was obtained for the anthracene-based ligand, while colorless single crystals (Figure V-1 a) were achieved for the remaining ligands. Single crystal XRD analysis displays that MOFs in the PCN-56X series crystalizes in the space group of $Fm\bar{3}m$. All adopt a general formula of $Zr_3O_2(OH)_2(TPDC\text{-}R)_3$ [R= OMe (PCN-561), OEt (PCN-562), CF_3 (PCN-564), Et (PCN-565), n-C_6H_{12} (PCN-566), and anthracene-based linker (PCN563)], which are confirmed to be isoreticular to PCN-56 [347] and UiO-68 [15] structures (Figure V-1b). Six Zr atoms in the square-antiprismatic coordination environment are linked by eight O atoms from four carboxylates and four alternatives of

μ_3-O and μ_3-OH on the triangle face to form a $[Zr_6O_4(OH)_4]$ core cluster. Each of the $[Zr_6O_4(OH)_4]$ cluster is connected by twelve carboxylates from the organic linkers, which gives rise to a 3-D network. There are two types of polyhedron cages—a tetrahedral cage, consisting of four Zr_6 clusters and six linkers with a cavity diameter of ~1.1nm (FigureVI-1c), and also an octahedral cage, comprised by six Zr_6 clusters with twelve organic linkers with a cavity diameter around 2.2 nm (Figure V-1d).

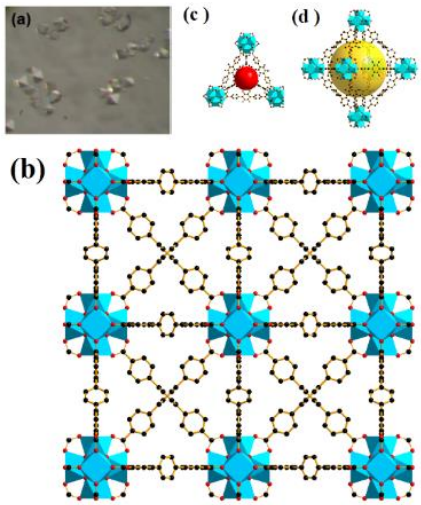

Figure V- 1. (a) Colorless crystals for PCN-56X; (b) Isoreticular structure of UiO-68; (c) Tetrahedral Cage; (d) Octahedral Cage.

5.3.2 Porosity and BET Surface Area Study

In order to characterize the porosity of those isoreticular MOFs, the nitrogen gas sorption isotherms were measured and the Brunauer-Emmett-Teller (BET) surface areas were calculated in the range of 1447-4449 m^2/g (Figure V-2 and Table V-1). As we

expected, the surface areas of PCN-561, PCN-562, and PCN-564 fall into the range of 2000~3000 m^2/g, which has been shown to be suitable for methane storage.[341] Attaching of ethyl groups in PCN-565 shows a significant enhancement of surface areas with a magnitude of 4449 m^2/g, which is almost a 60% increase. This dramatically difference is attributed to the efficient packing of gas molecules and the decrease of the dead volume. Theoretically, the total methane uptake will increase along with the increase of BET surface area. On the other hand, we also observe that the inclusion of longer pendent side groups (such as hexyl) display a decrease of the BET surface area (1447 m^2/g for PCN-566 vs 2794 m^2/g for PCN-56).

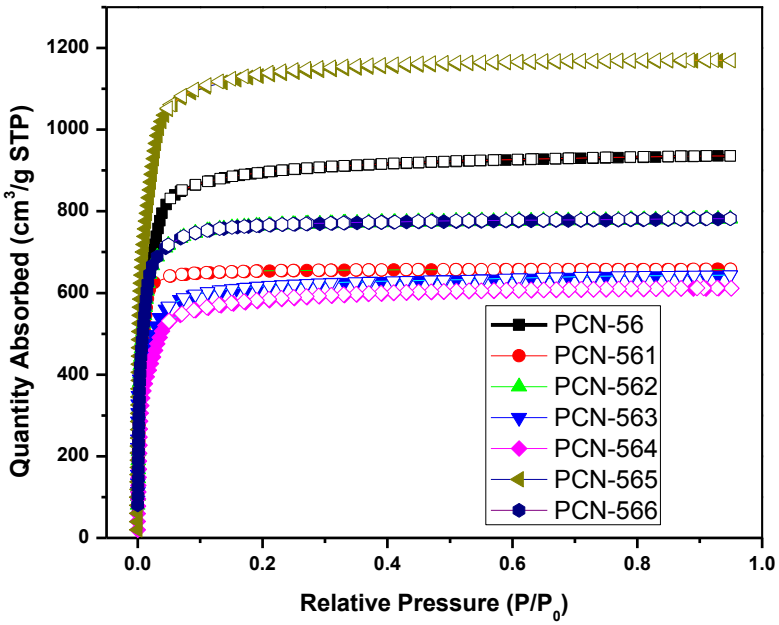

Figure V- 2. Nitrogen sorption of the PCN-56X series.

Table V- 1. The surface areas of PCN-56X based on N_2 isotherms.

PCN#	R=	BET Surface Area ($m^2 \cdot g^{-1}$)	Langmuir Surface Area ($m^2 \cdot g^{-1}$)
PCN-56	$-CH_3$	2794	4092
PCN-561	$-OCH_3$	2470	2724
PCN-562	$-OCH_2CH_3$	2676	3408
PCN-563	Anthracene	1729	3184
PCN-564	$-CF_3$	2249	2622
PCN-565	$-CH_2CH_3$	4449	5088
PCN-566	$-CH_2CH_2CH_2CH_2CH_3$	1447	2142

5.3.3 Methane Uptake at Low Pressure

Methane uptakes at 195K were further tested as shown in Figure V-3. Changes from methyl groups (PCN-56) to methoxy groups (PCN-561) do not show any significant influence on methane uptake at low pressure, where the introduction of polarizability did not attribute to the uptake. PCN-562 and PCN-563 are the best candidates among the PCN-56X series. Compared to the control set of PCN-56 (Me), both the ethoxy groups in PCN-562 and the central anthracene groups in PCN-563 provide more interaction points. The ethoxyl groups in PCN-562 not only introduce more polarizability but also provide additional carbon chains to interact with methane molecules, which eventually add to the total methane uptake. Therefore, an

enhancement is observed. In addition, it is worth noting that PCN-563 was obtained in powder form due to the poor solubility of anthracene-based linker. In general, a limited crystallinity likely lead to a reduced methane adsorption. Previous studies display that benzene has a significant affinity to methane. [200] Herein, the influence of the additional benzene overweigh that of crystallinity on methane uptake. Surprisingly, the methane uptake of PCN-565 is the lowest. According to the N_2 adsorption measurements, PCN-565 provides more accessible surface area compared to any other MOFs in the series; this indicates that the methane uptake may not directly correlate to the surface area at some extent, where a larger surface area would have loosely-packed methane molecules with resultant low overall gravimetric uptake. [200] Moreover, longer chains, such as the hexyl groups, in PCN-566 block the pores and essentially decrease the accessibility to these pores, leading to a low methane uptake.

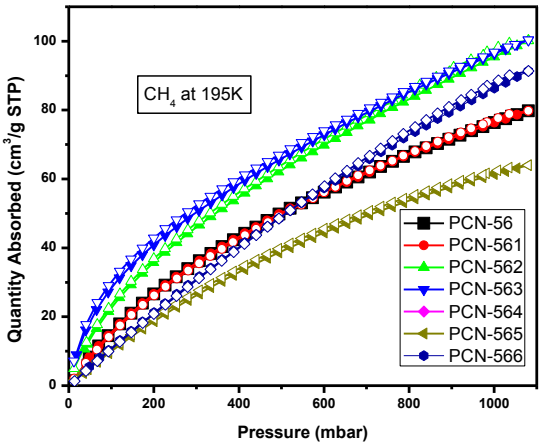

Figure V- 3. Methane uptake at 195K at low pressure.

5.3.4 High Pressure Methane Uptake

The high-pressure methane uptakes of the PCN-56X series were measured and shown in Figure V-4. Unlike the methane uptake results at low pressure, the inclusion of polar methoxy and ethoxy groups in PCN-561 and PCN-562, respectively, attribute to higher overall methane capacities at high pressure compared to those of the methyl groups in PCN-56 and the ethyl groups in PCN-565. Moreover, the methane sorption isotherm of PCN-565 is likely caused by the surface adsorption, which means the framework collapses under high pressure. This is also evident by the zero BET surface area of PCN-565 after the high pressure measurement. Any more polar groups (such as $-CF_3$ in PCN-564) reduce the interactions between the framework and methane molecules. Also, any longer carbon chains, the hexyl groups in PCN-566 here, will again block the accessible area for methane molecules.

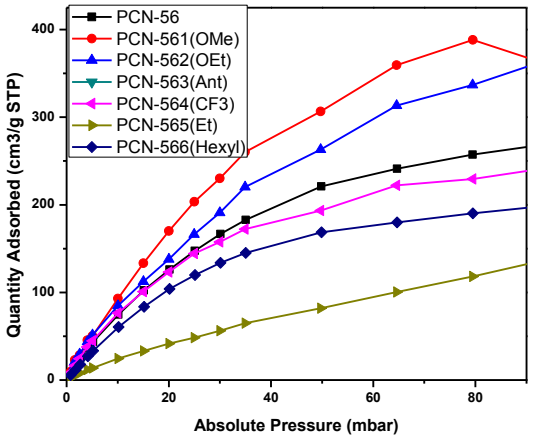

Figure V- 4. Methane storage capacity at high pressure of PCN-56X series.

5.3.5 Moisture Stability of PCN-56X

The moisture stability tests were also performed to confirm the side chain effects on the framework stability. The PXRD spectra of these isoreticular Zr-based MOFs were collected before and after exposure to the lab environment for six weeks (Figure V-5). As we expected, good moisture stabilities of PCN-56X were observed with the inclusion of different side chains. Again, PCN-565 (Et) is so porous that the framework collapses after six weeks.

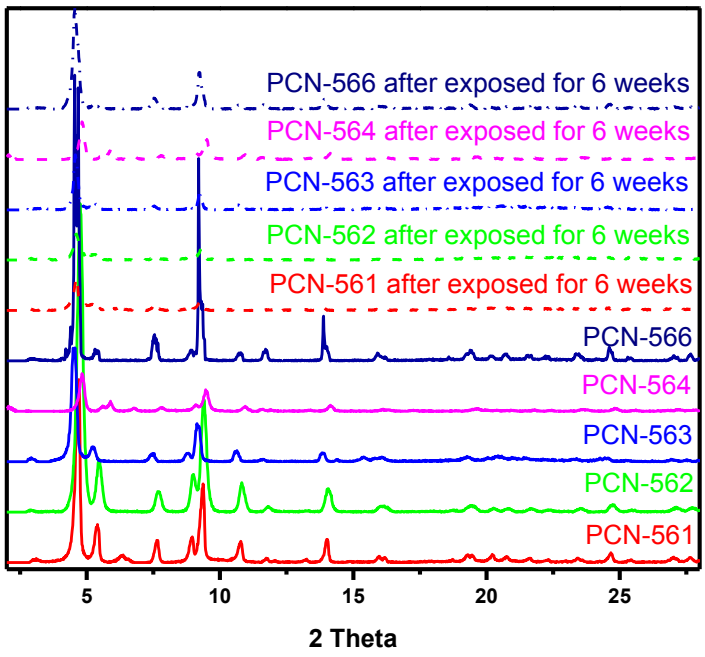

Figure V- 5. PXRD pattern before and after exposing PCN-56X series to air after six week at ambient condition.

5.4 Summary

Overall, a series of Zr-MOFs with enhanced methane storage capacity and excellent stability were successfully synthesized. After proper selection of side chains, the overall methane uptake could be significantly increased. In this study, it was found that materials with large surface areas in this UiO system will not necessarily possess a high methane uptake. Therefore, there was a tradeoff between the addition of the interaction points and the accessibility of gas molecules. Based on our study, the introduction of polarizability on the side chains will not improve the methane-framework interactions at low pressure. However, significant enhancements were displayed at high pressure. Overall, the introduction of side chains could significantly improve the packing efficiency of methane in the MOFs. Most importantly, those Zr-MOFs also show excellent moisture stability, which promises reusability.

CHAPTER VI

CONCLUSION

This dissertation has described the rational design and synthesis of various MOFs with exceptional topology, porosity, stability, and functionality. In the first project, the employment to the guidance of topological analysis led to the production of a three-dimensional ionic framework called PCN-99 (PCN=Porous Coordination Polymer). In this structure, a rare mesoporous cavity and one-dimensional mesoporous channel were produced. The anionic nature of PCN-99 shined light on the successful encapsulation of catalytic-active $Ru(bpy)_3^{2+}$ cation by electrostatic selection. The resultant heterogeneous system could catalyze the aerobic oxidative hydroxylation of arylboronic acid under visible light.

In the second project, I described the utilization of a template of magnesium-based MOF PCN-430-Mg for post-synthetic metathesis. After exchanging PCN-430-Mg with all the first row transition metals, several guidelines were concluded for a complete metal exchange. First, the parent framework has to be flexible enough to accommodate any structural changes during the exchange process. In general, a large pore size will facilitate the access of the entering metal to the SBUs. Moreover, the exchange process will be much more convenient if the SBUs includes coordinated solvent molecules or potential open metal sites. However, the coordination environment of the entering metal and the parent metal must match with each other. Otherwise, partial exchange could

happen. If the final coordination between the linker and entering metal is not thermodynamically stable, other relative stable phases will be produced.

Taking advantage of the guidelines learned about the post-synthetic metathesis from the last project, I successfully applied these to activate an inert porphyrinic tetrazolate-based MOF PCN-527-Cd via post-synthetic metathesis in a single-crystal-to-single-crystal transformation. The responding PCN-527-Fe demonstrated a very high activity in one-pot deacetalization-Knovenagel condensation reactions.

In the last project, I was able to design and synthesize stable Zr-MOFs constructed from Zr_6 clusters and functionalized organic linkers under a rational design. This series of Zr-based MOF PCN-56X (X=1-6) demonstrated good moisture stability. It was found that the addition of methoxyl and ethoxyl functional group significantly increased the overall methane uptake at high pressure, and this trend was not observed in either low pressure methane uptake or nitrogen isotherms. Adjusting the length of side chain in the framework have a dramatic influence on the total methane storage capacity at high pressure.

In conclusion, stability and functionality have been significant problems in the applications of MOFs. Materials with desirable properties here in this dissertation can be approached via both rational design for direct synthesis and post-synthetic metathesis. From the aspect of direct synthesis, rational design is the key to produce perspective MOFs. The design principles include the precise choice of organic linkers and metal ions under topological design in Chapter II, and the modification on the organic linkers based on the structural analysis in Chapter V. On the other hand, the second approach is

through post-synthetic metathesis. Templating the magnesium-based MOFs, previous study has shown robust iron (III)- and chromium (III)-based MOFs could be achieved as. Moreover, specific structural factors in either parent or daughter MOFs play a central role for a complete metal exchange (Chapter III). Once all those structural factors fulfill all the prerequisites, other functional MOFs could be produced with improved performance (Chapter IV). Overall, those works not only provide a systematic way of designing functional and robust MOFs but also shed light on the synthesis of other advanced functional materials.

REFERENCES

(1) Batten, S. R.; Champness, N. R.; Chen, X.-M.; Garcia-Martinez, J.; Kitagawa, S.; Öhrström, L.; O'Keeffe, M.; Paik Suh, M.; Reedijk, J. In *Pure and Applied Chemistry* 2013; Vol. 85, p 1715.

(2) Kitagawa, S.; Kitaura, R.; Noro, S.-i. *Angewandte Chemie International Edition* **2004**, *43*, 2334.

(3) Zhang, M.; Chen, Y.-P.; Bosch, M.; Gentle, T.; Wang, K.; Feng, D.; Wang, Z. U.; Zhou, H.-C. *Angewandte Chemie International Edition* **2014**, *53*, 815.

(4) Feng, X.; Ding, X.; Jiang, D. *Chemical Society Reviews* **2012**, *41*, 6010.

(5) Lee, J.; Farha, O. K.; Roberts, J.; Scheidt, K. A.; Nguyen, S. T.; Hupp, J. T. *Chemical Society Reviews* **2009**, *38*, 1450.

(6) Murray, L. J.; Dinca, M.; Long, J. R. *Chemical Society Reviews* **2009**, *38*, 1294.

(7) Zhou, H.-C.; Long, J. R.; Yaghi, O. M. *Chemical Reviews* **2012**, *112*, 673.

(8) Lee, Y.-R.; Kim, J.; Ahn, W.-S. *Korean Journal of Chemical Engineering* **2013**, *30*, 1667.

(9) Makal, T. A.; Yuan, D.; Zhao, D.; Zhou, H. C. In *The Chemistry of Nanostructured Materials*; Yang, P., Ed.; World Scientific: Singapore, 2011; Vol. II, p 37.

(10) Biemmi, E.; Christian, S.; Stock, N.; Bein, T. *Microporous and Mesoporous Materials* **2009**, *117*, 111.

(11) Li, H.; Eddaoudi, M.; O'Keeffe, M.; Yaghi, O. M. *Nature* **1999**, *402*, 276.

(12) Eddaoudi, M.; Kim, J.; Rosi, N.; Vodak, D.; Wachter, J.; O'Keeffe, M.; Yaghi, O. M. *Science* **2002**, *295*, 469.

(13) Chui, S. S.-Y.; Lo, S. M.-F.; Charmant, J. P. H.; Orpen, A. G.; Williams, I. D. *Science* **1999**, *283*, 1148.

(14) Férey, G.; Mellot-Draznieks, C.; Serre, C.; Millange, F.; Dutour, J.; Surblé, S.; Margiolaki, I. *Science* **2005**, *309*, 2040.

(15) Cavka, J. H.; Jakobsen, S.; Olsbye, U.; Guillou, N.; Lamberti, C.; Bordiga, S.; Lillerud, K. P. *J. Am. Chem. Soc.* **2008**, *130*, 13850.

(16) Jhung, S. H.; Lee, J. H.; Yoon, J. W.; Serre, C.; Férey, G.; Chang, J. S. *Advanced Materials* **2007**, *19*, 121.

(17) Kerner, R.; Palchik, O.; Gedanken, A. *Chemistry of Materials* **2001**, *13*, 1413.

(18) Stock, N.; Biswas, S. *Chemical Reviews* **2012**, *112*, 933.

(19) Son, W.-J.; Kim, J.; Kim, J.; Ahn, W.-S. *Chemical Communications* **2008**, 6336.

(20) Mueller, U.; Schubert, M.; Teich, F.; Puetter, H.; Schierle-Arndt, K.; Pastre, J. *Journal of Materials Chemistry* **2006**, *16*, 626.

(21) Martinez Joaristi, A.; Juan-Alcañiz, J.; Serra-Crespo, P.; Kapteijn, F.; Gascon, J. *Crystal Growth & Design* **2012**, *12*, 3489.

(22) Tranchemontagne, D. J.; Mendoza-Cortes, J. L.; O'Keeffe, M.; Yaghi, O. M. *Chem Soc Rev* **2009**, *38*, 1257.

(23) Lu, W.; Wei, Z.; Gu, Z.-Y.; Liu, T.-F.; Park, J.; Park, J.; Tian, J.; Zhang, M.; Zhang, Q.; Gentle Iii, T.; Bosch, M.; Zhou, H.-C. *Chemical Society Reviews* **2014**, *ASAP*, 10.1039/C4CS00003J.

(24) Gagnon, K. J.; Perry, H. P.; Clearfield, A. *Chemical Reviews* **2011**, *112*, 1034.

(25) Shimizu, G. K. H.; Vaidhyanathan, R.; Taylor, J. M. *Chemical Society Reviews* **2009**, *38*, 1430.

(26) Eddaoudi, M.; Kim, J.; Rosi, N.; Vodak, D.; Wachter, J.; O'Keeffe, M.; Yaghi, O. M. *Science* **2002**, *295*, 469.

(27) Yaghi, O. M.; O'Keeffe, M.; Ockwig, N. W.; Chae, H. K.; Eddaoudi, M.; Kim, J. *Nature* **2003**, *423*, 705.

(28) Lu, W.; Wei, Z.; Gu, Z.-Y.; Liu, T.-F.; Park, J.; Park, J.; Tian, J.; Zhang, M.; Zhang, Q.; Gentle Iii, T.; Bosch, M.; Zhou, H.-C. *Chemical Society Reviews* **2014**, *43*, 5561.

(29) Rosi, N. L.; Kim, J.; Eddaoudi, M.; Chen, B.; O'Keeffe, M.; Yaghi, O. M. *J. Am. Chem. Soc.* **2005**, *127*, 1504.

(30) Caskey, S. R.; Wong-Foy, A. G.; Matzger, A. J. *J. Am. Chem. Soc.* **2008**, *130*, 10870.

(31) Deng, H.; Grunder, S.; Cordova, K. E.; Valente, C.; Furukawa, H.; Hmadeh, M.; Gándara, F.; Whalley, A. C.; Liu, Z.; Asahina, S.; Kazumori, H.; O'Keeffe, M.; Terasaki, O.; Stoddart, J. F.; Yaghi, O. M. *Science* **2012**, *336*, 1018.

(32) Fordham, S.; Wang, X.; Bosch, M.; Zhou, H.-C. In *Lanthanide Metal-Organic Frameworks*; Cheng, P., Ed.; Springer Berlin Heidelberg: Berlin, Heidelberg, 2015, p 1.

(33) Férey, G.; Serre, C.; Mellot-Draznieks, C.; Millange, F.; Surblé, D. S. J.; Margiolaki, I. *Angewandte Chemie International Edition* **2004**, *43*, 6296.

(34) Kim, M.; Cahill, J. F.; Su, Y.; Prather, K. A.; Cohen, S. M. *Chemical Science* **2012**, *3*, 126.

(35) Wang, C.; Wang, J. L.; Lin, W. *Journal of the American Chemical Society* **2012**, *134*, 19895.

(36) Wang, J.-C.; Liu, Q.-K.; Ma, J.-P.; Huang, F.; Dong, Y.-B. *Inorganic Chemistry* **2014**, *53*, 10791.

(37) Custelcean, R.; Moyer, B. A. *European Journal of Inorganic Chemistry* **2007**, *2007*, 1321.

(38) Quartapelle Procopio, E.; Fukushima, T.; Barea, E.; Navarro, J. A. R.; Horike, S.; Kitagawa, S. *Chemistry – A European Journal* **2012**, *18*, 13117.

(39) Gross, M. S.; Sánchez, B. S.; Querini, C. A. *Applied Catalysis A: General* **2015**, *501*, 1.

(40) Esteban, J.; Ladero, M.; García-Ochoa, F. *Chemical Engineering Journal* **2015**, *269*, 194.

(41) Karmakar, A.; Desai, A. V.; Ghosh, S. K. *Coordination Chemistry Reviews* **2016**, *307, Part 2*, 313.

(42) Chen, W.; Wang, J.-Y.; Chen, C.; Yue, Q.; Yuan, H.-M.; Chen, J.-S.; Wang, S.-N. *Inorganic Chemistry* **2003**, *42*, 944.

(43) Medina, M. E.; Dumont, Y.; Greneche, J.-M.; Millange, F. *Chemical Communications* **2010**, *46*, 7987.

(44) Burrows, A. D.; Cassar, K.; Friend, R. M. W.; Mahon, M. F.; Rigby, S. P.; Warren, J. E. *CrystEngComm* **2005**, *7*, 548.

(45) Liu, Y.; Kravtsov, V. C.; Larsen, R.; Eddaoudi, M. *Chemical Communications* **2006**, 1488.

(46) Nouar, F.; Eckert, J.; Eubank, J. F.; Forster, P.; Eddaoudi, M. *Journal of the American Chemical Society* **2009**, *131*, 2864.

(47) Sava, D. F.; Kravtsov, V. C.; Nouar, F.; Wojtas, L.; Eubank, J. F.; Eddaoudi, M. *Journal of the American Chemical Society* **2008**, *130*, 3768.

(48) Sun, J.; Weng, L.; Zhou, Y.; Chen, J.; Chen, Z.; Liu, Z.; Zhao, D. *Angewandte Chemie International Edition* **2002**, *41*, 4471.

(49) Zhang, J.; Chen, S.; Bu, X. *Angewandte Chemie International Edition* **2008**, *47*, 5434.

(50) Xue, Y.-S.; He, Y.; Zhou, L.; Chen, F.-J.; Xu, Y.; Du, H.-B.; You, X.-Z.; Chen, B. *Journal of Materials Chemistry A* **2013**, *1*, 4525.

(51) Yu, J.; Cui, Y.; Wu, C.; Yang, Y.; Wang, Z.; O'Keeffe, M.; Chen, B.; Qian, G. *Angewandte Chemie International Edition* **2012**, *51*, 10542.

(52) Zheng, S.-T.; Mao, C.; Wu, T.; Lee, S.; Feng, P.; Bu, X. *Journal of the American Chemical Society* **2012**, *134*, 11936.

(53) Chen, S.; Zhang, J.; Wu, T.; Feng, P.; Bu, X. *J. Am. Chem. Soc.* **2009**, *131*, 16027.

(54) Liu, Y.; Eubank, J. F.; Cairns, A. J.; Eckert, J.; Kravtsov, V. C.; Luebke, R.; Eddaoudi, M. *Angewandte Chemie International Edition* **2007**, *46*, 3278.

(55) Zhao, X.; Bu, X.; Wu, T.; Zheng, S. T.; Wang, L.; Feng, P. *Nat Commun* **2013**, *4*, 2344.

(56) Vishnoi, P.; Kalita, A.; Murugavel, R. *Journal of Chemical Sciences* **2014**, *126*, 1385.

(57) Sun, L.; Xing, H.; Liang, Z.; Yu, J.; Xu, R. *Chemical Communications* **2013**, *49*, 11155.

(58) Qian, J.; Jiang, F.; Yuan, D.; Li, X.; Zhang, L.; Su, K.; Hong, M. *Journal of Materials Chemistry A* **2013**, *1*, 9075.

(59) Bosch, M.; Zhang, M.; Feng, D.; Yuan, S.; Wang, X.; Chen, Y.-P.; Zhou, H.-C. *APL Materials* **2014**, *2*, 124103.

(60) Ameloot, R.; Aubrey, M.; Wiers, B. M.; Gómora-Figueroa, A. P.; Patel, S. N.; Balsara, N. P.; Long, J. R. *Chemistry – A European Journal* **2013**, *19*, 5533.

(61) Ferey, G. *Chem. Soc. Rev.* **2008**, *37*, 191.

(62) Gong, Y.-N.; Meng, M.; Zhong, D.-C.; Huang, Y.-L.; Jiang, L.; Lu, T.-B. *Chemical Communications* **2012**, *48*, 12002.

(63) An, J.; Rosi, N. L. *Journal of the American Chemical Society* **2010**, *132*, 5578.

(64) Dincă, M.; Dailly, A.; Liu, Y.; Brown, C. M.; Neumann, D. A.; Long, J. R. *Journal of the American Chemical Society* **2006**, *128*, 16876.

(65) Dincă, M.; Long, J. R. *Journal of the American Chemical Society* **2007**, *129*, 11172.

(66) Alkordi, M. H.; Liu, Y.; Larsen, R. W.; Eubank, J. F.; Eddaoudi, M. *Journal of the American Chemical Society* **2008**, *130*, 12639.

(67) Genna, D. T.; Wong-Foy, A. G.; Matzger, A. J.; Sanford, M. S. *Journal of the American Chemical Society* **2013**, *135*, 10586.

(68) Li, B.; Zhang, Y.; Ma, D.; Ma, T.; Shi, Z.; Ma, S. *Journal of the American Chemical Society* **2014**, *136*, 1202.

(69) Chen, C.; Wang, Y.; Wu, B.; Wu, K.; Zeng, W.; Yu, L. *Nature* **1995**, *373*, 322.

(70) Lin, W.; Wang, Z.; Ma, L. *Journal of the American Chemical Society* **1999**, *121*, 11249.

(71) Maury, O.; Le Bozec, H. *Accounts of Chemical Research* **2005**, *38*, 691.

(72) Liu, Y.; Li, G.; Li, X.; Cui, Y. *Angewandte Chemie International Edition* **2007**, *46*, 6301.

(73) An, J.; Geib, S. J.; Rosi, N. L. *Journal of the American Chemical Society* **2009**, *131*, 8376.

(74) Cui, Y.; Yue, Y.; Qian, G.; Chen, B. *Chemical Reviews* **2012**, *112*, 1126.

(75) Takashima, Y.; Martínez, V. M.; Furukawa, S.; Kondo, M.; Shimomura, S.; Uehara, H.; Nakahama, M.; Sugimoto, K.; Kitagawa, S. *Nat Commun* **2011**, *2*, 168.

(76) An, J.; Shade, C. M.; Chengelis-Czegan, D. A.; Petoud, S.; Rosi, N. L. *Journal of the American Chemical Society* **2011**, *133*, 1220.

(77) Lu, W.-G.; Jiang, L.; Feng, X.-L.; Lu, T.-B. *Inorganic Chemistry* **2009**, *48*, 6997.

(78) Bhattacharyya, S.; Chakraborty, A.; Jayaramulu, K.; Hazra, A.; Maji, T. K. *Chemical Communications* **2014**, *50*, 13567.

(79) Joarder, B.; Desai, A. V.; Samanta, P.; Mukherjee, S.; Ghosh, S. K. *Chemistry – A European Journal* **2015**, *21*, 965.

(80) Deibert, B. J.; Li, J. *Chemical Communications* **2014**, *50*, 9636.

(81) Lu, Y.; Yan, B. *Chemical Communications* **2014**, *50*, 13323.

(82) Nagarkar, S. S.; Unni, S. M.; Sharma, A.; Kurungot, S.; Ghosh, S. K. *Angewandte Chemie International Edition* **2014**, *53*, 2638.

(83) Li, C.-R.; Li, S.-L.; Zhang, X.-M. *Crystal Growth & Design* **2009**, *9*, 1702.

(84) Carlucci, L.; Cozzi, N.; Ciani, G.; Moret, M.; Proserpio, D. M.; Rizzato, S. *Chemical Communications* **2002**, 1354.

(85) Yang, Q.-Y.; Li, K.; Luo, J.; Pan, M.; Su, C.-Y. *Chemical Communications* **2011**, *47*, 4234.

(86) Noro, S. I.; Kitagawa, S.; Kondo, M.; Seki, K. *Angewandte Chemie - International Edition* **2000**, *39*, 2082.

(87) Li, D.; Kaneko, K. *Chemical Physics Letters* **2001**, *335*, 50.

(88) Noguchi, H.; Kondo, A.; Hattori, Y.; Kajiro, H.; Kanoh, H.; Kaneko, K. *The Journal of Physical Chemistry C* **2007**, *111*, 248.

(89) Yaghi, O. M.; Li, H.; Groy, T. L. *Inorganic Chemistry* **1997**, *36*, 4292.

(90) Lee, E.; Kim, J.; Heo, J.; Whang, D.; Kim, K. *Angewandte Chemie International Edition* **2001**, *40*, 399.

(91) Pan, L.; Woodlock, E. B.; Wang, X.; Lam, K.-C.; Rheingold, A. L. *Chemical Communications* **2001**, 1762.

(92) Sarkar, M.; Biradha, K. *Crystal Growth & Design* **2007**, *7*, 1318.

(93) Fan, J.; Gan, L.; Kawaguchi, H.; Sun, W.-Y.; Yu, K.-B.; Tang, W.-X. *Chemistry – A European Journal* **2003**, *9*, 3965.

(94) Tzeng, B.-C.; Chiu, T.-H.; Chen, B.-S.; Lee, G.-H. *Chemistry – A European Journal* **2008**, *14*, 5237.

(95) Hasegawa, S.; Horike, S.; Matsuda, R.; Furukawa, S.; Mochizuki, K.; Kinoshita, Y.; Kitagawa, S. *Journal of the American Chemical Society* **2007**, *129*, 2607.

(96) Kong, G.-Q.; Ou, S.; Zou, C.; Wu, C.-D. *Journal of the American Chemical Society* **2012**, *134*, 19851.

(97) Lee, J. Y.; Roberts, J. M.; Farha, O. K.; Sarjeant, A. A.; Scheidt, K. A.; Hupp, J. T. *Inorganic Chemistry* **2009**, *48*, 9971.

(98) Seo, J. S.; Whang, D.; Lee, H.; Jun, S. I.; Oh, J.; Jeon, Y. J.; Kim, K. *Nature* **2000**, *404*, 982.

(99) Mao, C.; Kudla, R. A.; Zuo, F.; Zhao, X.; Mueller, L. J.; Bu, X.; Feng, P. *Journal of the American Chemical Society* **2014**, *136*, 7579.

(100) Manna, B.; Chaudhari, A. K.; Joarder, B.; Karmakar, A.; Ghosh, S. K. *Angewandte Chemie International Edition* **2013**, *52*, 998.

(101) Ma, J.-P.; Yu, Y.; Dong, Y.-B. *Chemical Communications* **2012**, *48*, 2946.

(102) Chen, Y.-Q.; Li, G.-R.; Chang, Z.; Qu, Y.-K.; Zhang, Y.-H.; Bu, X.-H. *Chemical Science* **2013**, *4*, 3678.

(103) Karmakar, A.; Desai, A. V.; Manna, B.; Joarder, B.; Ghosh, S. K. *Chemistry – A European Journal* **2015**, *21*, 7071.

(104) Sun, J.-K.; Wang, P.; Yao, Q.-X.; Chen, Y.-J.; Li, Z.-H.; Zhang, Y.-F.; Wu, L.-M.; Zhang, J. *Journal of Materials Chemistry* **2012**, *22*, 12212.

(105) Baldoví, J. J.; Coronado, E.; Gaita-Ariño, A.; Gamer, C.; Giménez-Marqués, M.; Mínguez Espallargas, G. *Chemistry – A European Journal* **2014**, *20*, 10695.

(106) Lim, K. S.; Ryu, D. W.; Lee, W. R.; Koh, E. K.; Kim, H. C.; Hong, C. S. *Chemistry – A European Journal* **2012**, *18*, 11541.

(107) Bloch, W. M.; Sumby, C. J. *Chemical Communications* **2012**, *48*, 2534.

(108) Vyasamudri, S. Y.; Maji, T. K. *Chemical Physics Letters* **2009**, *473*, 312.

(109) Liu, J.-Y.; Wang, Q.; Zhang, L.-J.; Yuan, B.; Xu, Y.-Y.; Zhang, X.; Zhao, C.-Y.; Wang, D.; Yuan, Y.; Wang, Y.; Ding, B.; Zhao, X.-J.; Yue, M. M. *Inorganic Chemistry* **2014**, *53*, 5972.

(110) Wu, J.-Y.; Liu, Y.-C.; Chao, T.-C. *Inorganic Chemistry* **2014**, *53*, 5581.

(111) Noro, S.-i.; Kitaura, R.; Kondo, M.; Kitagawa, S.; Ishii, T.; Matsuzaka, H.; Yamashita, M. *Journal of the American Chemical Society* **2002**, *124*, 2568.

(112) Qi, X.-L.; Lin, R.-B.; Chen, Q.; Lin, J.-B.; Zhang, J.-P.; Chen, X.-M. *Chemical Science* **2011**, *2*, 2214.

(113) Kondo, A.; Noguchi, H.; Ohnishi, S.; Kajiro, H.; Tohdoh, A.; Hattori, Y.; Xu, W.-C.; Tanaka, H.; Kanoh, H.; Kaneko, K. *Nano Letters* **2006**, *6*, 2581.

(114) Maji, T. K.; Matsuda, R.; Kitagawa, S. *Nat Mater* **2007**, *6*, 142.

(115) Cheng, J.-Y.; Wang, P.; Ma, J.-P.; Liu, Q.-K.; Dong, Y.-B. *Chemical Communications* **2014**, *50*, 13672.

(116) Higuchi, M.; Tanaka, D.; Horike, S.; Sakamoto, H.; Nakamura, K.; Takashima, Y.; Hijikata, Y.; Yanai, N.; Kim, J.; Kato, K.; Kubota, Y.; Takata, M.; Kitagawa, S. *Journal of the American Chemical Society* **2009**, *131*, 10336.

(117) Sen, S.; Nair, N. N.; Yamada, T.; Kitagawa, H.; Bharadwaj, P. K. *Journal of the American Chemical Society* **2012**, *134*, 19432.

(118) Nickerl, G.; Notzon, A.; Heitbaum, M.; Senkovska, I.; Glorius, F.; Kaskel, S. *Crystal Growth & Design* **2013**, *13*, 198.

(119) Zhao, X.; Bu, X.; Wu, T.; Zheng, S.-T.; Wang, L.; Feng, P. *Nat Commun* **2013**, *4*.

(120) Kong, G.-Q.; Xu, X.; Zou, C.; Wu, C.-D. *Chemical Communications* **2011**, *47*, 11005.

(121) Molander, G. A.; Bernardi, C. R. *The Journal of Organic Chemistry* **2002**, *67*, 8424.

(122) Fei, H.; Rogow, D. L.; Oliver, S. R. J. *Journal of the American Chemical Society* **2010**, *132*, 7202.

(123) Custelcean, R.; Bonnesen, P. V.; Duncan, N. C.; Zhang, X.; Watson, L. A.; Van Berkel, G.; Parson, W. B.; Hay, B. P. *Journal of the American Chemical Society* **2012**, *134*, 8525.

(124) Li, X.; Xu, H.; Kong, F.; Wang, R. *Angewandte Chemie - International Edition* **2013**, *52*, 13769.

(125) Fu, H.-R.; Xu, Z.-X.; Zhang, J. *Chemistry of Materials* **2015**, *27*, 205.

(126) Gao, L.; Li, C.-Y. V.; Chan, K.-Y.; Chen, Z.-N. *Journal of the American Chemical Society* **2014**, *136*, 7209.

(127) Tonigold, M.; Lu, Y.; Bredenkötter, B.; Rieger, B.; Bahnmüller, S.; Hitzbleck, J.; Langstein, G.; Volkmer, D. *Angewandte Chemie* **2009**, *121*, 7682.

(128) Denysenko, D.; Werner, T.; Grzywa, M.; Puls, A.; Hagen, V.; Eickerling, G.; Jelic, J.; Reuter, K.; Volkmer, D. *Chem. Commun.* **2012**, *48*, 1236.

(129) Song, X.; Jeong, S.; Kim, D.; Lah, M. S. *CrystEngComm* **2012**, *14*, 5753.

(130) Das, S.; Kim, H.; Kim, K. *Journal of the American Chemical Society* **2009**, *131*, 3814.

(131) Kim, M.; Cahill, J. F.; Fei, H.; Prather, K. A.; Cohen, S. M. *J. Am. Chem. Soc.* **2012**, *134*, 18082.

(132) Nouar, F.; Breeze, M. I.; Campo, B. C.; Vimont, A.; Clet, G.; Daturi, M.; Devic, T.; Walton, R. I.; Serre, C. *Chemical Communications* **2015**, *51*, 14458.

(133) Kim, M.; Cahill, J. F.; Fei, H.; Prather, K. A.; Cohen, S. M. *J. Am. Chem. Soc.* **2012**, *134*, 18082.

(134) Zou, L.; Feng, D.; Liu, T.-F.; Chen, Y.-P.; Yuan, S.; Wang, K.; Wang, X.; Fordham, S.; Zhou, H.-C. *Chemical Science* **2016**.

(135) Lian, X.; Feng, D.; Chen, Y.-P.; Liu, T.-F.; Wang, X.; Zhou, H.-C. *Chemical Science* **2015**, *6*, 7044.

(136) Park, J.; Feng, D.; Zhou, H.-C. *Journal of the American Chemical Society* **2015**, *137*, 11801.

(137) Song, X.; Kim, T. K.; Kim, H.; Kim, D.; Jeong, S.; Moon, H. R.; Lah, M. S. *Chemistry of Materials* **2012**, *24*, 3065.

(138) Irving, H.; Williams, R. J. P. *Journal of the Chemical Society (Resumed)* **1953**, 3192.

(139) Liu, T.-F.; Zou, L.; Feng, D.; Chen, Y.-P.; Fordham, S.; Wang, X.; Liu, Y.; Zhou, H.-C. *J. Am. Chem. Soc.* **2014**, *136*, 7813.

(140) Grancha, T.; Ferrando-Soria, J.; Zhou, H.-C.; Gascon, J.; Seoane, B.; Pasán, J.; Fabelo, O.; Julve, M.; Pardo, E. *Angewandte Chemie International Edition* **2015**, *54*, 6521.

(141) Van Santen, R. A. *The Journal of Physical Chemistry* **1984**, *88*, 5768.

(142) Brozek, C. K.; Cozzolino, A. F.; Teat, S. J.; Chen, Y.-S.; Dincă, M. *Chemistry of Materials* **2013**, *25*, 2998.

(143) Park, J.; Chen, Y.-P.; Perry, Z.; Li, J.-R.; Zhou, H.-C. *Journal of the American Chemical Society* **2014**, *136*, 16895.

(144) Zhao, J. a.; Mi, L.; Hu, J.; Hou, H.; Fan, Y. *J. Am. Chem. Soc.* **2008**, *130*, 15222.

(145) Zhang, Z.-J.; Shi, W.; Niu, Z.; Li, H.-H.; Zhao, B.; Cheng, P.; Liao, D.-Z.; Yan, S.-P. *Chem. Commun.* **2011**, *47*, 6425.

(146) Wang, X.-S.; Chrzanowski, M.; Wojtas, L.; Chen, Y.-S.; Ma, S. *Chemistry – A European Journal* **2013**, *19*, 3297.

(147) Kim, Y.; Das, S.; Bhattacharya, S.; Hong, S.; Kim, M. G.; Yoon, M.; Natarajan, S.; Kim, K. *Chemistry – A European Journal* **2012**, *18*, 16642.

(148) Majano, G.; Martin, O.; Hammes, M.; Smeets, S.; Baerlocher, C.; Pérez-Ramírez, J. *Advanced Functional Materials* **2014**, *24*, 3855.

(149) Jiang, H.-L.; Makal, T. A.; Zhou, H.-C. *Coordination Chemistry Reviews* **2013**, *257*, 2232.

(150) Takaishi, S.; DeMarco, E. J.; Pellin, M. J.; Farha, O. K.; Hupp, J. T. *Chemical Science* **2013**, *4*, 1509.

(151) Bury, W.; Fairen-Jimenez, D.; Lalonde, M. B.; Snurr, R. Q.; Farha, O. K.; Hupp, J. T. *Chemistry of Materials* **2013**, *25*, 739.

(152) Karagiaridi, O.; Bury, W.; Sarjeant, A. A.; Stern, C. L.; Farha, O. K.; Hupp, J. T. *Chemical Science* **2012**, *3*, 3256.

(153) Burnett, B. J.; Barron, P. M.; Hu, C.; Choe, W. *Journal of the American Chemical Society* **2011**, *133*, 9984.

(154) Brozek, C. K.; Bellarosa, L.; Soejima, T.; Clark, T. V.; López, N.; Dincă, M. *Chemistry – A European Journal* **2014**, *20*, 6871.

(155) Bellarosa, L.; Brozek, C. K.; García-Melchor, M.; Dincă, M.; López, N. *Chemistry of Materials* **2015**, *27*, 3422.

(156) Akimbekov, Z.; Wu, D.; Brozek, C. K.; Dinca, M.; Navrotsky, A. *Physical Chemistry Chemical Physics* **2016**, *18*, 1158.

(157) Brozek, C. K.; Michaelis, V. K.; Ong, T.-C.; Bellarosa, L.; López, N.; Griffin, R. G.; Dincă, M. *ACS Central Science* **2015**, *1*, 252.

(158) Beckner, M.; Dailly, A. *Applied Energy* **2015**, *149*, 69.

(159) Collins, D. J.; Ma, S.; Zhou, H.-C. In *Metal-Organic Frameworks*; John Wiley & Sons, Inc.: 2010, p 249.

(160) Düren, T.; Sarkisov, L.; Yaghi, O. M.; Snurr, R. Q. *Langmuir* **2004**, *20*, 2683.

(161) Lin, X.; Champness, N.; Schröder, M. In *Topics in Current Chemistry*; Schröder, M., Ed.; Springer Berlin / Heidelberg: 2010; Vol. 293, p 35.

(162) Zhou, W. *The Chemical Record* **2010**, *10*, 200.

(163) Menon, V. C.; Komarneni, S. *Journal of Porous Materials* **1998**, *5*, 43.

(164) Advanced Research Project Agency-Energy 2012.

(165) Mason, J. A.; Veenstra, M.; Long, J. R. *Chemical Science* **2014**, *5*, 32.

(166) Senkovska, I.; Kaskel, S. *Microporous and Mesoporous Materials* **2008**, *112*, 108.

(167) Seki, K. *Chemical Communications* **2001**, 1496.

(168) Ma, S.; Sun, D.; Simmons, J. M.; Collier, C. D.; Yuan, D.; Zhou, H.-C. *Journal of the American Chemical Society* **2008**, *130*, 1012.

(169) Yuan, D.; Zhao, D.; Sun, D.; Zhou, H.-C. *Angewandte Chemie International Edition* **2010**, *49*, 5357.

(170) Banerjee, R.; Furukawa, H.; Britt, D.; Knobler, C.; O'Keeffe, M.; Yaghi, O. M. *Journal of the American Chemical Society* **2009**, *131*, 3875.

(171) Xue, M.; Liu, Y.; Schaffino, R. M.; Xiang, S.; Zhao, X.; Zhu, G.-S.; Qiu, S.-L.; Chen, B. *Inorganic Chemistry* **2009**, *48*, 4649.

(172) Bellarosa, L.; Castillo, J. M.; Vlugt, T.; Calero, S.; López, N. *Chemistry – A European Journal* **2012**, *18*, 12260.

(173) Kong, G.-Q.; Han, Z.-D.; He, Y.; Ou, S.; Zhou, W.; Yildirim, T.; Krishna, R.; Zou, C.; Chen, B.; Wu, C.-D. *Chemistry – A European Journal* **2013**, *19*, 14886.

(174) Wu, H.; Zhou, W.; Yildirim, T. *The Journal of Physical Chemistry C* **2009**, *113*, 3029.

(175) Siberio-Pérez, D. Y.; Wong-Foy, A. G.; Yaghi, O. M.; Matzger, A. J. *Chemistry of Materials* **2007**, *19*, 3681.

(176) Ma, S.; Wang, X.-S.; Collier, C. D.; Manis, E. S.; Zhou, H.-C. *Inorganic Chemistry* **2007**, *46*, 8499.

(177) Wu, H.; Zhou, W.; Yildirim, T. *J. Am. Chem. Soc.* **2009**, *131*, 4995.

(178) Dietzel, P. D. C.; Morita, Y.; Blom, R.; Fjellvåg, H. *Angewandte Chemie International Edition* **2005**, *44*, 6354.

(179) Dietzel, P. D. C.; Panella, B.; Hirscher, M.; Blom, R.; Fjellvag, H. *Chemical Communications* **2006**, 959.

(180) Dietzel, P. D. C.; Besikiotis, V.; Blom, R. *Journal of Materials Chemistry* **2009**, *19*, 7362.

(181) Zhou, W.; Wu, H.; Yildirim, T. *Journal of the American Chemical Society* **2008**, *130*, 15268.

(182) Zhou, W.; Wu, H.; Hartman, M. R.; Yildirim, T. *The Journal of Physical Chemistry C* **2007**, *111*, 16131.

(183) Ma, S.; Sun, D.; Simmons, J. M.; Collier, C. D.; Yuan, D.; Zhou, H.-C. *Journal of the American Chemical Society* **2007**, *130*, 1012.

(184) Peng, Y.; Krungleviciute, V.; Eryazici, I.; Hupp, J. T.; Farha, O. K.; Yildirim, T. *Journal of the American Chemical Society* **2013**, *135*, 11887.

(185) Wu, H.; Simmons, J. M.; Liu, Y.; Brown, C. M.; Wang, X.-S.; Ma, S.; Peterson, V. K.; Southon, P. D.; Kepert, C. J.; Zhou, H.-C.; Yildirim, T.; Zhou, W. *Chemistry – A European Journal* **2010**, *16*, 5205.

(186) Lucena, S. M. P.; Mileo, P. G. M.; Silvino, P. F. G.; Cavalcante, C. L. *Journal of the American Chemical Society* **2011**, *133*, 19282.

(187) Guo, Z.; Wu, H.; Srinivas, G.; Zhou, Y.; Xiang, S.; Chen, Z.; Yang, Y.; Zhou, W.; O'Keeffe, M.; Chen, B. *Angewandte Chemie International Edition* **2011**, *50*, 3178.

(188) Zhao, D.; Yuan, D.; Sun, D.; Zhou, H.-C. *Journal of the American Chemical Society* **2009**, *131*, 9186.

(189) Zheng, B.; Yang, Z.; Bai, J.; Li, Y.; Li, S. *Chemical Communications* **2012**, *48*, 7025.

(190) Zheng, B.; Bai, J.; Duan, J.; Wojtas, L.; Zaworotko, M. J. *Journal of the American Chemical Society* **2011**, *133*, 748.

(191) Farha, O. K.; Özgür Yazaydın, A.; Eryazici, I.; Malliakas, C. D.; Hauser, B. G.; Kanatzidis, M. G.; Nguyen, S. T.; Snurr, R. Q.; Hupp, J. T. *Nat Chem* **2010**, *2*, 944.

(192) Yan, Y.; Yang, S.; Blake, A. J.; Lewis, W.; Poirier, E.; Barnett, S. A.; Champness, N. R.; Schroder, M. *Chemical Communications* **2011**, *47*, 9995.

(193) Yan, Y.; Telepeni, I.; Yang, S.; Lin, X.; Kockelmann, W.; Dailly, A.; Blake, A. J.; Lewis, W.; Walker, G. S.; Allan, D. R.; Barnett, S. A.; Champness, N. R.; Schröder, M. *Journal of the American Chemical Society* **2010**, *132*, 4092.

(194) Getzschmann, J.; Senkovska, I.; Wallacher, D.; Tovar, M.; Fairen-Jimenez, D.; Düren, T.; van Baten, J. M.; Krishna, R.; Kaskel, S. *Microporous and Mesoporous Materials* **2010**, *136*, 50.

(195) Li, B.; Wen, H.-M.; Wang, H.; Wu, H.; Tyagi, M.; Yildirim, T.; Zhou, W.; Chen, B. *Journal of the American Chemical Society* **2014**, *136*, 6207.

(196) Li, B.; Wen, H.-M.; Wang, H.; Wu, H.; Yildirim, T.; Zhou, W.; Chen, B. *Energy & Environmental Science* **2015**.

(197) Yang, Q.; Guillerm, V.; Ragon, F.; Wiersum, A. D.; Llewellyn, P. L.; Zhong, C.; Devic, T.; Serre, C.; Maurin, G. *Chemical Communications* **2012**, *48*, 9831.

(198) Gomez-Gualdron, D. A.; Gutov, O. V.; Krungleviciute, V.; Borah, B.; Mondloch, J. E.; Hupp, J. T.; Yildirim, T.; Farha, O. K.; Snurr, R. Q. *Chemistry of Materials* **2014**, *26*, 5632.

(199) Peng, Y.; Srinivas, G.; Wilmer, C. E.; Eryazici, I.; Snurr, R. Q.; Hupp, J. T.; Yildirim, T.; Farha, O. K. *Chemical Communications* **2013**, *49*, 2992.

(200) Wilmer, C. E.; Leaf, M.; Lee, C. Y.; Farha, O. K.; Hauser, B. G.; Hupp, J. T.; Snurr, R. Q. *Nat Chem* **2012**, *4*, 83.

(201) Martin, R. L.; Simon, C. M.; Smit, B.; Haranczyk, M. *Journal of the American Chemical Society* **2014**, *136*, 5006.

(202) He, Y.; Zhou, W.; Yildirim, T.; Chen, B. *Energy & Environmental Science* **2013**, *6*, 2735.

(203) Zhao, X.; Sun, D.; Yuan, S.; Feng, S.; Cao, R.; Yuan, D.; Wang, S.; Dou, J.; Sun, D. *Inorganic Chemistry* **2012**, *51*, 10350.

(204) Wang, Y.; Tan, C.; Sun, Z.; Xue, Z.; Zhu, Q.; Shen, C.; Wen, Y.; Hu, S.; Wang, Y.; Sheng, T.; Wu, X. *Chemistry – A European Journal* **2014**, *20*, 1341.

(205) Ma, L.; Lin, W. In *Functional Metal-Organic Frameworks: Gas Storage, Separation and Catalysis*; Schröder, M., Ed.; Springer Berlin Heidelberg: 2010; Vol. 293, p 175.

(206) Lalonde, M. B.; Farha, O. K.; Scheidt, K. A.; Hupp, J. T. *ACS Catalysis* **2012**, *2*, 1550.

(207) Wang, J.-L.; Wang, C.; Lin, W. *ACS Catalysis* **2012**, *2*, 2630.

(208) Liu, J.; Chen, L.; Cui, H.; Zhang, J.; Zhang, L.; Su, C.-Y. *Chem. Soc. Rev.* **2014**, *43*, 6011.

(209) Chughtai, A. H.; Ahmad, N.; Younus, H. A.; Laypkov, A.; Verpoort, F. *Chemical Society Reviews* **2015**.

(210) Yu, X.; Cohen, S. M. *Chemical Communications* **2015**, *51*, 9880.

(211) Wang, C.; Xie, Z.; deKrafft, K. E.; Lin, W. *Journal of the American Chemical Society* **2011**, *133*, 13445.

(212) Sun, L.-B.; Liu, X.-Q.; Zhou, H.-C. *Chemical Society Reviews* **2015**, *44*, 5092.

(213) Yoon, T. P.; Ischay, M. A.; Du, J. *Nat Chem* **2010**, *2*, 527.

(214) Han, S.; Wei, Y.; Grzybowski, B. A. *Chemistry – A European Journal* **2013**, *19*, 11194.

(215) Prier, C. K.; Rankic, D. A.; MacMillan, D. W. C. *Chemical Reviews* **2013**, *113*, 5322.

(216) Toyao, T.; Saito, M.; Dohshi, S.; Mochizuki, K.; Iwata, M.; Higashimura, H.; Horiuchi, Y.; Matsuoka, M. *Chemical Communications* **2014**, *50*, 6779.

(217) Zhang, Z.-M.; Zhang, T.; Wang, C.; Lin, Z.; Long, L.-S.; Lin, W. *J. Am. Chem. Soc.* **2015**, *137*, 3197.

(218) Xu, Y.; Yin, X.-B.; He, X.-W.; Zhang, Y.-K. *Biosensors and Bioelectronics* **2015**, *68*, 197.

(219) Wang, C.; Liu, D.; Xie, Z.; Lin, W. *Inorganic Chemistry* **2014**, *53*, 1331.

(220) Zhang, S.; Han, L.; Li, L.; Cheng, J.; Yuan, D.; Luo, J. *Crystal Growth & Design* **2013**, *13*, 5466.

(221) Sen, R.; Koner, S.; Bhattacharjee, A.; Kusz, J.; Miyashita, Y.; Okamoto, K.-I. *Dalton Transactions* **2011**, *40*, 6952.

(222) Lin, X.; Luo, F.; Zheng, L.; Gao, G.; Chi, Y. *Analytical Chemistry* **2015**, *87*, 4864.

(223) Kent, C. A.; Liu, D.; Ito, A.; Zhang, T.; Brennaman, M. K.; Meyer, T. J.; Lin, W. *Journal of Materials Chemistry A* **2013**, *1*, 14982.

(224) Larsen, R. W.; Wojtas, L. *Journal of Materials Chemistry A* **2013**, *1*, 14133.

(225) Yang, S.; Lin, X.; Blake, A. J.; Walker, G. S.; Hubberstey, P.; Champness, N. R.; Schröder, M. *Nat Chem* **2009**, *1*, 487.

(226) Qin, J.-S.; Zhang, S.-R.; Du, D.-Y.; Shen, P.; Bao, S.-J.; Lan, Y.-Q.; Su, Z.-M. *Chemistry – A European Journal* **2014**, *20*, 5625.

(227) Qin, J.-S.; Bao, S.-J.; Li, P.; Xie, W.; Du, D.-Y.; Zhao, L.; Lan, Y.-Q.; Su, Z.-M. *Chemistry – An Asian Journal* **2014**, *9*, 749.

(228) Zhang, Y.-B.; Zhou, H.-L.; Lin, R.-B.; Zhang, C.; Lin, J.-B.; Zhang, J.-P.; Chen, X.-M. *Nat Commun* **2012**, *3*, 642.

(229) He, Y.-C.; Yang, J.; Kan, W.-Q.; Zhang, H.-M.; Liu, Y.-Y.; Ma, J.-F. *Journal of Materials Chemistry A* **2015**, *3*, 1675.

(230) Cychosz, K. A.; Ahmad, R.; Matzger, A. J. *Chemical Science* **2010**, *1*, 293.

(231) Johnson, J. A.; Zhang, X.; Reeson, T. C.; Chen, Y.-S.; Zhang, J. *Journal of the American Chemical Society* **2014**, *136*, 15881.

(232) Zheng, S.-T.; Bu, J. T.; Li, Y.; Wu, T.; Zuo, F.; Feng, P.; Bu, X. *J. Am. Chem. Soc.* **2010**, *132*, 17062.

(233) Delgado-Friedrichs, O.; O'Keeffe, M.; Yaghi, O. M. *Physical Chemistry Chemical Physics* **2007**, *9*, 1035.

(234) Sheldrick, G. M. S.-. *SHELXS-97 ,Programs for X-ray Crystal Stucture Solution;* **1997**, University of Gottinggen: Gottinggen.

(235) Sheldrick, G. M. *S.-. SHELXS-97 ,Programs for X-ray Crystal Structure Refinement*, University of Gottinggen; Gottinggen.

(236) Farrugia, L. J. *WINGX, A Windows Program for Crystal Structure Analysis*, University of Glasgow: Glasgow.

(237) van der Sluis, P. S., A. L. *Acta Cyrstallogr., Sect A* **1990**, *46*, 194.

(238) Blatov, V. A.; Shevchenko, A. P.; Proserpio, D. M. *Crystal Growth & Design* **2014**, *14*, 3576.

(239) Fang, Q.-R.; Yuan, D.-Q.; Sculley, J.; Li, J.-R.; Han, Z.-B.; Zhou, H.-C. *Inorganic Chemistry* **2010**, *49*, 11637.

(240) Wang, X.; Lu, W.; Gu, Z.-Y.; Wei, Z.; Zhou, H.-C. *Chemical Communications* **2016**, *52*, 1926.

(241) Mao, X.; Wang, C.; Ma, X.; Zhang, M.; Liu, L.; Zhang, L.; Niu, L.; Zeng, Q.; Yang, Y.; Wang, C. *Nanoscale* **2011**, *3*, 1592.

(242) Zou, Y.-Q.; Chen, J.-R.; Liu, X.-P.; Lu, L.-Q.; Davis, R. L.; Jørgensen, K. A.; Xiao, W.-J. *Angewandte Chemie International Edition* **2012**, *51*, 784.

(243) Huang, Y.; Lin, Z.; Fu, H.; Wang, F.; Shen, M.; Wang, X.; Cao, R. *ChemSusChem* **2014**, *7*, 2647.

(244) Feng, D.; Liu, T. F.; Su, J.; Bosch, M.; Wei, Z.; Wan, W.; Yuan, D.; Chen, Y. P.; Wang, X.; Wang, K.; Lian, X.; Gu, Z. Y.; Park, J.; Zou, X.; Zhou, H. C. *Nat Commun* **2015**, *6*, 5979.

(245) Della Rocca, J.; Liu, D.; Lin, W. *Accounts of Chemical Research* **2011**, *44*, 957.

(246) O'Keeffe, M.; Peskov, M. A.; Ramsden, S. J.; Yaghi, O. M. *Accounts of Chemical Research* **2008**, *41*, 1782.

(247) F?rey, G. r. *Chemical Society Reviews* **2008**, *37*, 191.

(248) Horike, S.; Shimomura, S.; Kitagawa, S. *Nat Chem* **2009**, *1*, 695.

(249) Lu, W.; Wei, Z.; Gu, Z.-Y.; Liu, T.-F.; Park, J.; Park, J.; Tian, J.; Zhang, M.; Zhang, Q.; Gentle Iii, T.; Bosch, M.; Zhou, H.-C. *Chem. Soc. Rev.* **2014**, *43*, 5561.

(250) Brozek, C. K.; Miller, J. T.; Stoian, S. A.; Dincă, M. *Journal of the American Chemical Society* **2015**, *137*, 7495.

(251) Wang, Z.; Cohen, S. M. *Chemical Society Reviews* **2009**, *38*, 1315.

(252) Lalonde, M.; Bury, W.; Karagiaridi, O.; Brown, Z.; Hupp, J. T.; Farha, O. K. *J. Mater. Chem. A* **2013**, *1*, 5453.

(253) Han, Y.; Li, J.-R.; Xie, Y.; Guo, G. *Chemical Society Reviews* **2014**, *43*, 5952.

(254) Deria, P.; Mondloch, J. E.; Karagiaridi, O.; Bury, W.; Hupp, J. T.; Farha, O. K. *Chemical Society Reviews* **2014**, *43*, 5896.

(255) Brozek, C. K.; Dinc, M. *Chemical Society Reviews* **2014**, *43*, 5456.

(256) Yao, Q.; Sun, J.; Li, K.; Su, J.; Peskov, M. V.; Zou, X. *Dalton Transactions* **2012**, *41*, 3953.

(257) Zhang, Z.; Zhang, L.; Wojtas, L.; Nugent, P.; Eddaoudi, M.; Zaworotko, M. J. *Journal of the American Chemical Society* **2012**, *134*, 924.

(258) Brozek, C. K.; Dincă, M. *Journal of the American Chemical Society* **2013**, *135*, 12886.

(259) Liao, J.-H.; Chen, W.-T.; Tsai, C.-S.; Wang, C.-C. *CrystEngComm* **2013**, *15*, 3377.

(260) Kim, Y.; Das, S.; Bhattacharya, S.; Hong, S.; Kim, M. G.; Yoon, M.; Natarajan, S.; Kim, K. *Chemistry - A European Journal* **2012**, *18*, 16642.

(261) Song, X.; Jeong, S.; Kim, D.; Lah, M. S. *CrystEngComm* **2012**, *14*, 5753.

(262) Rivest, J. B.; Jain, P. K. *Chemical Society Reviews* **2013**, *42*, 89.

(263) Wei, Z.; Lu, W.; Jiang, H.-L.; Zhou, H.-C. *Inorganic Chemistry* **2013**, *52*, 1164.

(264) Brozek, C. K.; Dinca, M. *Chemical Society Reviews* **2014**, *43*, 5456.

(265) Akimbekov, Z.; Wu, D.; Brozek, C. K.; Dinca, M.; Navrotsky, A. *Physical Chemistry Chemical Physics* **2015**.

(266) Brozek, C. K.; Dinca, M. *Chemical Communications* **2015**, *51*, 11780.

(267) Lalonde, M.; Bury, W.; Karagiaridi, O.; Brown, Z.; Hupp, J. T.; Farha, O. K. *Journal of Materials Chemistry A* **2013**, *1*, 5453.

(268) Li, J.; Huang, P.; Wu, X.-R.; Tao, J.; Huang, R.-B.; Zheng, L.-S. *Chemical Science* **2013**, *4*, 3232.

(269) Huang, S.; Li, X.; Shi, X.; Hou, H.; Fan, Y. *Journal of Materials Chemistry* **2010**, *20*, 5695.

(270) Meng, W.; Li , H.; Xu , Z.; Du, S.; Li, Y.; Zhu, Y.; Han , Y.; Hou, H.; Fan, Y.; Tang, M. *Chemistry – A European Journal* **2014**, *20*, 2945.

(271) Mukherjee, G.; Biradha, K. *Chemical Communications* **2012**, *48*, 4293.

(272) Zhang, Z.; Wojtas, L.; Eddaoudi, M.; Zaworotko, M. J. *Journal of the American Chemical Society* **2013**, *135*, 5982.

(273) Niu, Y.-F.; Zhao, W.; Han, J.; GeTian; Zhao, X.-L. *CrystEngComm* **2014**, *16*, 2344.

(274) Mallick, A.; Saha, S.; Pachfule, P.; Roy, S.; Banerjee, R. *Journal of Materials Chemistry* **2010**, *20*, 9073.

(275) Saha, D.; Maity, T.; Das, S.; Koner, S. *Dalton Transactions* **2013**, *42*, 13912.

(276) Huang, Y.-L.; Gong, Y.-N.; Jiang, L.; Lu, T.-B. *Chemical Communications* **2013**, *49*, 1753.

(277) Ramaswamy, P.; Wong, N. E.; Gelfand, B. S.; Shimizu, G. K. H. *Journal of the American Chemical Society* **2015**, *137*, 7640.

(278) Xie, Y.-M.; Wu, J.-H. *Inorganica Chimica Acta* **2014**, *412*, 15.

(279) Wu, Z.-F.; Tan, B.; Feng, M.-L.; Lan, A.-J.; Huang, X.-Y. *Journal of Materials Chemistry A* **2014**, *2*, 6426.

(280) Zuo, C.; Lu, Z.; Zhang, M. *Inorganic Chemistry Communications* **2015**, *52*, 41.

(281) Volkringer, C.; Loiseau, T.; Marrot, J.; Ferey, G. *CrystEngComm* **2009**, *11*, 58.

(282) Yu, C.; Ma, S.; Pechan, M. J.; Zhou, H.-c. *J. Appl. Phys.* **2007**, *101*, 09E108.

(283) Ma, S.; Sun, D.; Ambrogio, M.; Fillinger, J. A.; Parkin, S.; Zhou, H.-C. *Journal of the American Chemical Society* **2007**, *129*, 1858.

(284) Sun, D.; Ma, S.; Ke, Y.; Petersen, T. M.; Zhou, H.-C. *Chemical Communications* **2005**, 2663.

(285) Ma, S.; Zhou, H.-C. *Journal of the American Chemical Society* **2006**, *128*, 11734.

(286) Sun, D.; Ma, S.; Ke, Y.; Collins, D. J.; Zhou, H.-C. *Journal of the American Chemical Society* **2006**, *128*, 3896.

(287) Park, Y. K.; Choi, S. B.; Kim, H.; Kim, K.; Won, B.-H.; Choi, K.; Choi, J.-S.; Ahn, W.-S.; Won, N.; Kim, S.; Jung, D. H.; Choi, S.-H.; Kim, G.-H.; Cha, S.-S.; Jhon, Y. H.; Yang, J. K.; Kim, J. *Angewandte Chemie International Edition* **2007**, *46*, 8230.

(288) Sun, D.; Ke, Y.; Collins, D. J.; Lorigan, G. A.; Zhou, H.-C. *Inorganic Chemistry* **2007**, *46*, 2725.

(289) Ma, S.; Wang, X.-S.; Yuan, D.; Zhou, H.-C. *Angewandte Chemie International Edition* **2008**, *47*, 4130.

(290) Ma, S.; Yuan, D.; Wang, X.-S.; Zhou, H.-C. *Inorganic Chemistry* **2009**, *48*, 2072.

(291) Gao, W.; Xing, F.; Zhou, D.; Shao, M.; Zhu, S. *Inorganic Chemistry Communications* **2011**, *14*, 601.

(292) Zhang, H.; Li, N.; Tian, C.; Liu, T.; Du, F.; Lin, P.; Li, Z.; Du, S. *Crystal Growth & Design* **2012**, *12*, 670.

(293) Han, L.; Qin, L.; Xu, L.-P.; Zhao, W.-N. *Inorganic Chemistry* **2013**, *52*, 1667.

(294) Zhang, X.; Fan, L.; Sun, Z.; Zhang, W.; Fan, W.; Sun, L.; Zhao, X. *CrystEngComm* **2013**, *15*, 4910.

(295) Feng, D.; Liu, T.-F.; Su, J.; Bosch, M.; Wei, Z.; Wan, W.; Yuan, D.; Chen, Y.-P.; Wang, X.; Wang, K.; Lian, X.; Gu, Z.-Y.; Park, J.; Zou, X.; Zhou, H.-C. *Nat Commun* **2015**, *6*.

(296) Clegg, W.; Little, I. R.; Straughan, B. P. *Inorganic Chemistry* **1988**, *27*, 1916.

(297) Ma, S.; Wang, X.-S.; Manis, E. S.; Collier, C. D.; Zhou, H.-C. *Inorganic Chemistry* **2007**, *46*, 3432.

(298) Helm, L.; Merbach, A. E. *Coordination Chemistry Reviews* **1999**, *187*, 151.

(299) Zhou, H.-C. J.; Kitagawa, S. *Chem. Soc. Rev.* **2014**, *43*, 5415.

(300) He, Y.; Zhou, W.; Qian, G.; Chen, B. *Chem. Soc. Rev.* **2014**, *43*, 5657.

(301) Qin, J.-S.; Du, D.-Y.; Li, W.-L.; Zhang, J.-P.; Li, S.-L.; Su, Z.-M.; Wang, X.-L.; Xu, Q.; Shao, K.-Z.; Lan, Y.-Q. *Chemical Science* **2012**, *3*, 2114.

(302) Sumida, K.; Rogow, D. L.; Mason, J. A.; McDonald, T. M.; Bloch, E. D.; Herm, Z. R.; Bae, T.-H.; Long, J. R. *Chemical Reviews* **2012**, *112*, 724.

(303) Yang, Q.; Liu, D.; Zhong, C.; Li, J.-R. *Chemical Reviews* **2013**, *113*, 8261.

(304) DeCoste, J. B.; Peterson, G. W. *Chemical Reviews* **2014**, *114*, 5695.

(305) Hu, T.-L.; Wang, H.; Li, B.; Krishna, R.; Wu, H.; Zhou, W.; Zhao, Y.; Han, Y.; Wang, X.; Zhu, W.; Yao, Z.; Xiang, S.; Chen, B. *Nat Commun* **2015**, *6*.

(306) Allendorf, M. D.; Bauer, C. A.; Bhakta, R. K.; Houk, R. J. T. *Chem. Soc. Rev.* **2009**, *38*, 1330.

(307) Heine, J.; Müller-Buschbaum, K. *Chemical Society Reviews* **2013**, *42*, 9232.

(308) Wang, H.; Xu, J.; Zhang, D.-S.; Chen, Q.; Wen, R.-M.; Chang, Z.; Bu, X.-H. *Angewandte Chemie* **2015**, *127*, 6064.

(309) Chen, Q.; Chang, Z.; Song, W.-C.; Song, H.; Song, H.-B.; Hu, T.-L.; Bu, X.-H. *Angew. Chem. Int. Edit.* **2013**, *52*, 11550.

(310) Yoon, M.; Srirambalaji, R.; Kim, K. *Chemical Reviews* **2012**, *112*, 1196.

(311) Gu, Z.-Y.; Park, J.; Raiff, A.; Wei, Z.; Zhou, H.-C. *ChemCatChem* **2013**, *6*, 67.

(312) Beletskaya, I.; Tyurin, V. S.; Tsivadze, A. Y.; Guilard, R.; Stern, C. *Chemical Reviews* **2009**, *109*, 1659.

(313) Gao, W.-Y.; Chrzanowski, M.; Ma, S. *Chem. Soc. Rev.* **2014**, *43*, 5841.

(314) Jiang, H.-L.; Feng, D.; Wang, K.; Gu, Z.-Y.; Wei, Z.; Chen, Y.-P.; Zhou, H.-C. *Journal of the American Chemical Society* **2013**, *135*, 13934.

(315) Xu, H.-Q.; Hu, J.; Wang, D.; Li, Z.; Zhang, Q.; Luo, Y.; Yu, S.-H.; Jiang, H.-L. *Journal of the American Chemical Society* **2015**, *137*, 13440.

(316) Lee, C. Y.; Farha, O. K.; Hong, B. J.; Sarjeant, A. A.; Nguyen, S. T.; Hupp, J. T. *J. Am. Chem. Soc.* **2011**, *133*, 15858.

(317) Jin, S.; Son, H.-J.; Farha, O. K.; Wiederrecht, G. P.; Hupp, J. T. *J. Am. Chem. Soc.* **2013**, *135*, 955.

(318) Son, H.-J.; Jin, S.; Patwardhan, S.; Wezenberg, S. J.; Jeong, N. C.; So, M.; Wilmer, C. E.; Sarjeant, A. A.; Schatz, G. C.; Snurr, R. Q.; Farha, O. K.; Wiederrecht, G. P.; Hupp, J. T. *J. Am. Chem. Soc.* **2013**, *135*, 862.

(319) Wang, K.; Lv, X.-L.; Feng, D.; Li, J.; Chen, S.; Sun, J.; Song, L.; Xie, Y.; Li, J.-R.; Zhou, H.-C. *Journal of the American Chemical Society* **2016**, *138*, 914.

(320) Liu, T.-F.; Feng, D.; Chen, Y.-P.; Zou, L.; Bosch, M.; Yuan, S.; Wei, Z.; Fordham, S.; Wang, K.; Zhou, H.-C. *J. Am. Chem. Soc.* **2015**, *137*, 413.

(321) Feng, D.; Chung, W.-C.; Wei, Z.; Gu, Z.-Y.; Jiang, H.-L.; Chen, Y.-P.; Darensbourg, D. J.; Zhou, H.-C. *J. Am. Chem. Soc.* **2013**, *135*, 17105.

(322) Aromí, G.; Barrios, L. A.; Roubeau, O.; Gamez, P. *Coordination Chemistry Reviews* **2011**, *255*, 485.

(323) Zhang, J.-P.; Zhang, Y.-B.; Lin, J.-B.; Chen, X.-M. *Chemical Reviews* **2012**, *112*, 1001.

(324) Wang, F.; Hou, D.-C.; Yang, H.; Kang, Y.; Zhang, J. *Dalton Trans.* **2014**, *43*, 3210.

(325) Andersson Trojer, M.; Movahedi, A.; Blanck, H.; Nydén, M. *Journal of Chemistry* **2013**, *2013*, 1.

(326) Zhu, X.-J.; Wong, W.-K.; Jiang, F.-L.; Poon, C.-T.; Wong, W.-Y. *Tetrahedron Letters* **2008**, *49*, 2114.

(327) Gauuan, P. J. F.; Trova, M. P.; Gregor-Boros, L.; Bocckino, S. B.; Crapo, J. D.; Day, B. J. *Bioorganic & Medicinal Chemistry* **2002**, *10*, 3013.

(328) Liu, D.; Liu, T.-F.; Chen, Y.-P.; Zou, L.; Feng, D.; Wang, K.; Zhang, Q.; Yuan, S.; Zhong, C.; Zhou, H.-C. *J. Am. Chem. Soc.* **2015**, *137*, 7740.

(329) Guo, Z.; Yan, D.; Wang, H.; Tesfagaber, D.; Li, X.; Chen, Y.; Huang, W.; Chen, B. *Inorganic Chemistry* **2015**, *54*, 200.

(330) Ma, L.; Mihalcik, D. J.; Lin, W. *J. Am. Chem. Soc.* **2009**, *131*, 4610.

(331) Tan, C.; Yang, S.; Champness, N. R.; Lin, X.; Blake, A. J.; Lewis, W.; Schröder, M. *Chemical Communications* **2011**, *47*, 4487.

(332) Cheng, X.; Duan, X.-y.; Liu, T.; Wang, F.-m.; Lu, C.-s.; Meng, Q.-j. *Inorganic Chemistry Communications* **2010**, *13*, 818.

(333) Hu, S.; Meng, Z.-S.; Tong, M.-L. *Crystal Growth & Design* **2010**, *10*, 1742.

(334) Park, J.; Li, J.-R.; Chen, Y.-P.; Yu, J.; Yakovenko, A. A.; Wang, Z. U.; Sun, L.-B.; Balbuena, P. B.; Zhou, H.-C. *Chemical Communications* **2012**, *48*, 9995.

(335) Shiju, N. R.; Alberts, A. H.; Khalid, S.; Brown, D. R.; Rothenberg, G. *Angewandte Chemie International Edition* **2011**, *50*, 9615.

(336) Li, B.; Zhang, Y.; Ma, D.; Li, L.; Li, G.; Li, G.; Shi, Z.; Feng, S. *Chemical Communications* **2012**, *48*, 6151.

(337) Li, P.; Yu, Y.; Huang, P.-P.; Liu, H.; Cao, C.-Y.; Song, W.-G. *J. Mater. Chem. A* **2014**, *2*, 339.

(338) Díaz, U.; Brunel, D.; Corma, A. *Chemical Society Reviews* **2013**, *42*, 4083.

(339) Hawn, D. D.; DeKoven, B. M. *Surface and Interface Analysis* **1987**, *10*, 63.

(340) Brion, D. *Applications of Surface Science* **1980**, *5*, 133.

(341) Makal, T. A.; Li, J. R.; Lu, W.; Zhou, H. C. *Chem. Soc. Rev.* **2012**, *41*, 7761.

(342) Cohen, S. M. *Chem. Rev.* **2011**, *112*, 970.

(343) O'Keeffe, M.; Yaghi, O. M. *Chem. Rev.* **2011**, *112*, 675.

(344) Meek, S. T.; Greathouse, J. A.; Allendorf, M. D. *Advanced Materials* **2011**, *23*, 249.

(345) Jasuja, H.; Zang, J.; Sholl, D. S.; Walton, K. S. *The Journal of Physical Chemistry C* **2012**, *116*, 23526.

(346) Feng, D.; Gu, Z. Y.; Li, J. R.; Jiang, H. L.; Wei, Z.; Zhou, H. C. *Angew. Chem. Int. Ed. Engl.* **2012**, *51*, 10307.

(347) Jiang, H.-L.; Feng, D.; Liu, T.-F.; Li, J.-R.; Zhou, H.-C. *Journal of the American Chemical Society* **2012**, *134*, 14690.

(348) Makal, T. A.; Wang, X.; Zhou, H.-C. *Crystal Growth & Design* **2013**, *13*, 4760.

(349) Kosynkin, D. V.; Tour, J. M. *Organic Letters* **2001**, *3*, 993.

(350) Shi, D.; Ren, Y.; Jiang, H.; Lu, J.; Cheng, X. *Dalton Transactions* **2013**, *42*, 484.